PROTON SCATTERING AS A PROBE OF RELATIVITY IN NUCLEI

by

David P. Murdock

B.S., Chemistry, California Institute of Technology, 1976

M.S., Physics, University of Colorado, 1983

Submitted to the Department of Physics
in partial fulfillment of the requirements
for the degree of
Doctor of Philosophy
at the
Massachusetts Institute of Technology

Signature of Author _____
Department of Physics, August 1987

Certified by _____
Charles J. Horowitz, Thesis Supervisor

Accepted by _____
Chairman, Department Committee

Proton Scattering as a Probe of
Probe of Relativity in Nuclei

by

David P. Murdock

Submitted to the Department of Physics
on August 7, 1987 in partial fulfillment of the
requirements for the Degree of
Doctor of Philosophy in Physics

ABSTRACT

The relativistic impulse approximation is applied to proton elastic scattering (Chapter 2) and proton quasi-elastic scattering (Chapter 3) to examine the effects of relativistic dynamics on the predicted experimental observables. When possible, comparison with experiment is made.

Proton elastic scattering from ^{12}C, ^{16}O, ^{40}Ca, ^{48}Ca, ^{90}Zr and ^{208}Pb at energies near 200 MeV is studied with a relativistic microscopic calculation of the Dirac optical potential. This calculation goes beyond the original RIA by including: (a) An explicit treatment of exchange terms in the optical potential; (b) Medium modifications from Pauli blocking; (c) The resolution of an important ambiguity in the relativistic NN amplitude by using pseudovector π coupling. The results quantitatively reproduce all measured spin observables (A_y and Q) except at very large backward angles. Energy dependence and sensitities of the microscopic calculation are discussed.

Proton quasi-elastic scattering at energies from 300 to 800 MeV on ^{12}C, ^{40}Ca and ^{208}Pb is calculated using a relativistic plane wave impulse approximation with a Fermi gas model for the target. Relativistic effects are incorporated by using spinors characterized by effective masses of from $.8M$ to $.9M$. The enhanced lower components give significant differences between relativistic and nonrelativistic predictions of some quasi-elastic spin observables. The analyzing power at $T_{\rm lab} = 500$ MeV, $\theta_{\rm lab} = 18.5°$ decreases from the free NN value when relativistic spinors are used, in agreement with the data. The polarization transfer coefficients $D_{s's}$ and $D_{l'l}$ show some disagreement with the data, and the others (D_{nn} and $D_{s'l}$) are unaffected. Predictions for observables at other energies and scattering angles are presented. Finally, calculations are presented for the (p,n) quasi-free charge exchange reaction, which give significantly different predictions for the cross section and some spin observables depending on the use of relativistic spinors and the choice of pion coupling.

Magnetic moments are calculated for closed shell–plus–one nuclei. It is shown that when one accounts for the interaction of the valence nucleon with the nuclear core, agreement with the experimental values is comparable to that of the nonrelativistic "Schmidt" magnetic moments.

Thesis Supervisor: Charles Horowitz (Assistant Professor of Physics)

FOREWORD

Much of the fun of doing theoretical physics is in being able to make successful predictions of experiments. It's especially exciting (and rare) to be able to make them in the *literal* as well as the *scientific* sense, and to see a set of detailed predictions confirmed after they made. That is just what happened during the course of this work, with the 200 MeV proton elastic spin observables for ^{90}Zr and ^{208}Pb, later measured by the Hausser group at TRIUMF.

My own interest in the subject of relativity in proton scattering came from my earlier graduate work at the University of Colorado where I assisted with the first relativistic impulse approximation calculation, and where it was discovered that the simplest relativistic version of the old KMT theory did surprisingly well with the recently–measured analyzing power for 500 MeV p + ^{40}Ca scattering. No one interested in proton scattering could ignore the predictions of spin observables in Refs.[Sh83] and [Cl83b], even people who might not have liked the idea of using the Dirac equation to do nuclear physics. (Those relativistic guys must have done *something* right!) In fact, it is still an open question as to just what *was* done right in the Dirac calculation, one which is not dealt with in this thesis, and which I would like to study at some later date. But the first project written up in this thesis (Chapter 2, also published as *Phys. Rev.* **C35**, 1442 (1987)) shows that the original success at 500 MeV was no fluke and that the RIA works at lower energies, provided one applies it more carefully than in the first publications.

The next part (Chapter 3) presents calculations for a different and in some respects more rigorous test of relativistic impulse approximations, the prediction of the observables of quasi-elastic proton scattering, for which data are only now starting to come in from LAMPF and TRIUMF. Theoretical work on this subject is also in an underdeveloped state, and there is lots of work ahead in seeing how the quasi-free

(p,p′) and (p,n) reactions probe the need for relativistic dynamics in descriptions of nuclei. This work is presently being prepared for publication.

General Acknowledgements

First, my thanks go to my thesis advisor, Charles Horowitz for guiding me through several projects which were interesting and, I feel, important for the understanding of current intermediate–energy proton scattering experiments. These projects gave me the chance to do some math, some computation and to have contact with experimentalists and their data. Chuck has taught me much about finding interesting physical problems, seeing the important physics in them and doing careful computations to get to the answers. I am grateful for his guidance in doing calculations that the experimentalists wanted to see and getting them into published form, and for encouraging me to be an active participant in the community of nuclear physics researchers.

Next, I would like to thank the other people who in one way or another have served as my research advisors. They are Jim Shepard and Ernie Rost of the University of Colorado, where I got a valuable start in doing the types of calculations in this thesis; Chris Zafiratos, also of the CU Nuclear Physics Lab, and W. Carl Lineberger of JILA and the Department of Chemistry at CU.

I'm also grateful to John Negele of MIT for his help, comments and enthusiasm for the work of the nuclear physics grad students at MIT. (Seems like *that* one shows up in just about everyone's acknowledgements, doesn't it?) And I appreciate the efforts of all my other teachers at MIT and CU.

Ken Hicks of TRIUMF provided me with news of experimental developments, new data and help with my trips to TRIUMF as well as being a good friend from back in my CU days. Steve Lepp of The Harvard Observatory (another old CU crony!) helped me learn about microcomputing; Dick Furnstahl of IUCF and Roger Gilson gave assistance with TEX. My friend Judy Powelson and her parents have given me support

and hospitality whenever I was in Boulder. And I thank my brother, Steve Murdock and my mother, Rose Murdock for their valuable help with my financial support.

Finally there are my officemates, fellow grad students and other local friends who have made life in Boston tolerable. These include Mike and Kathleen Forgac (old CalTech friends) and Steve Lepp; officemates Suzhou Huang, Marcello Lissia, Jim Mahoney (a fellow American!!), Illka Vuorio, Shunzo Kumano, Nouredine Zettilli and Jacek Myczkowski; MIT grad students Michael Biafore, Susan Gardner, Eric Kronenberg and Alan Raskin.

Thanks again to everyone.

Chapter 1. Introduction

1.A Relativity and Nuclear Physics

The atomic nucleus is a complex many–body system whose components interact strongly and at short range. Presumably, the correct degrees of freedom are the quark and gluon fields of quantum chromodynamics, but at present it is very difficult to understand nuclear phenomena along these lines. The job of the nuclear physicist is to find the *important* degrees of freedom of the nuclear system and the dynamics obeyed by them.

Traditionally, those degrees of freedom have been taken to be protons and neutrons interacting via two-body potentials and described by Schrödinger (nonrelativistic) wavefunctions and the many–particle Schrödinger equation. While the formalism of relativistic field theories is often used to obtain the forms of NN potentials they are then customarily used in *non*relativistic calculations; the lower components of the Dirac wavefunctions are assumed unchanged in the nuclear medium.

In the past decade support has been given to the idea that nucleon dynamics should begin *and stay* in the framework of relativistic quantum mechanics and field theory. The Stanford group, whose work is summarized in reference [Se86], has shown how nuclear matter saturation arises in a model field theory of nucleons and Lorentz scalar and vector (isoscalar) fields, with Lagrangian density:

$$\begin{aligned}\mathcal{L} = \overline{\psi}[\gamma_\mu(i\partial^\mu - g_V V^\mu) - (M - g_S\phi)]\psi + \tfrac{1}{2}(\partial_\mu\phi\partial^\mu\phi - m_s^2\phi^2) \\ - \frac{1}{4}F_{\mu\nu}F^{\mu\nu} + \tfrac{1}{2}m_V^2 V_\mu V^\mu + \delta\mathcal{L}\end{aligned} \tag{1.A.1}$$

Model	g_s^2	g_v^2	m_s (MeV)	m_v (MeV)
MFT	91.64	136.2	550.	783.
RHA	62.89	79.78	550.	783.

Table 1.1

Model parameters for QHD in two approximations. Coupling constants are found by adjusting to fit the saturation density and binding of nuclear matter. MFT is the mean field theory where vacuum fluctuations are ignored. RHA is the relativistic Hartree approximation including vacuum fluctuations.

where

$$F_{\mu\nu} = \partial_\mu V_\nu - \partial_\nu V_\mu \tag{1.A.2}$$

and $\delta\mathcal{L}$ stands for possible counterterm contributions to regularize the theory. Typical model parameters are given in Table 1.1.

In the mean field approximation (written here for a static, uniform system), the meson field operators in (1.A.1) are replaced by their ground state expectation values:

$$\phi \to \langle\phi\rangle \equiv \phi_0 \tag{1.A.3a}$$

$$V_\mu \to \langle V_\mu\rangle \equiv \delta_{\mu 0} V_0 \tag{1.A.3b}$$

resulting in the mean field equations

$$\phi_0 = \frac{g_s}{m_S^2}\langle\bar{\psi}\psi\rangle \equiv \frac{g_s}{m_S^2}\rho_s \tag{1.A.4a}$$

$$V_0 = \frac{g_V}{m_V^2}\langle\bar{\psi}\psi\rangle \equiv \frac{g_V}{m_V^2}\rho_B \tag{1.A.4b}$$

$$[i\partial\!\!\!/^\mu - g_V\gamma^0 V_0 - (M - g_S\phi_0)]\psi = 0 \tag{1.A.4c}$$

The theory can then be solved exactly, and it has now been extensively applied to nuclear matter and finite nuclei. Important results of these studies include:

a) The saturation property of nuclear matter, resulting from a balance of the attractive scalar field and the repulsive vector field. The saturation density and binding

energy of nuclear matter give the values of Table 1.1. The mean values of the meson fields in nuclear matter are

$$g_S\phi_0 \approx -400 \text{ MeV} \qquad g_V V_0 \approx +350 \text{ MeV} , \qquad (1.A.5)$$

values which are not small compared to the (free) nucleon mass and emphasize the need for relativistic dynamics. The scalar field shifts the mass of the nucleon to:

$$M \rightarrow M^* \equiv M - g_S\phi_0 \qquad (1.A.6)$$

b) In finite nuclei, the mean field theory reproduces the observed spin–orbit splittings of the nucleon levels and gives good agreement with the measured charge densities.

The field theory treatment of nuclear physics is appealing on formal grounds; relativistic quantum field theory is the only known consistent, Lorentz covariant way of treating dynamical systems. Since QHD is a theory for fermions, spin will be treated as a fundamental part of the dynamics, so that spin dependence of the interactions will arise naturally. Since it is Lorentz invariant, it will be applicable for all momenta; one of the original motivations for the development of QHD was the description of nuclear matter under conditions of high density (large Fermi momentum), as in astrophysical applications. But apart from these extreme conditions, there are good reasons to prefer a relativistic field theory treatment for ordinary nuclei and nuclear matter. Without using static potentials as a starting point, one can deal with the retardation of the NN interaction and meson exchange currents explicitly. And with an unambiguous way to arrive at measurable quantities from nucleon and meson degrees of freedom, the appearance of quark degrees of freedom in conventional nuclear processes will be clear.

A second approach to relativistic nucleon dynamics which also gives the large potentials of (1.A.5) comes from the work of Clark et al [Cl83a], who have studied the phenomenology of the Dirac equation for describing nucleon–nucleus elastic

scattering. In this work, the Dirac equation with phenomenological scalar and vector optical potentials replace the standard central and spin–orbit potentials of Schrödinger phenomenology. It was found that proton elastic data could be fit well by as many parameters as for the nonrelativistic phenomenology. Again, the scalar potential is of strength -400 MeV and vector field is of strength $+350$ Mev in the nuclear interior, with geometries following the nuclear densities. The relativistic potentials show less energy dependence than the nonrelativistic potentials. The Dirac potentials can be reduced to a Schrödinger–equivalent form where the central potential is roughly the sum of the scalar and vector potentials (see Appendix C), but an energy dependence is introduced by this reduction; the relation between the two descriptions can explain the energy dependence of the Schrödinger optical potentials.

It was later found that the strong relativistic optical potentials of the phenomenological fits could be *calculated* from a relativistic NN interaction and nuclear structure information by the Relativistic Impulse Approximation (RIA). This provides more evidence for the possibility of a complete relativistic treatment of the nucleon dynamics for proton scattering. The predictions of spin observables from these calculations agree very well with data.

Thus, relativistic treatments of nuclear physics have the following advantages:

1) Field theory treatments offer the possibility for unambiguous fully consistent calculations; they will be good for all momenta and interaction strengths and will incorporate spin as a natural part of the dynamics.

2) Mean field theory calculations can explain nuclear matter saturation and the spin–orbit splitting in finite nuclei in a simple and satisfatory way.

3) The impulse approximation provides a remarkably successful treatment of proton elastic scattering, so that there is the possibility that structure and reaction calculations can be united with the same dynamical basis.

In this thesis, I present two pieces of work on relativistic treatments of proton scattering and a shorter section on nuclear structure. Both of the proton scattering sections use the relativistic impulse approximation to calculate experimentally observable quantities for nucleon–nucleus scattering from the nucleon–nucleon scattering amplitudes. Relativity makes predictions about how the NN interaction is modified in the presence of many other nucleons, and the consequences for intermediate–energy experiments are shown.

Chapter 2 deals with elastic proton scattering from closed–shell nuclei, for which the relativistic approach has already been used with success. The present work improves on these first calculations in that it includes some features of the RIA which were previously omitted. These features significantly extend the energy range at which the RIA can be applied, and good agreement with proton data near 200 MeV is obtained.

Chapter 3 presents the first work of mapping out the nuclear response for quasielastic proton scattering, as calculated in a relativistic scheme. In this section we compare calculations for the scattering observables with and without the mass shift brought about by the scalar field, (1.A.6) to see if there is any signature of the relativistic effective mass, i.e. the enhanced lower components of the spinors. We find that there are such signatures, and when compared with the new quasielastic data, the results are favorable (though mixed) for the relativistic treatment.

Chapter 4 deals with electromagnetic probes of nuclear structure, in particular the magnetic moments of closed shell–plus–(or minus)–one nuclei. Static magnetic moments have presented a problem for relativistic structure calculations, but with more careful inclusion of many–body effects, this problem has been largely eliminated.

1.B Conventions

The notation for the various scattering amplitudes will adhere as closely as possible to that already used in the important publications in this field. There is *no* need for a new way of representing these.

Conventions for the Dirac matrices and spinors will be those of [Bj64], which are the same as those of [Se86] except for the normalization of the spinors, and these will be pointed out when the need arises.

Vector quantities without indices and not in boldface are generally four–vectors. Three–vectors will be written in boldface, and when these quantities are squared, it means, e.g.

$$Q^2 = Q_0^2 - \mathbf{Q}^2 = Q_0^2 - \mathbf{Q}\cdot\mathbf{Q}$$

This differs from what was used in [Mu87] but is in line with [Bj64].

Clebsch–Gordan coefficients, written as $\langle j_1\, m_1\, j_2\, m_2 | j_3\, m_3\rangle$ for $\mathbf{j}_1 + \mathbf{j}_2 = \mathbf{j}_3$ follow the Condon–Shortley phase convention. When $\mathbf{l}$ is added to $\mathbf{s}$ to give single–particle states of good j, use $\mathbf{j}_1 = \mathbf{l}$, $\mathbf{j}_2 = \mathbf{s}$, and $\mathbf{j}_3 = \mathbf{j}$

Generally, $\hbar = c = 1$ throughout.

1.C Relativistic NN Amplitudes

Chapters 2 and 3 will present calculations which take information from NN scattering and apply it to N-nucleus scattering, using relativistic dynamics and wavefunctions. These calculations will then require a relativistic description of the NN scattering data.

1.C.1 Nonrelativistic Representation of the Amplitude

The most general representation of the nucleon–nucleon scattering amplitude in the nonrelativistic setting is a Wolfenstein–type parametrization with 5 complex parameters at each lab energy and scattering angle. More precisely, this is the most general form consistent with rotation, parity, time–reversal and isospin invariance [Gl83].

If in the center of mass frame of the colliding nucleons the momenta and spins of incident particles 1 and 2 are $\mathbf{k}_c, s_1$ and $-\mathbf{k}_c, s_2$ and those of the outgoing particles, $1'$ and $2'$ are $\mathbf{k}'_c, s'_1$ and $-\mathbf{k}'_c, s'_2$, the on-shell amplitude f_c can be written:

$$(2ik_c)^{-1} f_c = A + B\sigma_1\cdot\sigma_2 + i|\mathbf{q}|C(\sigma_{1n} + \sigma_{2n}) + D\sigma_1\cdot\hat{q}\,\sigma_2\cdot\hat{q} + E\sigma_{1z}\sigma_{2z} \quad (1.C.1)$$

where $q = |\mathbf{k}'_c - \mathbf{k}_c|$. f_c is a *Pauli* operator which depends on q and $E_c = \sqrt{\mathbf{k}_c^2 + M^2}$; scattering amplitudes for particular spin orientations are found by operating on the initial and final Pauli spinors. Orthogonal directions $\hat{z}$, $\hat{q}$ and $\hat{n}$ are defined by:

$$\mathbf{k}_a = \tfrac{1}{2}(\mathbf{k}_c + \mathbf{k}'_c) \tag{1.C.2}$$

$$\hat{z} = \hat{k}_a \qquad\qquad \hat{n} = \hat{q} \times \hat{z} \tag{1.C.3}$$

The subscripts on the σ's indicate the spatial component and whether to operate between the $1'$ and 1 or the $2'$ and 2 spinors. The are five complex functions A,....,E for pp and five functions for nn scattering.

(Though not the way that the NN amplitude is most often quoted, form (1.C.1) is used in much of the literature related to the calculations in this thesis; it is trivially related to the more common representations of the amplitude; see Appendix A.)

The amplitude f_c is normalized so that the cross section is the square of f_c:

$$\left.\frac{d\sigma}{d\Omega_c}\right|_{\substack{1\to 1' \\ 2\to 2'}} = \left|\langle \chi^\dagger_{1'} \chi^\dagger_{2'} f_c \chi_1 \chi_2 \rangle\right|^2 \tag{1.C.4}$$

1.C.2 Relativistic Representation of the Amplitude

McNeil, Ray and Wallace [McN83a] equated on–shell matrix elements of a $4 \times 4 \otimes 4 \times 4$ matrix $\hat{\mathcal{F}}$ to the experimental NN amplitudes. The Pauli spinor χ_i matrix elements of Eq.(1.C.1) are equated to the positive energy matrix elements of a Dirac operator $\hat{\mathcal{F}}$, operating on the four-comonent spinors of the corresponding momenta and spins:

$$(2ik_c)^{-1} \chi^\dagger_{s'_1} \chi^\dagger_{s'_2} f_c(E,q) \chi_{s_1} \chi_{s_2} = \overline{U}(\mathbf{k}'_c, s'_1) \overline{U}(-\mathbf{k}'_c, s'_2) \hat{\mathcal{F}}(E_c, q) U(\mathbf{k}_c, s_1) U(-\mathbf{k}_c, s_2) \ . \tag{1.C.5}$$

where

$$U(k_c, s_1) = \sqrt{\frac{E_c + M}{2M}} \begin{pmatrix} 1 \\ \frac{\vec{\sigma}\cdot\mathbf{k}_c}{E_c + M} \end{pmatrix} \chi_{s_1} \tag{1.C.6}$$

which is normalized so that $\overline{U}U = 1$. Again, there is an isospin label for $\hat{\mathcal{F}}$, with $\hat{\mathcal{F}}_{pp}$ for pp scattering and $\hat{\mathcal{F}}_{pn}$ for pn scatterng. We will abbreviate the right side of (1.C.5) as $\overline{U}_{1'}\overline{U}_{2'}\hat{\mathcal{F}}U_1U_2$.

$\hat{\mathcal{F}}$ is an operator in the spinor space of the two particles and quite generally (before considering physical symmetries) has $4\times4\times4\times4 = 256$ components. So Eq.(1.C.5)) only determines a small subset of the components in $\hat{\mathcal{F}}$. Just as symmetries reduce the number of possible independent spin matrix elements of f_c to five (the functions $A(q,E_c)\ldots E(q,E_c)$ in Eq. (1.C.1)), isospin and time–reversal invariance reduce the independent components of $\hat{\mathcal{F}}$ to 44, for the on–shell amplitudes [Tj85]. So there will be an infinite number of operators $\hat{\mathcal{F}}$ with the same five on–shell matrix elements, but different $4\times4\otimes4\times4$ matrix structures. These different structures will give, for example, different negative energy spinor matrix elements of $\hat{\mathcal{F}}$. These ambiguities are important because we will use the full $\hat{\mathcal{F}}$, not just $\overline{U}_{1'}\overline{U}_{2'}\hat{\mathcal{F}}U_1U_2$ to construct an optical potential in the calculation of Chapter 2.

Thus, the information contained in the measurement of the NN amplitudes at a given energy— which gives the five complex Wolfenstein parameters— is not sufficient to determine the operator $\hat{\mathcal{F}}$ completely, so without further theoretical input, assumptions need to be made about the form of $\hat{\mathcal{F}}(q)$. These assumptions will determine the behavior of the NN amplitudes as the spinors U change. The choice for $\hat{\mathcal{F}}(q)$ made in the original RIA was:

$$\hat{\mathcal{F}}(q,E) = \sum_L F^L(q,E)\lambda^L_{(1)}\cdot\lambda^L_{(2)} \qquad (1.C.7)$$

where the L's stand for the Dirac matrix types listed in Table 1.2. For example, the tensor term contributes $F^T(q,E)\overline{U}_{1'}\sigma^{\mu\nu}U_1\ \overline{U}_{2'}\sigma_{\mu\nu}U_2$. With this form, one can derive a 5×5 nonsingular matrix relating the F^L to the 5 Wolfenstein parameters $A,\ldots,E$ (Ref. [McN83a]; see also Appendix A). We emphasize that only the free matrix elements of (1.C.5) are determined by the NN data while the "off–shell" operator is

$\hat{\mathcal{F}} = \sum_i F^i(q,E)\lambda^i_{(1)}\lambda^i_{(2)}$	
i	λ^i
S (Scalar)	1
V (Vector)	γ_μ
P (Pseudoscalar)	γ_5
A (Axial-Vector)	$\gamma_5\gamma_\mu$
T (Tensor)	$\sigma_{\mu\nu}$

Table 1.2

needed to construct an optical potential. Other assumptions for the form of $\hat{\mathcal{F}}$ are possible, in particular replacing γ^5 by $\frac{\not{q}\gamma^5}{2M}$ which gives the same result for the amplitudes when operating on free spinors but which will give a different $t\rho$ optical potential.

Chapter 2. Elastic Scattering; The Relativistic Impulse Approximation

2.A Introduction

2.A.1 Elastic Proton Scattering

Models for the NN interaction in the nuclear medium are tested particularly well by studying elastic scattering of protons from closed–shell nuclei, especially at intermediate energies. In such experiments an incoming proton beam, which may be polarized is scattered, leaving the target nucleus in its ground state. The polarization of the outgoing beam can also be measured.

These experiments allow us to focus on the NN interaction because:

a) Knowledge of excited states will not be important, and in fact, very detailed information on the structure of the ground state may not be necessary.

b) At intermediate energies (and small scattering angles) the scattering is dominated by single-collision processess, making impulse approximations possible.

c) Complete sets of high quality data now exist for the energy range 200-800 MeV, giving very strict limits on acceptable theoretical models.

At each lab energy and scattering angle, there are three independent measurements possible: The cross section $\frac{d\sigma}{d\Omega}$, and two spin observables, the analyzing power A_y and the spin rotation parameter Q. (See Appendix B, especially Fig. B.2 which gives a schematic of the spin measurements which give A_y and Q.)

2.A.2 Optical Potentials

The dynamics of proton–nucleus scattering is summarized by the optical potential. For Schrödinger dynamics, there are central and spin–orbit parts:

$$\left[-\frac{\nabla^2}{2M} + U_c(r) + U_{\rm so}(r)\vec{\sigma}\cdot\mathbf{L}\right]\psi_{\rm nonrel}(\mathbf{r}) = E\psi_{\rm nonrel}(\mathbf{r}) \qquad (2.A.1a)$$

$$U_{\rm Schr} = U_c(r) + U_{\rm so}(r)\vec{\sigma}\cdot\mathbf{L} \qquad (2.A.1b)$$

while in the relativistic case one deals with scalar, vector and a small tensor potential:

$$[\vec{\alpha}\cdot\mathbf{p} + U_0(r) + \beta(M + U_S(r)) - 2i\vec{\alpha}\cdot\hat{r}U_T(r)]\psi_{\rm rel}(\mathbf{r}) = E\psi_{\rm rel}(\mathbf{r}) \qquad (2.A.2a)$$

$$U_{\rm Dirac}(r) = U_0(r) + \beta U_S(r) - 2i\vec{\alpha}\cdot\hat{r}U_T(r) \qquad (2.A.2b)$$

Phenomenological studies of these potentials at low energies find $U_c(r)$ to have a real part of about –50 MeV and $U_{\rm so}(r)$ peaked at the nuclear surface with a value of about –1 MeV, while the real parts of $U_S(r)$ and $U_0(r)$ are of order –400 MeV and +350 MeV, respectively.

$U_{\rm Schr}$ and $U_{\rm Dirac}$ are both calculable from NN amplitudes and nuclear structure information by means of "impulse approximations", to be outlined in the next section. (As will be seen, the term "approximation" is something of a misnomer in the relativistic case.) Both types of resulting optical potentials give good agreement with experimental cross sections, but recently it was found that the simplest relativistic calculation did much better than the simple nonrelativistic calculations in predicting the spin observables A_y and Q.

It may well be that one must do better calculations of medium corrections for the nonrelativistic calculations to get agreement with the 500 MeV spin observables which is as good as the relativistic calculations; in any case, neither of the two simple impulse approximations works well at energies of $T_{\rm lab} \approx 200$ MeV and lower [Ra85]. In particular, the first relativistic calculations (with their simple extrapolations on the NN

amplitudes for large |q|) do not match the large–angle behavior of the spin observables in Pb, and neutron densities extracted from the impulse approximation show strong energy dependence.

To answer these questions about the applicability of the relativistic impulse approximation to lower energies, we have used models to add features of the RIA which were ignored in the first calculations. These include a proper handling of the antisymmetrization of the NN scattering matrix and its modification by the nuclear medium. In addition, we test the original form of the NN amplitude $\hat{\mathcal{F}}$ in (1.C.7) by choosing a form with better low–energy physics built in.

From these models, we choose one standard procedure for calculating the Dirac optical potentials for proton scattering at energies near 200 MeV from ^{12}C, ^{16}O, ^{40}Ca, ^{90}Zr and ^{208}Pb and compare them with all the available data.

2.B Nonrelativistic and Relativistic Impulse Approximations

2.B.1 KMT Theory

In 1959, Kerman McManus and Thaler [Ke59] developed a formalism for the scattering of intermediate–energy nucleons by nuclei, with the object of calculating nucleon–nucleus scattering in terms of nucleon–nucleon amplitudes. An approximation for the optical potential for elastic scattering was derived as follows:

Assume Schrödinger dynamics with two–body potentials between all nucleons, (in particular, between the projectile and the target nucleons). Then divide the Hamiltonian for the complete system into:

$$H = H_0 + V \qquad\qquad H_0 = H_N + K_0 \qquad\qquad (2.B.1)$$

where H_N is the Hamiltonian for the N nucleons in the target nucleus, K_0 is the kinetic energy operator of the incident particle, and

$$V = \sum_{i=1}^{N} v(\mathbf{r}_0, \mathbf{r}_i) \qquad\qquad (2.B.2)$$

is the sum of two–body interactions between the projectile at $\mathbf{r}_0$ and target nucleons at $\mathbf{r}_i$. The scattering matrix for nucleon–nucleus collisions obeys a Lippman–Schwinger equation:

$$T = T + V\frac{1}{E - H_0 + i\epsilon}T \ . \tag{2.B.3}$$

With $\mathcal{A}$ being the projection operator for antisymmetrized nuclear states, KMT define a nuclear medium NN scattering operator τ as the solution of:

$$\tau = v\left\{1 + \frac{\mathcal{A}}{E - K_0 - H_N + i\epsilon}\tau\right\} \tag{2.B.4}$$

to be contrasted with the free NN scattering operator t, which satisfies:

$$t = v\left\{1 + \frac{1}{E - K_0 - K_1 + i\epsilon}t\right\} \tag{2.B.5}$$

where K_1 is the kinetic energy operator for a target nucleon.

Then by combining (2.B.3), (2.B.4) and (2.B.5), KMT arrived at a first approximation for V (note: *not* for T):

$$V \approx (N-1)\tau \tag{2.B.6}$$

As a further approximation, the free NN matrix t is used in place of τ (the "impulse approximation") to give:

$$V \approx (N-1)t \tag{2.B.7}$$

The full expression for the optical potential for elastic scattering, using a nuclear ground state $|0\rangle$ normalized as $\langle 0|0\rangle = N$ is

$$U_{opt} = \left(\frac{N-1}{N}\right)\left\langle 0\left|\sum_{i=1}^{N} t_i\right|0\right\rangle \tag{2.B.8}$$

2.B.2 Relativistic Impulse Approximation

In 1983, McNeil et al. [McN83b] and Shepard et al. [Sh83] investigated the possibility that a *relativistic* formula analagous to (2.B.8) would give a good description

of nucleon scattering. They presented a hypothesis as to how this might take place: The NN scattering operator t_i in KMT is replaced by the Dirac operator $\hat{\mathcal{F}}_i$ introduced in Section 1.C, with the appropriate factors for normalization:

$$\hat{t}_i \longrightarrow -\frac{4\pi i p_{\rm cm}}{M}\hat{\mathcal{F}}_i \qquad (2.B.9)$$

where is $p_{\rm cm}$ is the magnitude of the three-momentum of the projectile in the nucleon–nucleus center of mass frame (optical potentials and scattering observables are calculated for this frame). The relativistic analog of (2.B.8) is:

$$U_{opt}(q,E) = -\frac{4\pi i p_{\rm cm}}{M}\left\langle 0\left|\sum_{i=1}^{N}\hat{\mathcal{F}}_i(q,E)\right|0\right\rangle \qquad (2.B.10)$$

The formula in complete analogy to (2.B.7) would include a properly symmetrized $\hat{\mathcal{F}}$, and the formula in analogy to (2.B.6) would also include modifications of the nuclear medium, but neither of these features were included in the first calculations [Sh83], [Cl83b]. Also, $\hat{\mathcal{F}}$ was chosen to be of the form (1.C.7), without examining any other form.

Eq. (2.B.10) is now commonly referred to as the Relativistic Impulse Approximation, although clearly it is a *hypothesis*, since there is no well–defined way of calculating higher–order terms. (However, see [Lu87].)

Calculations at $T_{\rm lab}$=500 MeV and $T_{\rm lab}$=800 MeV for proton scattering on ^{40}Ca and ^{208}Pb ([Sh83], [Cl83b]) are surprisingly successful, especially for the spin observables A_y ad Q which give quantitative agreement with data. The agreement is much better than the lowest–order nonrelativistic calculations. At lower energies, the simple implementation of (2.B.10) does not give such impressive agreement [Ra85].

Before inquiring about a next order formula for (2.B.10), it is worth investigating whether a better calculation of (2.B.10) will give good agreement over a larger range of projectile energies. These improvements then include a properly symmetrized $\hat{\mathcal{F}}$,

including medium modifications, and investigating the assumptions made in choosing form (1.C.7). This will be the subject matter of the rest of this chapter.

2.C Relativistic Love–Franey Model

In this section, I review a model which allows one to separate direct and exchange parts of the scattering amplitude, so that an antisymmetrized amplitude can be used in the relativistic impulse approximation. This model performs a separation of (1.C.5) into:

$$\langle \mathbf{k}_1' \, \mathbf{k}_2' | \hat{\mathcal{F}} | \mathbf{k}_1 \mathbf{k}_2 \rangle = \langle \mathbf{k}_1' \mathbf{k}_2' | \hat{t}(E) | \mathbf{k}_1 \mathbf{k}_2 \rangle + (-1)^T \langle \mathbf{k}_2' \mathbf{k}_1' | \hat{t}(E) | \mathbf{k}_1 \mathbf{k}_2 \rangle \qquad (2.C.1)$$

where now $\hat{t}(E)$ is the true NN scattering operator. T is the total isospin of the two–nucleon state before or after the collision.

In Ref. [Ho85], a model for this separation was presented which is mathematically simple and has a physical basis in the one–boson exchange mechanism. It also allows one to examine ambiguities in the form of $\hat{\mathcal{F}}$.

The NN amplitude is modeled as arising from the first Born approximation for the exchange of a set of "mesons" (see Fig. 2.1) whose parameters are fit to reproduce NN scattering data at separate energies. The mesons are of different Lorentz types (scalar, vector, tensor, pseudoscalar and axial vector) and isospins. The coupling constants are complex with a real coupling g_i^2 and an imaginary one $\overline{g}_i^2$. The small imaginary couplings are a purely phenomenological means of obtaining the imaginary amplitude. We use the nonrelativistic limit of the free spinors, so that the mesons have propagators of the form $\frac{1}{\mathbf{q}^2+m^2}$, and the meson-nucleon vertices have form factors $\frac{1}{1+\frac{\mathbf{q}^2}{\Lambda^2}}$ with separate m and Λ for the real and imaginary contributions to the amplitude, denoted respectively by $m,\overline{m}$ and $\Lambda,\overline{\Lambda}$. The parameters found for the real amplitude have a close correspondence with those of one-boson exchange potential fits [Ho72], [Ho75] to NN data.

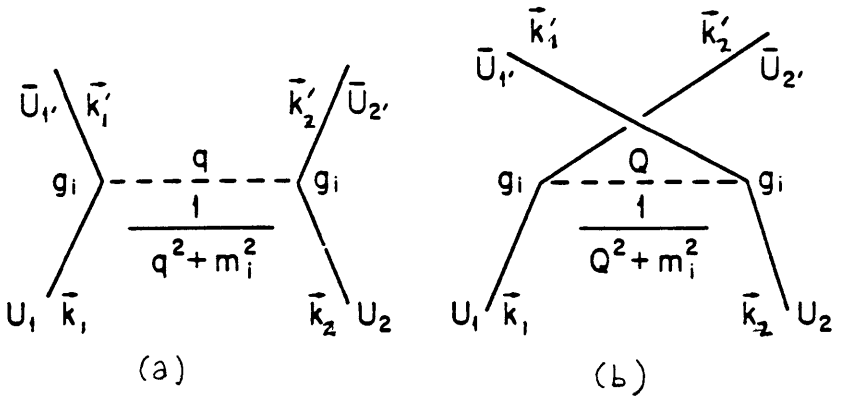

Fig. 2.1 Meson exchange diagrams for the relativistic Love–Franey model.

To calculate the NN amplitudes we consider the diagrams in Fig. 2.1 where the two interacting nucleons are identical particles in either a $T = 0$ or $T = 1$ total isospin state. The NN–meson vertex factor from the Feynman rules is assumed to be:

$$g_i \left(\frac{1}{1 + \frac{\mathbf{q}^2}{\Lambda_i^2}} \right) \lambda^{L(i)} (\vec{\tau})^{I_i} \tag{2.C.2}$$

where $L(i)$ denotes the Lorentz type of the i^{th} meson (see Table 1.2) and $I_i = (0, 1)$ is the meson's isospin. The $T = 0$ scattered wave is symmetric for space–spin interchange so there is a relative (+) sign between diagrams 2.1a and 2.1b. For $T = 1$ scattering, the wavefunction is antisymmetric and likewise there is a relative minus sign. Then up to overall kinematic factors, the contribution of meson i to the amplitude is:

$$\begin{aligned} \overline{U}_{1'}\overline{U}_{2'}\hat{\mathcal{F}}^i U_1 U_2 \propto & \frac{g_i^2}{m_i^2 + \mathbf{q}^2} \left(\frac{1}{1 + \frac{\mathbf{q}^2}{\Lambda_i^2}} \right)^2 \overline{U}_{1'} \lambda^{L(i)} U_1 \; \overline{U}_{2'} \lambda^{L(i)} U_2 \; \{\vec{\tau}_1 \cdot \vec{\tau}_2\}^{I_i} \\ & + (-1)^T \frac{g_i^2}{m_i^2 + \mathbf{Q}^2} \left(\frac{1}{1 + \frac{\mathbf{Q}^2}{\Lambda_i^2}} \right)^2 \overline{U}_{2'} \lambda^{L(i)} U_1 \; \overline{U}_{1'} \lambda^{L(i)} U_2 \; \{\vec{\tau}_1 \cdot \vec{\tau}_2\}^{I_i} \end{aligned} \tag{2.C.3}$$

where the direct and exchange momentum transfers are $\mathbf{q} = \mathbf{k}'_1 - \mathbf{k}_1$ and $\mathbf{Q} = \mathbf{k}'_2 - \mathbf{k}_1$. $\lambda^{L(i)} \cdot \lambda^{L(i)}$ has the same meaning as given in Table 1.2 and there is also a contribution to the imaginary part with the same form.

The first term in (2.C.3) is already of the form (1.C.7) from which we can identify the contributions to the F^L's in that expression (i.e. the standard form of the operator $\hat{\mathcal{F}}$). The second term is not of this form because of the different order of the spinors in the product. However, it can be rewritten with a Fierz transformation:

$$(\overline{U}_{2'}\lambda^L U_1)(\overline{U}_{1'}\lambda^L U_2) = \sum_{L'} c_{LL'}(\overline{U}_{1'}\lambda^{L'} U_1)(\overline{U}_{2'}\lambda^{L'} U_2) \qquad (2.C.4)$$

where

$$c_{LL'} = \frac{1}{8}\begin{pmatrix} 2 & 2 & 1 & -2 & 2 \\ 8 & -4 & 0 & -4 & -8 \\ 24 & 0 & -4 & 0 & 24 \\ -8 & -4 & 0 & -4 & 8 \\ 2 & -2 & 1 & 2 & 2 \end{pmatrix}, \qquad (2.C.5)$$

with rows and columns labelled in the order (S, V, T, A, P). So (2.C.3) becomes:

$$\overline{U}_{1'}\overline{U}_{2'}\hat{\mathcal{F}}^i U_1 U_2 \propto \frac{g_i^2}{m_i^2 + \mathbf{q}^2}\left(\frac{1}{1+\frac{\mathbf{q}^2}{\Lambda_i^2}}\right)^2 \{\tau_1 \cdot \tau_2\}^{I_i}\overline{U}_{1'}\lambda^{L(i)}U_1\overline{U}_{2'}\lambda^{L(i)}U_2$$

$$+ (-1)^T \frac{g_1^2}{m_i^2 + \mathbf{Q}^2}\left(\frac{1}{1+\frac{\mathbf{Q}^2}{\Lambda_i^2}}\right)^2 \{\tau_1 \cdot \tau_2\}^{I_i} \sum_{L'} c_{L(i)\,L'}\overline{U}_{1'}\lambda^{L'}U_1\ \overline{U}_{2'}\lambda^{L'}U_2 \qquad (2.C.6)$$

and the identification with the contributions to the invariants $F^S \ldots F^P$ can now be made. Note that while in the first ("direct") piece a meson always contributes to the F^L invariant of the same Lorentz type, this is not the case with the second ("exchange") term. For example, the pseudoscalar "meson", with $L(i) = P$ now contributes to the scalar invariant F^S because the Fierz matrix element $c_{P,S}$ is nonzero. So the "pion" of the model has an effect on the scalar optical potential from the exchange term.

With the spinor normalization used here ($\overline{U}U = 1$), the kinematic factor needed in (2.C.6) to give the free spinor matrix element as in Eqs. (1.C.5) and (1.C.7) is $\frac{iM^2}{2E_c k_c}$. Collecting all of these pieces, the total contribution to the invariant F^L from all of the N "mesons" is a sum of direct and exchange pieces:

$$F^L = i\frac{M^2}{2E_c k_c}[F_D^L(\mathbf{q}) + F_{Ex}^L(\mathbf{Q})] \qquad (2.C.7)$$

$$F_D^L = \sum_{i=1}^{N} \delta_{L,L(i)} \{\vec{\tau}_1 \cdot \vec{\tau}_2\}^{I_i} f^i(\mathbf{q}) \qquad (2.C.8a)$$

$$F_{Ex}^L = (-1)^T \sum_{i=1}^{N} c_{L(i),L} \{\vec{\tau}_1 \cdot \vec{\tau}_2\}^{I_i} f^i(\mathbf{Q}) \qquad (2.C.8b)$$

$$\text{where :} \quad f^i(\mathbf{q}) = f_R^i(\mathbf{q}) - i f_I^i(\mathbf{q})$$

$$f_R^i(\mathbf{q}) = \frac{g_i^2}{\mathbf{q}^2 + m_i^2} \left(1 + \frac{\mathbf{q}^2}{\Lambda_i^2}\right)^{-2} \qquad f_I^i = \frac{\overline{g}_i^2}{\mathbf{q}^2 + \overline{m}_i^2} \left(1 + \frac{\mathbf{q}^2}{\overline{\Lambda}_i^2}\right)^{-2} \qquad (2.C.9)$$

Finally, to get the invariant for pp and pn scattering,

$$F^L(pp) = F^L(T=1) \qquad (2.C.10a)$$

$$F^L(pn) = \frac{1}{2}[F^L(T=1) + F^L(T=0)] \qquad (2.C.10b)$$

To simplify the result a little further, define

$$t_D^L(\mathbf{q}) = \frac{iM^2}{2E_c k_c} F_D^L(\mathbf{q}) \qquad t_{Ex}^L(\mathbf{Q}) = \frac{iM^2}{2E_c k_c} F_{Ex}^L(\mathbf{Q}) \qquad (2.C.11)$$

then the Direct + Exchange separation of the amplitude is:

$$\begin{aligned}
\langle \mathbf{k}_1' \mathbf{k}_2' | \hat{\mathcal{F}} | \mathbf{k}_1 \mathbf{k}_2 \rangle &= \langle \mathbf{k}_1' \mathbf{k}_2' | \hat{t}(E) | \mathbf{k}_1 \mathbf{k}_2 \rangle + (-1)^T \langle \mathbf{k}_2' \mathbf{k}_1' | \hat{t}(E) | \mathbf{k}_1 \mathbf{k}_2 \rangle \\
&= \left\langle \mathbf{k}_1' \mathbf{k}_2' \left| \left(\frac{iM^2}{2E_c k_c}\right) \sum_L \left\{ F_D^L(\mathbf{q}) + F_{Ex}^L(\mathbf{Q}) \right\} \lambda_{(1)}^L \cdot \lambda_{(2)}^L \right| \mathbf{k}_1 \mathbf{k}_2 \right\rangle \\
&= (2\pi)^3 \delta^3(\mathbf{k}_1' + \mathbf{k}_2' - \mathbf{k}_1 - \mathbf{k}_2) \sum_L \lambda_{(1)}^L \cdot \lambda_{(2)}^L [t_D^L(\mathbf{q}) + t_{Ex}^L(\mathbf{Q})]
\end{aligned} \qquad (2.C.12)$$

where the functions $t_D(\mathbf{q})$ and $t_{Ex}(\mathbf{Q})$ are expressed in terms of the parameters of the model by Eqs. (2.C.7)–(2.C.11).

Values of the parameters found for this model are given in Tables 2.1-2.3. Note: the 200 and 400 MeV tables given here are not the same as those in [Ho85]; a correction

			Real			Imaginary		
Meson	Isospin	Lorentz Type	m	g^2	Λ	$\overline{m}$	$\overline{g}^2$	$\overline{\Lambda}$
π	1	P	138	13.205	565.77	500	-4.129	994.92
η	0	P	550	8.780	1386.82	1000	5.053	1162.15
σ	0	S	500	-6.314	1018.96	600	-2.702	572.39
ω	0	V	783	10.927	835.09	700	4.246	584.66
t_1	1	T	600	-.031	200.0	750	0.163	1139.03
a_1	1	A	800	-1.128	403.56	1000	0.487	865.60
δ	1	S	960	0.340	543.17	650	2.201	565.87
ρ	1	V	760	-.585	917.19	600	-1.749	557.28
t_0	0	T	800	0.334	2500.0	750	-.808	880.91
a_0	0	A	1275	2.271	1292.96	750	-1.891	933.15

Table 2.1

Meson parameters for $T_{\rm lab} = 200$ MeV. Parameters m, $\bar{m}$ and Λ, $\bar{\Lambda}$ are in MeV.

to the couplings has been applied to those values to make them consistent with the formalism in the present work. See Appendix A of [Mu87].

2.D Formalism for Direct + Exchange Optical Potentials for Finite Nuclei

2.D.1 General Result for $\langle \mathbf{r}|U_{\rm opt}|\psi\rangle$

The schematic expression for the Dirac optical potential U_{opt} in the RIA is:

$$U_{opt}(q,E) = -\frac{4\pi i p_{\rm cm}}{M}\langle\overline{\Psi}_2|\sum_i \hat{\mathcal{F}}_i(q,E)|\Psi_2\rangle \qquad (2.D.1)$$

where $\hat{\mathcal{F}}_i(q,E)$ is a two–particle Dirac operator, the antisymmetrized scattering amplitude for the scattering of the proton from target nucleon i. It is a function of the

			Real			Imaginary		
Meson	Isospin	Lorentz Type	m	g^2	Λ	$\overline{m}$	$\overline{g}^2$	$\overline{\Lambda}$
π	1	P	138	13.33	577.43	500	-2.205	473.95
η	0	P	550	3.391	2500	1000	4.989	2500
σ	0	S	500	-5.861	1008.2	600	-1.807	724.66
ω	0	V	783	9.825	862.17	700	2.948	685.89
t_1	1	T	600	0.122	650.57	750	0.066	2427.16
a_1	1	A	800	-.556	388.83	1000	0.049	200
δ	1	S	960	-.002	200	650	1.655	631.8
ρ	1	V	760	-.385	647.04	600	-1.258	633
t_0	0	T	800	0.006	200	750	-.356	691.1
a_0	0	A	1275	0.190	719.74	750	-.898	762.61

Table 2.2

Meson parameters for $T_{\rm lab} = 300$ MeV. Parameters m, $\bar{m}$ and Λ, $\bar{\Lambda}$ are in MeV.

momentum transfer q and the collision energy E, the center of mass energy of the nucleon pair. The customary choice for E in impulse approximation calculations is the "Breit–frame" energy, but in this work nuclear recoil is ignored so it is taken to be the center of mass energy for a stationary target nucleon and incident proton at the lab energy. $|\Psi_2\rangle$ is the full A–particle nuclear ground state.

Using the properly antisymmetrized scattering operator $\hat{t}$ in place of $\hat{\mathcal{F}}$, the *complete* expression for the $U_{\rm opt}$ *operator* acting on the full scattered wave $|\Psi_1\rangle$ is:

$$\langle \mathbf{r}|U_{opt}|\psi_1\rangle = \langle\overline{\Psi}_2|\mathbf{r}_1\cdots\mathbf{r}_A\rangle\left(-\frac{4\pi i p_{\rm cm}}{M}\right)\sum_i\Big\{\langle \mathbf{r}\,\mathbf{r}_i|\hat{t}(E)|\mathbf{r}'\,\mathbf{r}'_i\rangle + (-1)^T\langle \mathbf{r}_i\mathbf{r}|\hat{t}(E)|\mathbf{r}'\mathbf{r}'_i\rangle\Big\}$$
$$\cdot\prod_{j\neq i}\delta^3(\mathbf{r}'_j-\mathbf{r}_j)\langle\mathbf{r}'_1\cdots\mathbf{r}'_A|\Psi_2\rangle\langle\mathbf{r}'|\Psi_1\rangle \qquad (2.D.2)$$

			Real			Imaginary		
Meson	Isospin	Lorentz Type	m	g^2	Λ	$\overline{m}$	$\overline{g}^2$	$\overline{\Lambda}$
π	1	P	138	13.748	526.02	500	-1.263	473.95
η	0	P	550	-5.655	212.14	1000	3.029	2500
σ	0	S	500	-5.483	1266.60	600	-1.650	724.66
ω	0	V	783	8.530	1191.05	700	2.678	685.89
t_1	1	T	600	3.575	200.	750	-.025	2427.16
a_1	1	A	800	-.253	2500.	1000	-.127	200
δ	1	S	960	-.551	2500.	650	1.297	631.8
ρ	1	V	760	-.474	250.71	600	-.876	633
t_0	0	T	800	-.426	2500.	750	-.250	691.1
a_0	0	A	1275	8.855	331.23	750	-.539	762.61
t_1'	1	T	200	-.383	254.74			
t_0'	0	T	200	0.018	313.65			
a_1'	1	A	250	-.027	200.			
a_0'	0	A	250	-.369	2500.			
σ'	0	S	1000	0.622	216.16			
δ'	1	S	400	0.089	245.52			

Table 2.3

Meson parameters for $T_{\rm lab} = 400$ MeV. Parameters m, $\bar{m}$ and Λ, $\bar{\Lambda}$ are in MeV.

where integrations over all coordinates except for $\mathbf{r}$ are implied and T is the total isospin of the nucleons at $\mathbf{r}'$ and $\mathbf{r}_i$. We can decompose proton–proton and proton–neutron pairs into states of total isospin, as in (2.C.10). All the bras and kets in (2.D.2)) are *Dirac* eigenstates.

If the target wavefunction $\langle \mathbf{r}_1 \cdots \mathbf{r}_A | \Psi_2 \rangle$ is taken to be a Hartree product of

orbitals, this expression readily simplifies to:

$$\langle \mathbf{r}|U_{opt}|\psi_1\rangle = -\frac{4\pi i p_{\rm cm}}{M}\sum_{\alpha}\int d^3r_2' d^3r_2 d^3r_1 \langle\overline{\psi}_{2\,\alpha}|\mathbf{r}_2'\rangle \cdot\Big\{\langle \mathbf{r}\,\mathbf{r}_2'|\hat{t}(E)|\mathbf{r}_1'\,\mathbf{r}_2\rangle + (-1)^T\langle \mathbf{r}_2'\,\mathbf{r}|\hat{t}(E)|\mathbf{r}_1\mathbf{r}_2\rangle\Big\}\langle\mathbf{r}_2|\psi_2\rangle\langle\mathbf{r}_1|\psi_1\rangle \tag{2.D.3}$$

where the index α runs over the occupied proton and neutron orbitals and 1 and 2 go with "projectile" and "target".

The antisymmetrized coordinate–space element of $\hat{t}(E)$ is the Fourier transform of the momentum–space element, for which the Love–Franey model gives explicit expressions:

$$\langle \mathbf{r}_1'\,\mathbf{r}_2'|\hat{t}(E)|\mathbf{r}_1\,\mathbf{r}_2\rangle + (-1)^T\langle \mathbf{r}_2'\,\mathbf{r}_1'|\hat{t}(E)|\mathbf{r}_1\,\mathbf{r}_2\rangle = \int \frac{d^3k_2' d^3k_1' d^3k_2 d^3k_1}{(2\pi)^{12}} e^{i\mathbf{k}_1'\cdot\mathbf{r}_1'} e^{i\mathbf{k}_2'\cdot\mathbf{r}_2'} e^{-i\mathbf{k}_1\cdot\mathbf{r}_1} e^{-i\mathbf{k}_2\cdot\mathbf{r}_2} \cdot\Big\{\langle \mathbf{k}_1'\mathbf{k}_2'|\hat{t}(E)|\mathbf{k}_1,\mathbf{k}_2\rangle + (-1)^T\langle \mathbf{k}_1'\mathbf{k}_2'|\hat{t}(E)|\mathbf{k}_1\mathbf{k}_2\rangle\Big\} \tag{2.D.4}$$

At this point we use the Fierz reordering to get an expression with a single matrix element. The $\hat{t}$ operator is assumed to be of the form

$$\hat{t}(E) = \sum_L \lambda_{(1)}^L \cdot \lambda_{(2)}^L t^L(E) \tag{2.D.5}$$

where the meaning of "(1)" is the first argument in the bra and ket and "(2)" is for the second argument. As discussed in Section 2.C, we can write:

$$\langle \mathbf{k}_1'\,\mathbf{k}_2'|\hat{t}(E)|\mathbf{k}_1\mathbf{k}_2\rangle + (-1)^T\langle \mathbf{k}_2'\,\mathbf{k}_1'|\hat{t}(E)|\mathbf{k}_1\mathbf{k}_2\rangle = (2\pi)^3\delta^3(\mathbf{k}_1'+\mathbf{k}_2'-\mathbf{k}_1-\mathbf{k}_2)\sum_i \lambda_{(1)}^i\cdot\lambda_{(2)}^i[t_D^i(\mathbf{q}) + t_{Ex}^i(\mathbf{Q})] \tag{2.D.6}$$

where $\mathbf{q} = \mathbf{k}_1' - \mathbf{k}_1 = -\mathbf{k}_2' - \mathbf{k}_2$ and $\mathbf{Q} = \mathbf{k}_2' - \mathbf{k}_1 = \mathbf{k}_2 - \mathbf{k}_1'$. The functions $t_D(\mathbf{q})$ and $t_{Ex}(\mathbf{Q})$ were calculated in Section 2.C. (They depend only on $|\mathbf{q}|$ and $|\mathbf{Q}|$.) The sum on i, Lorentz types, with $\lambda^S = 1$, $\lambda^V = \gamma^0$ and $\lambda^T = \sigma^{\mu\nu}$ will be implied through this section.

Putting this into (2.D.4) gives:

$$\begin{aligned}
&\langle \mathbf{r}_1' \mathbf{r}_2' | t(E) | \mathbf{r}_1 \mathbf{r}_2 \rangle + (-1)^T \langle \mathbf{r}_2' \mathbf{r}_1' | \hat{t}(E) | \mathbf{r}_1 \mathbf{r}_2 \rangle \\
&\qquad = \frac{1}{(2\pi)^9} \int d^3k_1' d^3k_2' d^3k_1 d^3k_2 e^{i\mathbf{k}_1' \cdot \mathbf{r}_1'} e^{i\mathbf{k}_2' \cdot \mathbf{r}_2'} e^{-i\mathbf{k}_1 \cdot \mathbf{r}_1} e^{-i\mathbf{k}_2 \cdot \mathbf{r}_2} \\
&\qquad\qquad \cdot [t_D^i(\mathbf{q}) + t_{Ex}^i(\mathbf{Q})] \delta^3(\mathbf{k}_1' + \mathbf{k}_2' - \mathbf{k}_1 - \mathbf{k}_2) \lambda_{(1)}^i \cdot \lambda_{(2)}^i \\
&\qquad = \frac{1}{(2\pi)^9} \Big\{ \int d^3k_1 d^3k_2 d^3q e^{i(\mathbf{k}_1 + \mathbf{q}) \cdot \mathbf{r}_1'} e^{i(\mathbf{k}_2 - \mathbf{q}) \cdot \mathbf{r}_2'} e^{-i\mathbf{k}_1 \cdot \mathbf{r}_1} e^{-i\mathbf{k}_2 \cdot \mathbf{r}_2} t_D(\mathbf{q}) \\
&\qquad\qquad + \int d^3k_1 d^3k_2 d^3Q e^{i(\mathbf{k}_2 - \mathbf{Q}) \cdot \mathbf{r}_1'} e^{i(\mathbf{Q} + \mathbf{k}_1) \cdot \mathbf{r}_2'} e^{-i\mathbf{k}_1 \cdot \mathbf{r}_1} e^{-i\mathbf{k}_2 \cdot \mathbf{r}_2} t_{Ex}(\mathbf{Q}) \Big\}
\end{aligned} \tag{2.D.7}$$

In the second step, we have used the delta function in the $\mathbf{k}_2'$ integration and then since $\mathbf{k}_1' = \mathbf{q} + \mathbf{k}_1 = \mathbf{k}_2 - \mathbf{Q}$, the $\mathbf{k}_1'$ integration has been moved inside and replaced by:

$$\int d^3k_1' \to \int d^3q \qquad\qquad \int d^3k_1' \to \int d^3Q (\mathbf{Q} \to -\mathbf{Q})$$

for the two terms, respectively. Now if we do the remaining integrals in (2.D.7) we get delta function factors and Fourier transforms of t_D and t_{Ex}: define the r–space functions $t_{D,Ex}(\mathbf{r})$ by

$$t_{D,Ex}(\mathbf{r}) = \frac{1}{(2\pi)^3} \int d^3q \; t_{D,Ex}(\mathbf{q}) e^{-i\mathbf{q} \cdot \mathbf{r}} \,. \tag{2.D.8}$$

Then (2.D.7) becomes:

$$\begin{aligned}
&\langle \mathbf{r}_1' \mathbf{r}_2' | t(E) | \mathbf{r}_1 \mathbf{r}_2 \rangle + (-1)^T \langle \mathbf{r}_2' \mathbf{r}_1' | \hat{t}(E) | \mathbf{r}_1 \mathbf{r}_2 \rangle \\
&\qquad = \Big[t_D^i(|\mathbf{r}_2' - \mathbf{r}_1'|) \delta^3(\mathbf{r}_1' - \mathbf{r}_1) \delta^3(\mathbf{r}_2' - \mathbf{r}_2) \\
&\qquad\qquad + t_{Ex}^i(|\mathbf{r}_2' - \mathbf{r}_1'|) \delta^3(\mathbf{r}_2' - \mathbf{r}_1) \delta^3(\mathbf{r}_1' - \mathbf{r}_2) \Big] \lambda_{(1)}^i \cdot \lambda_{(2)}^i
\end{aligned} \tag{2.D.9}$$

Then putting this into (2.D.3) gives the optical potential:

$$\begin{aligned}
&\langle \mathbf{r}|U_{opt}|\psi_1\rangle \\
&= -\frac{4\pi i p_{\rm cm}}{M}\int d^3r_2' d^3r_2 d^3r_1 \sum_\alpha \{\overline{\psi}_{2\,\alpha}(\mathbf{r}_2')\lambda^i\psi_{2\,\alpha}(\mathbf{r}_2)\} \\
&\qquad \cdot \Big\{t_D^i(|\mathbf{r}_2'-\mathbf{r}|)\delta^3(\mathbf{r}-\mathbf{r}_2)\delta^3(\mathbf{r}_2'-\mathbf{r}_2) \\
&\qquad\qquad + t_{Ex}^i(|\mathbf{r}_2'-\mathbf{r}|)\delta^3(\mathbf{r}_2'-\mathbf{r}_1)\delta^3(\mathbf{r}-\mathbf{r}_2)\Big\}\ \lambda^i\psi_1(\mathbf{r}_1) \\
&= -\frac{4\pi i p_{\rm cm}}{M}\sum_\alpha \int d^3r_2 \left\{\overline{\psi}_{2\,\alpha}(\mathbf{r}_1)\lambda^i\psi_{2\,\alpha}(\mathbf{r})t_D^i(\mathbf{r}_2-\mathbf{r})\ \lambda^i\psi_1(\mathbf{r}_1)\right\} \\
&\qquad -\frac{4\pi i p_{\rm cm}}{M}\sum_\alpha \int d^3r_1 \left\{\overline{\psi}_{2\,\alpha}(\mathbf{r})\lambda^i\psi_{2\,\alpha}(\mathbf{r}_2)t_{Ex}^i(\mathbf{r}_1-\mathbf{r})\lambda^i\ \psi_1(\mathbf{r}_1)\right\}
\end{aligned} \tag{2.D.10}$$

Relabel the integration variables and define

$$\rho^i(\mathbf{r}',\mathbf{r}) = \sum_\alpha \overline{\psi}_{2\,\alpha}(\mathbf{r}')\lambda^i\psi_{2\,\alpha}(\mathbf{r})\ , \tag{2.D.11}$$

with

$$\rho^i(\mathbf{r}) \equiv \rho^i(\mathbf{r},\mathbf{r}) \tag{2.D.12}$$

the scalar, vector, etc. nucleon densities. Then the optical potential is:

$$\begin{aligned}
\langle \mathbf{r}|U_{opt}|\psi_1\rangle = -\frac{4\pi i p_{\rm cm}}{M}&\left[\int d^3r'\rho^i(\mathbf{r}')t_D^i(|\mathbf{r}'-\mathbf{r}|)\lambda^i\right]\psi_1(\mathbf{r}) \\
&-\frac{4\pi i p_{\rm cm}}{M}\int d^3r'\rho^i(\mathbf{r}',\mathbf{r})t_{Ex}^i(|\mathbf{r}'-\mathbf{r}|)\lambda^i\psi_1(\mathbf{r}')
\end{aligned} \tag{2.D.13}$$

The first term in (2.D.13) gives a multiplicative ("local") factor $U_D^i(r,E)$ which can be used in the Dirac equation with no further ado. The exchange term is of the form:

$$\int d^3r' U_{Ex}(\mathbf{r},\mathbf{r}')\psi_1(\mathbf{r}').$$

To use conventional methods for solving the Dirac (or Schrödinger– equivalent) equation, it is desirable to have an approximate *local* expression for the second term.

2.D.2 Local Approximation for Nonlocal Potential

To get an approximate *local* expression for the nonlocal term in (2.D.13), we need to relate the values of the scattered wave $\psi(\mathbf{r})$ at two different points in space. Of course, if $\psi(\mathbf{r})$ were a plane wave of momentum $\mathbf{k}$, this would be easy:

$$\psi_{\mathrm{pw},\mathbf{k}}(\mathbf{r}') = \psi_{\mathrm{pw},\mathbf{k}}(\mathbf{r})\, e^{-i\mathbf{k}\cdot(\mathbf{r}-\mathbf{r}')} \qquad (2.D.14)$$

A suitable approximation for the scattered wave ψ, apparently due to Austern [Au70], is to make a "local WKB approximation". First, calculate a "local momentum" $k = |\mathbf{k}|$ for the two points $\mathbf{r}$ and $\mathbf{r}'$ by:

$$\frac{\hbar^2 k^2}{2m} + U_L\left(\frac{\mathbf{r}'+\mathbf{r}}{2}\right) = E \qquad (2.D.15)$$

where $U_L(r)$ is an approximate local (Schrödinger–equivalent) potential and E is the projectile's kinetic energy. The direction of the "local momentum" is taken to follow some distribution $A(\hat{k})$, normalized so that

$$\int A(\hat{k}) d\hat{k} = 1$$

and then the relation between the wavefunction values comes from a weighted average of the phase differences:

$$\psi(\mathbf{r}') = \psi(\mathbf{r}) \int A(\hat{k})\, e^{-i\mathbf{k}\cdot(\mathbf{r}-\mathbf{r}')}\, d\hat{k} \qquad (2.D.16)$$

The simplest guess for $A(\hat{k})$ is to choose it to be a constant, $A = \frac{1}{4\pi}$. This gives

$$\psi(\mathbf{r}') = \psi(\mathbf{r}) j_0(|\mathbf{r}-\mathbf{r}'|k) \qquad (2.D.17)$$

and with this, (2.D.13) becomes:

$$\langle \mathbf{r}|U_{opt}|\psi_1\rangle = \Big\{ \int d^3r' \rho^i(\mathbf{r}') t_D(|\mathbf{r}'-\mathbf{r}|, E)\lambda^i + \int \rho^i(\mathbf{r}',\mathbf{r}) t^i_{Ex}(|\mathbf{r}'-\mathbf{r}|, E) j_0(|\mathbf{r}'-\mathbf{r}|k)\lambda^i \Big\} \psi_1(\mathbf{r}) \qquad (2.D.18)$$

2.D.3 Off–diagonal elements of density matrix

We still need a simple expression for $\rho^i(\mathbf{r},\mathbf{r}')$. This function is easily evaluated for uniform nuclear matter, and such an approximation could be used for the finite nucleus with the appropriate effective k_F chosen for each pair $(\mathbf{r},\mathbf{r}')$. Since k_F is related to the diagonal element of $\rho^B(\mathbf{r},\mathbf{r}')$ by:

$$\rho^B_{\rm nm}(\mathbf{r},\mathbf{r}) = \rho^B_{\rm nm}(\mathbf{r}) = \frac{2}{3\pi^2}k_F^3 \qquad (2.D.19)$$

and since $\rho^B(\mathbf{r})$ for the target nucleus is known at all points, it is simplest to let the effective k_F be the local value at the midpoint of $\mathbf{r}$ and $\mathbf{r}'$:

$$\rho^B(\tfrac{1}{2}[\mathbf{r}+\mathbf{r}']) \equiv \frac{2}{3\pi^2}k_F^3 \qquad (2.D.20)$$

This guess is the same as the first term of an expansion of $\rho(\mathbf{r},\mathbf{r}')$ proposed by Negele and Vautherin [Ne72].

With this local approximation for k_F, a local nuclear matter approximation for $\rho^i(\mathbf{r}',\mathbf{r})$ gives:

$$\rho^i(\mathbf{r}',\mathbf{r}) \approx \frac{4}{(2\pi)^3}\int_{k\le k_F} d^3k\ \overline{u}_{\mathbf{k}}\lambda^i u_{\mathbf{k}} e^{i\mathbf{k}\cdot(\mathbf{r}-\mathbf{r}')} \qquad (2.D.21)$$

where the spinors are normalized to give:

$$u^\dagger_{\mathbf{k}',s'}u_{\mathbf{k},s} = \delta_{s',s}\delta^3(\mathbf{k}'-\mathbf{k}) \qquad \overline{u}_{\mathbf{k}',s'}u_{\mathbf{k},s} = \frac{M^*}{E^*}\delta_{s',s}\delta^3(\mathbf{k}'-\mathbf{k}) \qquad (2.D.22)$$

For the vector case, $\lambda^i = \gamma_0$ the integral is easy, for then we have:

$$\rho^B(\mathbf{r}',\mathbf{r}) \approx 4\int_{k\le k_F}\frac{d^3k}{(2\pi)^3}e^{i\mathbf{k}\cdot(\mathbf{r}-\mathbf{r}')} \qquad (2.D.23)$$

Defining $s = |\mathbf{r}'-\mathbf{r}|$, this gives:

$$\begin{aligned}\rho^B(\mathbf{r}',\mathbf{r}) &\approx \frac{8k_F^3}{(2\pi)^2(sk_F)^3}\left(\sin(sk_F)-(sk_F)\cos(sk_F)\right)\\ &= \rho^B_{\rm nm}\left(\frac{\mathbf{r}'+\mathbf{r}}{2}\right)\frac{3}{(sk_F)^3}\left(\sin(sk_F)-(sk_F)\cos(sk_F)\right)\\ &= \rho^B_{\rm nm}\left(\frac{\mathbf{r}+\mathbf{r}'}{2}\right)3j_1(sk_F)\end{aligned} \qquad (2.D.24)$$

while for the scalar density we get:

$$\begin{aligned}\rho^S(\mathbf{r}',\mathbf{r}) &\approx \frac{4}{(2\pi)^3}\int_{k\le k_F} d^3k\,\overline{u}_{\mathbf{k}}u_{\mathbf{k}}e^{i\mathbf{k}\cdot(\mathbf{r}-\mathbf{r}')} \\ &= \frac{4}{(2\pi)^3}\int_{k\le k_F} d^3k\frac{M^*}{\sqrt{k^2+M^{*2}}}e^{i\mathbf{k}\cdot(\mathbf{r}-\mathbf{r}')}\end{aligned} \tag{2.D.25}$$

We want to use the same integral as in (2.D.23) to simplify the calculation, and so we want to pull the factor $\frac{M^*}{\sqrt{k^2+M^{*2}}}$ outside as an effective factor. We choose the value appropriate for $\mathbf{r}' \to \mathbf{r}$ which, from the definition of the effective k_F, is the ratio $\frac{\rho^S}{\rho^B}$ (for nuclear matter) evaluated at the midpoint of $\mathbf{r}'$ and $\mathbf{r}$:

$$\rho^S(\mathbf{r}',\mathbf{r}) = \frac{\rho^S_{\rm nm}\left(\frac{\mathbf{r}'+\mathbf{r}}{2}\right)}{\rho^B_{\rm nm}\left(\frac{\mathbf{r}'+\mathbf{r}}{2}\right)}\int_{k\le k_F}\frac{4\,d^3k}{(2\pi)^3}e^{i\mathbf{k}\cdot(\mathbf{r}-\mathbf{r}')} \tag{2.D.26}$$

Now using (2.D.24) we get:

$$\begin{aligned}\rho^S(\mathbf{r}',\mathbf{r}) &\approx \rho^S_{\rm nm}\left(\frac{\mathbf{r}'+\mathbf{r}}{2}\right)\frac{3}{(sk_F)^3}\left(\sin(sk_F)-sk_F\cos(sk_F)\right) \\ &= \rho^S_{\rm nm}\left(\frac{\mathbf{r}+\mathbf{r}'}{2}\right)3j_1(sk_F)\end{aligned} \tag{2.D.27}$$

Finally, in (2.D.24) and (2.D.27) we replace $\rho^B_{\rm nm}\left(\frac{\mathbf{r}'+\mathbf{r}}{2}\right)$ and $\rho^S_{\rm nm}\left(\frac{\mathbf{r}'+\mathbf{r}}{2}\right)$ by the tabulated values of $\rho^S\left(\frac{\mathbf{r}'+\mathbf{r}}{2}\right)$ and $\rho^B\left(\frac{\mathbf{r}'+\mathbf{r}}{2}\right)$ for the target nucleus. For ρ^B these are precisely the same thing, since that is where the local value of k_F came from, but for ρ^S this is another small approximation. So both density matrices have the same form, and the result is:

$$\rho^i(\mathbf{r}',\mathbf{r}) \approx \rho^i\left(\frac{\mathbf{r}'+\mathbf{r}}{2}\right)\frac{3}{(sk_F)^3}\left(\sin(sk_F)-sk_F\cos(sk_F)\right) \tag{2.D.28}$$

where k_F is defined by (2.D.19).

The other possibilities for ρ^i, particularly the tensor density ρ^T will be discussed in the next section. As it turns out, the $(0i)$ component of the tensor density is nonzero in spin-zero nuclei (and gives a tensor optical potential) whereas it is zero in nuclear

matter. So the discussion of this section gives no help for $\rho^{T(0i)}(\mathbf{r},\mathbf{r}')$. But we will use the approximation of (2.D.28) with i =Tensor for the small tensor density.

2.D.4 Relativistic Densities; the Tensor Potential

The nuclear densities from the Hartree calculation of Horowitz and Serot [Ho81] are used in constructing the optical potentials. The nuclear Dirac wavefunctions have radial and angular parts for upper and lower components:

$$\psi_\alpha(\mathbf{r}) = \psi_{n\kappa mt}(\mathbf{r}) = \begin{pmatrix} i\frac{G(r)}{r}\Phi_{\kappa m} \\ -\frac{F(r)}{r}\vec{\sigma}\cdot\hat{r}\Phi_{\kappa m} \end{pmatrix} \qquad (2.D.29)$$

where $\kappa = \pm(j+\frac{1}{2})$ for spin alligned $\binom{\text{antiparallel}}{\text{parallel}}$ to the total angular momentum; see [Se86]. The $\Phi_{\kappa m}$ are spin spherical harmonics normalized to give:

$$\sum_{m=-j}^{j} \Phi^\dagger_{\kappa m}\Phi_{\kappa m} = \left(\frac{2j+1}{4\pi}\right) \qquad (2.D.30)$$

Then the vector density (zero component) for the spherical spin–zero considered is a sum over occupied states,

$$\sum_\alpha^{\text{occ}} \overline{\psi}_\alpha(\mathbf{r})\gamma^0\psi_\alpha(\mathbf{r}) = \sum_a^{\text{occ}} \left(\frac{2j_a+1}{4\pi r^2}\right)(|G_a(r)|^2 + |F_a(r)|^2) \qquad (2.D.31)$$

and the scalar density is:

$$\sum_\alpha^{\text{occ}} \overline{\psi}_\alpha(\mathbf{r})\psi_\alpha(\mathbf{r}) = \sum_a^{\text{occ}} \left(\frac{2j_a+1}{4\pi r^2}\right)(|G_a(r)|^2 - |F_a(r)|^2)\ . \qquad (2.D.32)$$

Here, α labels the nucleon states and a labels the Hartree levels.

Now consider the $\mu\nu$ component of the tensor density; we will evaluate:

$$\rho^{T(\mu\nu)}(\mathbf{r}) = \sum_\alpha \overline{\psi}_\alpha(\mathbf{r})\sigma^{\mu\nu}\psi_\alpha(\mathbf{r}) \qquad (2.D.33)$$

Since $\sigma^{\mu\nu}$ is antisymmetric in μ and ν we need to look at only the cases $(\mu\nu) = (0i)$ and $(\mu\nu) = (ij)$ where $i,j = 1,2,3$.

First, the case $(\mu\nu) = (0i)$. Since

$$\sigma^{0i} = i \begin{pmatrix} 0 & \sigma^i \\ \sigma^i & 0 \end{pmatrix}$$

we get

$$\begin{aligned} \rho^{T(0i)}(r) &= \sum_\alpha G_\alpha(r) F_\alpha(r) \left\{ \Phi_\alpha^\dagger \sigma^i \vec{\sigma} \cdot \hat{r} \Phi_\alpha + \Phi_\alpha^\dagger \vec{\sigma} \cdot \hat{r} \sigma^i \Phi_\alpha \right\} \\ &= \sum_\alpha \sum_j G_\alpha(r) F_\alpha(r) [\sigma^i \sigma^j + \sigma^j \sigma^i] \hat{r}^j \Phi_\alpha \\ &= 2 \sum_\alpha \sum_j G_\alpha(r) F_\alpha(r) \delta^{ij} \hat{r}^j \Phi_\alpha^\dagger \Phi_\alpha \\ &= 2 \sum_a \frac{2j_a + 1}{4\pi r^2} G_a(r) F_a(r) \hat{r}^i \end{aligned} \tag{2.D.34}$$

Now take the case $(\mu\nu) = (ij)$. Since

$$\sigma^{ij} = \sum_k \epsilon^{ijk} \begin{pmatrix} \sigma^k & 0 \\ 0 & \sigma^k \end{pmatrix},$$

we get

$$\rho^{T(ij)} = \sum_\alpha \sum_k \epsilon^{ijk} \left\{ |G_\alpha(r)|^2 + |F_\alpha(r)|^2 \right\} \Phi_\alpha^\dagger \sigma^k \Phi_\alpha \tag{2.D.35}$$

But in a spin–saturated nucleus,

$$\sum_\alpha \Phi_\alpha^\dagger \sigma^k \Phi_\alpha = 0 \tag{2.D.36}$$

so only the $(0i)$ terms of $\rho^{T(\mu\nu)}$ contribute to the tensor potential.

In (2.D.18), the sum over all tensor components leaves only

$$\begin{aligned} \rho^{T(0i)} \sigma_{0i} + \rho^{T(i0)} \sigma_{i0} &= -2 \rho^{T(0i)} \sigma^{0i} \\ &= -2i \vec{\alpha} \cdot \hat{r} \sum_a \left(\frac{2j_a + 1}{4\pi r^2} \right) 2 G_a F_a \end{aligned} \tag{2.D.37}$$

where we have used $\sigma^{0i} = i\alpha^i$.

The remaining Lorentz density types vanish. The three-vector density is:

$$\begin{aligned} \rho^{V(\mu=i)} &= \sum_\alpha^{\text{occ}} \overline{\psi}_\alpha(\mathbf{r}) \gamma^i \psi_\alpha(\mathbf{r}) \\ &= \sum_\alpha^{\text{occ}} i \frac{G_\alpha F_\alpha}{r} \Phi_\alpha^\dagger [\sigma^i \vec{\sigma} \cdot \hat{r} - \vec{\sigma} \cdot \hat{r} \sigma^i] \Phi_\alpha \\ &= 0 \end{aligned} \tag{2.D.38}$$

and

$$\begin{aligned}\rho^P(r) &= \sum_{\alpha}^{\text{occ}} \overline{\psi}_\alpha(\mathbf{r})\gamma^5\psi_\alpha(\mathbf{r}) \\ &= \sum_{\alpha}^{\text{occ}} 2i\frac{G_\alpha F_\alpha}{r}[\Phi_\alpha^\dagger \vec{\sigma}\cdot\hat{r}\Phi_\alpha] \\ &= 0\end{aligned} \tag{2.D.39}$$

and

$$\begin{aligned}\rho^{A(\mu=i)} &= \sum_{\alpha}^{\text{occ}} \overline{\psi}_\alpha(\mathbf{r})\gamma^i\gamma^5\psi_\alpha(\mathbf{r}) \\ &= \sum_{\alpha}^{\text{occ}} \left[|G_\alpha|^2 + |F_\alpha|^2\right]\ \Phi_\alpha^\dagger\sigma^i\Phi_\alpha \\ &= 0\end{aligned} \tag{2.D.40}$$

for a spin–saturated nucleus. Finally,

$$\begin{aligned}\rho^{A(\mu=0)} &= \sum_{\alpha}^{\text{occ}} i\frac{G_\alpha F_\alpha}{r^2}\left[\Phi_\alpha^\dagger\vec{\sigma}\cdot\hat{r}\Phi_\alpha - \Phi_\alpha^\dagger\vec{\sigma}\cdot\hat{r}\Phi_\alpha\right] \\ &= 0\ ,\end{aligned} \tag{2.D.41}$$

identically.

2.E Pseudovector Coupling in the Direct + Exchange Model

We have examined the effect on the optical potential of using pseudovector coupling for the "pion" of this model, that is, replacing $\lambda^P = \gamma^5$ by $\lambda^P = \pm\frac{\not{q}\gamma^5}{2M}$. As noted above, this does not change the parameters obtained from the fit to the NN data because the free spinors U satisfy:

$$(\overline{U}_{1'}\gamma^5 U_1)(\overline{U}_{2'}\gamma^5 U_2) = -(\overline{U}_{1'}\frac{\not{q}\gamma^5}{2M}U_1)(\overline{U}_{2'}\frac{\not{q}\gamma^5}{2M}U_2) \tag{2.E.1a}$$

$$(\overline{U}_{2'}\gamma^5 U_1)(\overline{U}_{1'}\gamma^5 U_2) = -(\overline{U}_{2'}\frac{\not{Q}\gamma^5}{2M}U_1)(\overline{U}_{1'}\frac{\not{Q}\gamma^5}{2M}U_2) \tag{2.E.1b}$$

While the direct amplitude from λ^P still does not contribute to the optical potential, the new "off–shell" behavior of the exchange term will make a difference. We look at

the contribution to the optical potential from the exchange part of the pseudoscalar term in $\hat{t}(E)$ when this new coupling choice, $\frac{\not{q}}{2M}$, is used.

Go back to the full expression for the optical potential, now written out in momentum space. When the new coupling choice is used in $\hat{t}^P(E)$, the "pion" contribution to the optical potential is:

$$\begin{aligned}\langle \mathbf{k}|U_{opt}(E)|\psi_1\rangle\Big|_{\substack{P\,(pv)\\ Ex}} &= -\frac{4\pi i p_{\rm cm}}{M}\sum_\alpha (-1)^T \langle \overline{\psi}_{2\,\alpha}|\mathbf{k}_2'\rangle\langle \mathbf{k}_2'\mathbf{k}|\hat{t}^{P\,(pv)}(E)|\mathbf{k}_1\mathbf{k}_2\rangle \\ &\qquad\qquad \cdot\langle \mathbf{k}_2|\psi_{2\,\alpha}\rangle\langle \mathbf{k}_1|\psi_1\rangle \\ &= -\frac{4\pi i p_{\rm cm}}{M}\sum_\alpha \int d^3k_1\, d^3k_2\, d^3k_2 \left(-\overline{\psi}_{2\,\alpha}(\mathbf{k}_2')\frac{\not{Q}\gamma^5}{2M}\psi_1(\mathbf{k}_1)\right) \\ &\qquad \cdot\left(\overline{\psi}(\mathbf{k})\frac{\not{Q}\gamma^5}{2M}\psi_{2\,\alpha}(\mathbf{k}_2)\right) t_{Ex}^P(\mathbf{Q})\delta^3(\mathbf{k}+\mathbf{k}_2'-\mathbf{k}_1-\mathbf{k}_2)\end{aligned} \tag{2.E.2}$$

where $Q = k_2' - k_1$ and $\psi(\mathbf{k})$ is a plane wave of momentum $\mathbf{k}$.

The Fierz identity *can* be used here because (2.C.4) is a general relation for *any* 4–component objects between which the basic Dirac matrices may be sandwiched. When we use it on the terms in (2.E.2) in large parentheses, we find:

$$\begin{aligned}&\left(-\overline{\psi}_{2\,\alpha}(\mathbf{k}_2')\frac{\not{Q}\gamma^5}{2M}\psi_1(\mathbf{k}_1)\right)\left(\overline{\psi}(\mathbf{k})\frac{\not{Q}\gamma^5}{2M}\psi_{2\,\alpha}(\mathbf{k}_2)\right) \\ &\quad = \left(\overline{\psi}_{2\,\alpha}(\mathbf{k}_2')\frac{\not{Q}\gamma^5}{2M}\psi_1(\mathbf{k}_1)\right)\left(\overline{\psi}(\mathbf{k})\frac{\gamma^5\not{Q}}{2M}\psi_{2\,\alpha}(\mathbf{k}_2)\right) \\ &\quad = \frac{1}{4}\left(\overline{\psi}_{2\,\alpha}(\mathbf{k}_2')\frac{\not{Q}}{2M}\frac{\not{Q}}{2M}\psi_{2\,\alpha}(\mathbf{k}_2)\right)\left(\overline{\psi}(\mathbf{k})\psi(\mathbf{k}_1)\right) \\ &\qquad -\frac{1}{4}\left(\overline{\psi}_{2\,\alpha}(\mathbf{k}_2')\frac{\not{Q}}{2M}\gamma^0\frac{\not{Q}}{2M}\psi_{2\,\alpha}(\mathbf{k}_2)\right)\left(\overline{\psi}(\mathbf{k})\gamma_0\psi_1(\mathbf{k}_1)\right) \\ &\qquad\quad +\frac{1}{8}\left(\overline{\psi}_{2\,\alpha}(\mathbf{k}_2')\frac{\not{Q}}{2M}\sigma^{\mu\nu}\frac{\not{Q}}{2M}\psi_{2\,\alpha}(\mathbf{k}_2)\right)\left(\overline{\psi}(\mathbf{k})\sigma_{\mu\nu}\psi_1(\mathbf{k}_1)\right) \\ &\qquad\qquad +\cdots\end{aligned} \tag{2.E.3}$$

where the unwritten Fierz terms would give zero when the sum on α is performed, using the results of Section 2.D.4. We now approximate Q_0, the change in energy

of the struck particle for the exchange process to be much less than its change in momentum, $|\mathbf{Q}|$. Then in (2.E.3), we get:

$$\frac{\not{Q}}{2M}\frac{\not{Q}}{2M} = \frac{Q^2}{4M^2} \approx -\frac{\mathbf{Q}^2}{4M^2} \qquad (2.E.4a)$$

$$\frac{\not{Q}}{2M}\gamma^0\frac{\not{Q}}{2M} = \frac{2Q_0^2 - Q^2}{4M^2} \approx \frac{\mathbf{Q}^2}{4M^2} \qquad (2.E.4b)$$

$$\frac{\not{Q}}{2M}\sigma^{\mu\nu}\frac{\not{Q}}{2M} = \frac{1}{4M^2}\left(Q^2\sigma^{\mu\nu} + 2i[\not{Q}\gamma^\mu Q^\nu - \not{Q}\gamma^\nu Q^\mu]\right) \qquad (2.E.4c)$$

The contributions to the density from the second term in (2.E.4c) come from terms proportional to $Q_0 Q_i$, which are assumed small compared to the first term, so we have:

$$\frac{\not{Q}}{2M}\sigma^{\mu\nu}\frac{\not{Q}}{2M} \approx \frac{Q^2}{4M^2}\sigma^{\mu\nu} \approx -\frac{\mathbf{Q}^2}{4M^2}\sigma^{\mu\nu}\ . \qquad (2.E.5)$$

Now using (2.E.5) in (2.E.4) and substituting in (2.E.3), the result is:

$$\begin{aligned}\langle \mathbf{k}|U_{opt}|\psi_1\rangle = -\frac{4\pi i p_{\rm cm}}{M}\sum_\alpha \int d^3k_1\, d^3k_2'\, d^3k_2 \\ \cdot\Bigg[\left(-\frac{1}{4}\right)\{\overline{\psi}_{2\,\alpha}(\mathbf{k}_2')\psi_{2\,\alpha}(\mathbf{k}_2)\}\frac{\mathbf{Q}^2}{4M^2}t_{Ex}^P(\mathbf{Q})\overline{\psi}(\mathbf{k})\psi_1(\mathbf{k}_1) \\ +\left(-\frac{1}{4}\right)\{\overline{\psi}_{2\,\alpha}(\mathbf{k}_2')\gamma^0\psi_{2\,\alpha}(\mathbf{k}_2)\}\frac{\mathbf{Q}^2}{4M^2}t_{Ex}^P(\mathbf{Q})\overline{\psi}(\mathbf{k})\gamma_0\psi_1(\mathbf{k}_1) \\ -\left(\frac{1}{8}\right)\{\overline{\psi}_{2\,\alpha}(\mathbf{k}_2')\sigma^{\mu\nu}\psi_{2\,\alpha}(\mathbf{k}_2)\}\frac{\mathbf{Q}^2}{4M^2}t_{Ex}^P(\mathbf{Q})\overline{\psi}(\mathbf{k})\sigma_{\mu\nu}\psi_1(\mathbf{k}_1)\Bigg]\end{aligned} \qquad (2.E.6)$$

The corresponding momentum–space expression, when we use pseudoscalar coupling (omit $\pm\frac{\not{Q}}{2M}$) and do the Fierz transformation on (2.E.2) is:

$$\begin{aligned}\langle \mathbf{k}|U_{opt}|\psi_1\rangle = -\frac{4\pi i p_{\rm cm}}{M}\sum_\alpha \int d^3k_1\, d^3k_2'\, d^3k_2 \\ \cdot\Bigg[\left(\frac{1}{4}\right)\{\overline{\psi}_{2\,\alpha}(\mathbf{k}_2')\psi_{2\,\alpha}(\mathbf{k}_2)\}\, t_{Ex}^P(\mathbf{Q})\overline{\psi}(\mathbf{k})\psi_1(\mathbf{k}_1) \\ +\left(-\frac{1}{4}\right)\{\overline{\psi}_{2\,\alpha}(\mathbf{k}_2')\gamma^0\psi_{2\,\alpha}(\mathbf{k}_2)\}\, t_{Ex}^P(\mathbf{Q})\overline{\psi}(\mathbf{k})\gamma_0\psi_1(\mathbf{k}_1) \\ +\left(\frac{1}{8}\right)\{\overline{\psi}_{2\,\alpha}(\mathbf{k}_2')\sigma^{\mu\nu}\psi_{2\,\alpha}(\mathbf{k}_2)\}\, t_{Ex}^P(\mathbf{Q})\overline{\psi}(\mathbf{k})\sigma_{\mu\nu}\psi_1(\mathbf{k}_1)\Bigg]\end{aligned} \qquad (2.E.7)$$

The difference is that for scalar and tensor potentials, $t^P_{Ex}(\mathbf{Q})$ picks up a factor of $-\frac{\mathbf{Q}^2}{4M^2}$ while in the vector potential it picks up $\frac{\mathbf{Q}^2}{4M^2}$. Thus, in calculating optical potentials we insert these factors with $t^P_{Ex}(\mathbf{Q})$ for the choice of pseudovector coupling. This factor is much less than 1 and its inclusion improves the behavior of the nuclear matter Dirac optical potentials at low energy by making both scalar and vector potentials smaller in absolute value [Ho85].

2.F Summary

The coordinate space optical potential is calculated from:

$$U^i(r) = -\frac{4\pi i p_{\rm cm}}{M}\Big\{\int d^3r\,\rho^i(\mathbf{r})t^i_D(|\mathbf{r}-\mathbf{r}'|,E) + \int d^3r\rho^i(\mathbf{r},\mathbf{r}')t^i_{Ex}(|\mathbf{r}-\mathbf{r}'|,E)j_0(k|\mathbf{r}-\mathbf{r}'|)\Big\} \tag{2.F.1}$$

where $i = S,V,T$ which gives the Dirac optical potential to be used for scattering calculations:

$$U_{opt} = U^S - \gamma^0 U^V - 2i\vec{\alpha}\cdot\hat{r}U^T \tag{2.F.2}$$

In (2.F.1) the off–diagonal one–body density is approximated by

$$\rho^i(\mathbf{r},\mathbf{r}') = \rho^i(\tfrac{1}{2}(\mathbf{r}+\mathbf{r}'))\frac{3}{(sk_F)}j_1(sk_F) \tag{2.F.3}$$

where $s = |\mathbf{r}-\mathbf{r}'|$. We will make the simple choice $k = p_{\rm lab}$ for the "local momentum" k in the second term of (2.F.1). Finally, the r–space Direct and Exchange amplitudes t^i_D and t^i_{Ex} are calculated from the Fourier transform of (2.C.18). This last step involves the Fourier transforms of the functions $f(\mathbf{q})$ in (2.C.16).

$$f(\mathbf{q}) = \frac{g^2}{\mathbf{q}^2+m^2}\left(1+\frac{\mathbf{q}^2}{\Lambda^2}\right)^{-2} \tag{2.F.4}$$

for which we use:

$$\int \frac{d^3q}{(2\pi)^3}e^{i\mathbf{q}\cdot\mathbf{r}}f(\mathbf{q}) = \frac{g^2}{4\pi}\frac{\Lambda^2}{(\Lambda^2-m^2)}\left\{\frac{\Lambda^2}{(\Lambda^2-m^2)}\frac{(e^{-mr}-e^{-\Lambda r})}{r} - \frac{\Lambda}{2}e^{-\Lambda r}\right\} \tag{2.F.5}$$

	SCALAR		VECTOR	
Energy (MeV)	Real	Imag.	Real	Imag.
200	-0.008	0.098	0.061	0.207
400	-0.043	0.061	-0.012	0.089

Table 2.4

Pauli Blocking Correction Factors a_i (see Eq. (2.G.1)

except for the Exchange contribution from the Pseudoscalar invariant when we use pseudovector coupling. Then we need the Fourier transform with a factor of $\frac{\mathbf{q}^2}{4M^2}$:

$$\int \frac{d^3q}{(2\pi)^3} e^{i\mathbf{q}\cdot\mathbf{r}} \frac{\mathbf{q}^2}{4M^2} f(\mathbf{q}) = \frac{g^2}{4\pi} \frac{\Lambda^2}{4M^2} \frac{\Lambda^2}{(\Lambda^2 - m^2)} \cdot \left\{ \frac{m^2}{(\Lambda^2 - m^2)} \frac{(e^{-\Lambda r} - e^{-mr})}{r} + \frac{\Lambda}{2} e^{-\Lambda r} \right\} \tag{2.F.6}$$

2.G Pauli Blocking Corrections

We now correct the optical potentials of Eq. (2.F.1) for medium modifications from Pauli blocking. Relativistic Brueckner theory calculations (similar to Ref. [Ho87]) of $U_{\rm opt}$ have been performed for infinite nuclear matter. These calculations use the HEA [Ho72] one-boson exchange potential and do not include binding energy (dispersion) corrections. The results with the Pauli exclusion operator, U_{pb} at various densities can be well represented by

$$U^i_{pb}(r) = \left[1 - a_i(T_{\rm lab}) \left(\frac{\rho_B(r)}{\rho_0} \right)^{\frac{2}{3}} \right] U^i(r) \tag{2.G.1}$$

Here, U^i is the optical potential calculated without the Pauli operator, and $\rho_0 = .1934\ fm^{-3}$. The approximate k_F^2 or $\rho_B^{\frac{2}{3}}$ density dependence agrees with phase space results for isotropic scattering. Therefore the nuclear matter calculations give Pauli blocking factors $a_i(T_{\rm lab})$ for each energy $T_{\rm lab}$. These are collected in Table 2.4 and are different for the real and imaginary parts of the scalar and vector potentials. (We omit Pauli blocking for the small tensor potential.)

At 200 MeV the imaginary potentials are Pauli blocked by about 10 percent while the change in the real potentials is smaller. Note, because a_i is different for i = scalar and vector, the effect on the Schrödinger equivalent imaginary potential, which involves cancellations (see Section 2.H, Eq. (2.H.1a)) is larger.

We use these nuclear matter results in a local density approximation to correct our finite nucleus optical potentials. Potentials from (2.F.1) are simply multiplied as in Eq. (2.G.1), where the baryon density is taken to be the $\rho_B(r)$ of the target. We find that the $\frac{2}{3}$ exponent in Eq. (2.G.1) is not critical for the results in Section 2.H.

Section 2.H Results

2.H.1 Dirac Potentials

Before presenting scattering observables, we look at the optical potentials in order to show the importance of some features of the model and compare with optical potentials from other approaches. In the last section it was noted how the scalar and vector optical potentials in nuclear matter decrease in strength when psedovector pion coupling is used in place of pseudoscalar coupling. Fig. 2.2 shows the same effect for ^{90}Zr at 200 MeV. We have used pseudovector coupling only for the real part of the optical potential, being guided by known pion–nucleon interactions. For the imaginary part, we leave the original MRW amplitude alone and use a pseudoscalar invariant. (If a pseudovector imaginary potential is used instead, the changes in observables are very small.) The further effect of Pauli blocking is also shown.

In Fig. 2.3 we compare our relativistic optical potential for ^{40}Ca at 200 MeV, (using pseudovector coupling and including the Pauli correction) with a phenomenological Wood–Saxon fit to scattering data by Clark et al. [Cl83a]. The agreement is very good, considering the uncertainty in the phenomenological fit.

To compare our results with the optical potentials from nonrelativistic models, we calculate the "Schrödinger–equivalent" potentials which follow from the relativistic scalar and vector types. These are functions which play the same role as the

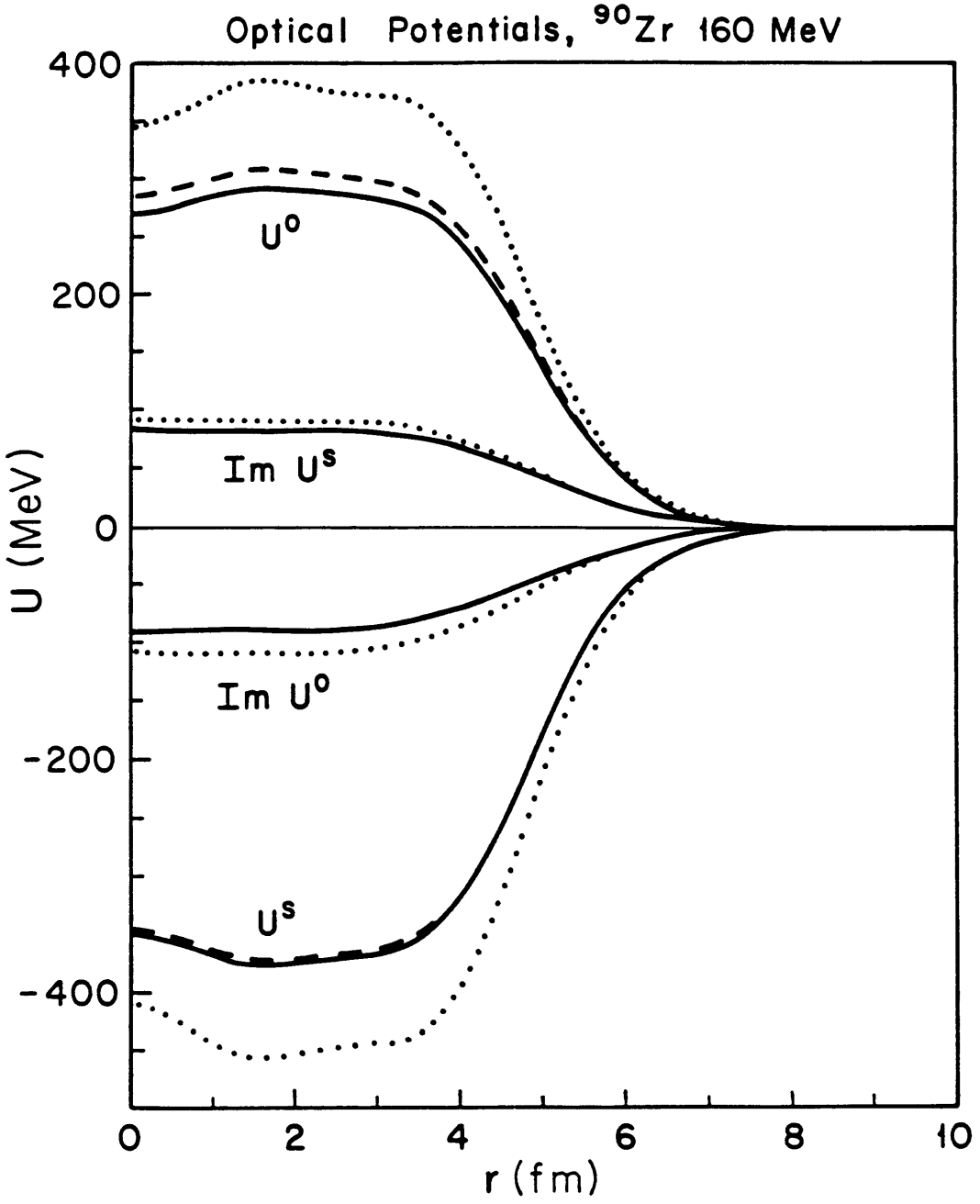

Fig. 2.2 Optical potentials for ^{90}Zr at 160 MeV. The dotted curves use pseudoscalar coupling without the Pauli blocking factor. The dashed curves use pseudovector coupling instead; the solid curves use pseudovector coupling and include the Pauli blocking factor.

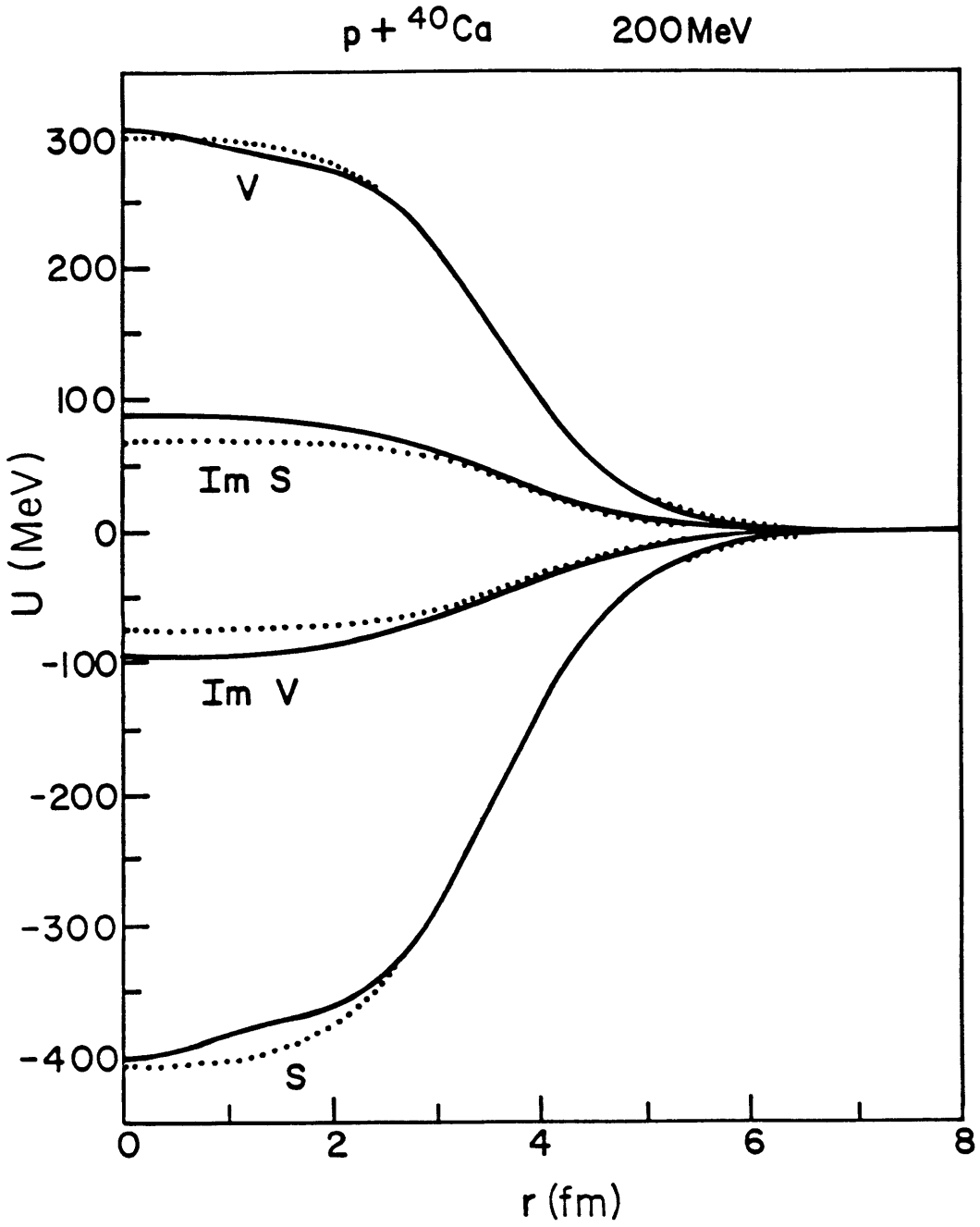

Fig. 2.3 Relativistic optical potentials for ^{40}Ca at 200 MeV. The solid curve is the microscopic calculation. The dotted curve is a phenomenological fit of Clark et al [Cl83a]

nonrelativistic potential when the Dirac equation for the projectile is written as a second order equation for the upper components [Cl83a]. Ignoring the small tensor and Coulomb potentials, the relation between the nonrelativistic central U_c and spin–orbit U_{so} potentials and the relativistic ones is:

$$U_c \approx \frac{1}{2E}[2EU^V + 2MU^S - (U^V)^2 + (U^S)^2] + U_{\text{Darwin}} \qquad (2.H.1a)$$

$$U_{so} \approx \frac{1}{2E}\left[-\frac{1}{rA}\left(\frac{\partial A}{\partial r}\right)\right] \qquad (2.H.1b)$$

where

$$U_{\text{Darwin}} = \frac{1}{2E}\left[-\frac{1}{2r^2A}\frac{\partial}{\partial r}\left(r^2\frac{\partial A}{\partial r}\right) + \frac{3}{4A^2}\left(\frac{\partial A}{\partial r}\right)^2\right] \qquad (2.H.2)$$

and

$$A = \frac{(E + U^S - U^V + M)}{(E + M)} \qquad (2.H.3)$$

Fig. 2.4 compares the Schrödinger-like potential for ^{208}Pb from our model with the nonrelativistic Paris G–matrix calculation of Ref. [Ri85]. The relativistic calculation gives a real central potential which is about 30 MeV more positive and has a non-Wood-Saxon shape, and a real spin orbit potential which is much stronger than the nonrelativistic result.

2.H.2 200 MeV Observables

In Figs. 2.5 through 2.12 we show the predictions of our model for the cross–section and spin observables A_y and Q for proton–nucleus scattering, at energies near 200 MeV. Experimental points, where available are also shown. The spin rotation, Q, data for ^{12}C, ^{16}O, ^{40}Ca, and ^{48}Ca are *preliminary* results from IUCF [St85]. For the heavier nuclei ^{90}Zr and ^{208}Pb, there are as yet no published Q data measured at 200 MeV. However, there is preliminary TRIUMF data for Zr and Pb at 200 MeV [Hi87], and there is TRIUMF data for ^{208}Pb at 290 MeV [Ha85].

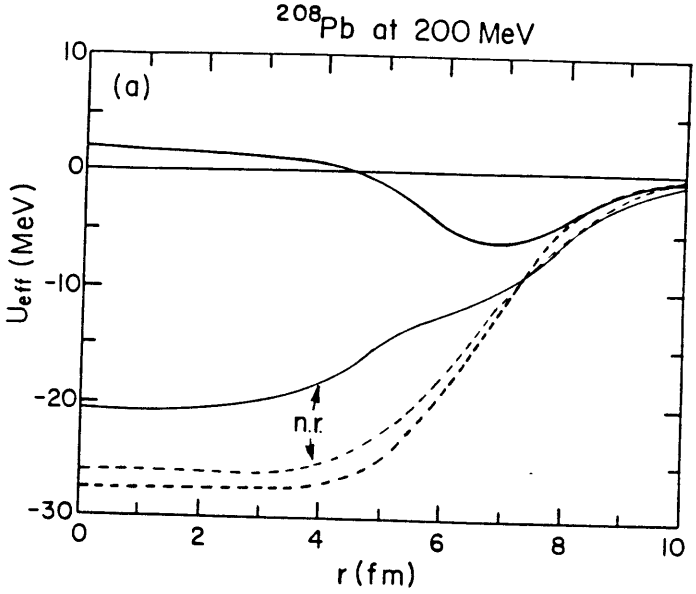

(a)

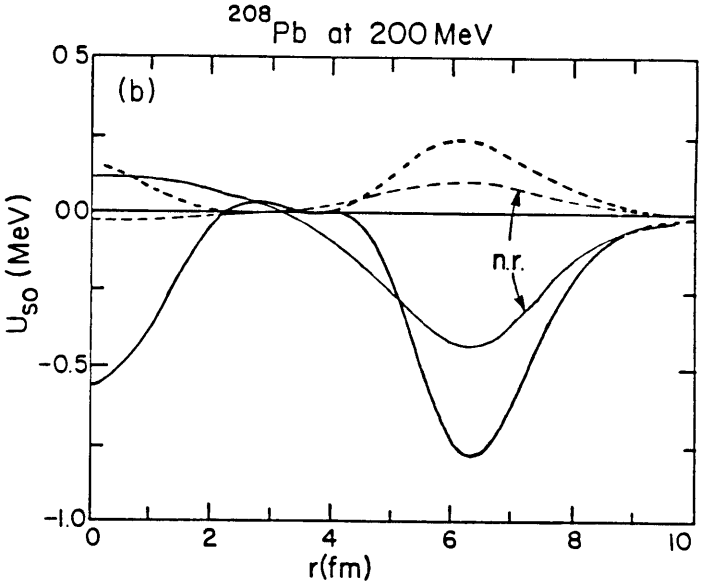

(b)

Fig. 2.4 Schrödinger potentials for ^{208}Pb at 200 MeV. Schrödinger–equivalent potentials, Eqs. (2.H.1a–2.H.3), from the relativistic calculation (heavy curves) are compared with the nonrelativistic (n.r.) results of Rikus and von Geramb [Ri85] (thin curves). Fig. 2.4a compares central and 2.4b compares spin–orbit potentials. Real potentials are solid and imaginary dashed curves.

Nucleus	$T_{\rm lab}$ (MeV)	$\sigma_{\rm total}$ (fm^2)
^{12}C	200	23.6
^{16}O	200	29.6
^{16}O	318	28.1
^{40}Ca	200	57.1
^{48}Ca	200	67.0
^{90}Zr	160	98.0
^{208}Pb	200	176.3
^{208}Pb	300	171.2
^{208}Pb	400	167.2

Table 2.5

Total reaction cross sections for calculations with pseudovector coupling and Pauli blocking.

For our calculations, we have chosen pseudovector coupling for the "pion" of the model (for its contribution to the real optical potential). We have not included the small tensor potential in the scattering calculations (but see the discussion of ^{48}Ca below). For the baryon and scalar densities of Eqs. (2.27) and (2.29) we have used those of Horowitz and Serot [Ho81]. The scattering observables calculated with these conventions are shown by the solid curves of Figs. 2.5 through 2.10 and Fig. 2.15. Total reaction cross sections for this set of calculations are given in Table 2.5.

Generally, the calculations match the data quantitatively up to about 60°, beyond which there is some trouble with the magnitude of the cross sections and the phase of the spin observables. The spin observables A_y and Q are very well reproduced both in the magnitudes and phases of the oscillations. This agreement includes the forward angle region in Q where results are very sensitive to the optical potentials. Agreement is greatly improved over the original RIA without explicit exchange or Pauli blocking [Ra85]. In Section 2.I we compare our results with other microscopic calculations.

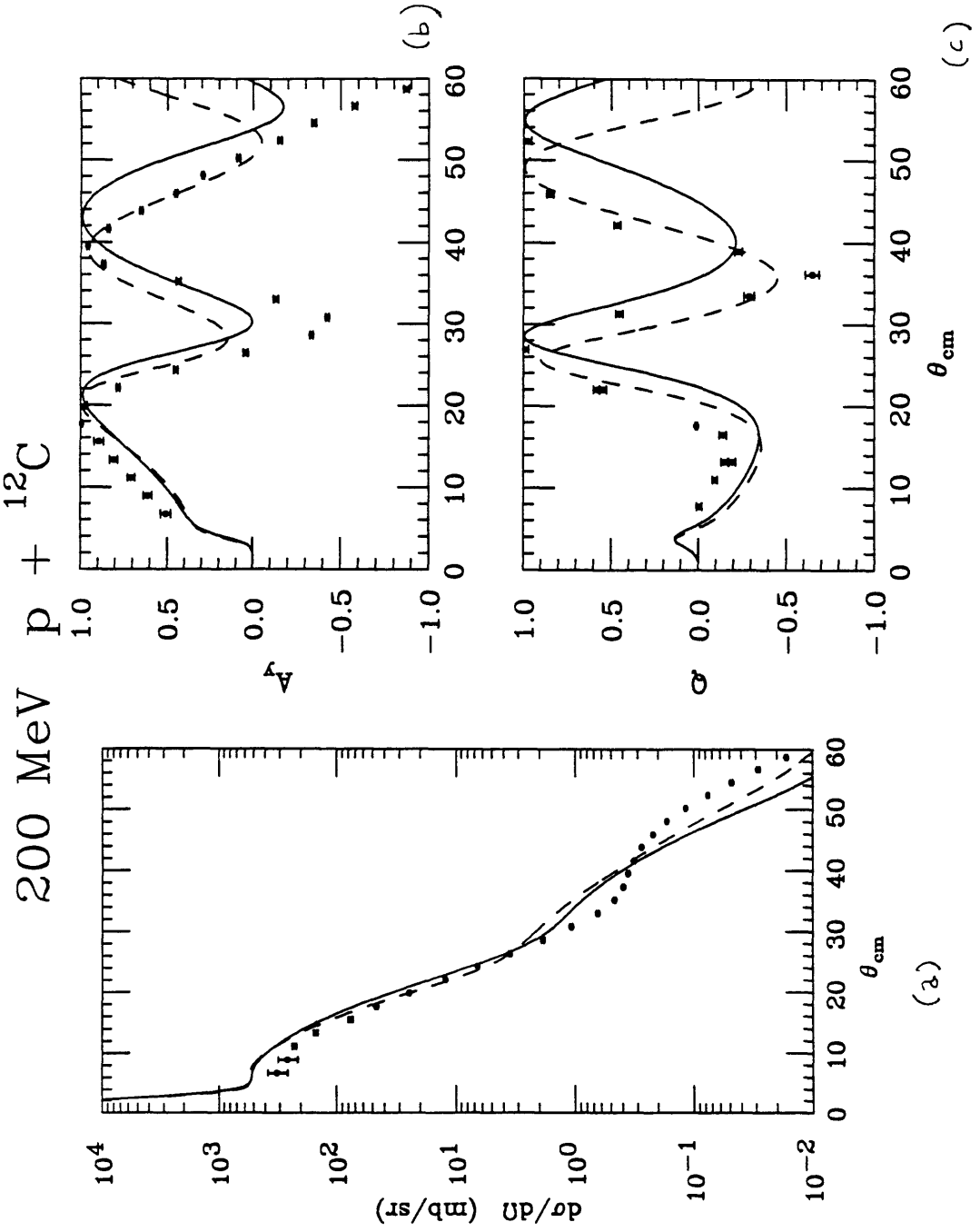

Fig. 2.5 Cross section (a), analyzing power (b) and spin rotation parameter (c) for 200 MeV ^{12}C scattering. The solid curves use Hartree densities. The dashed curves use empirical densities described in section III.C. Preliminary Q data are from Ref. [St85].

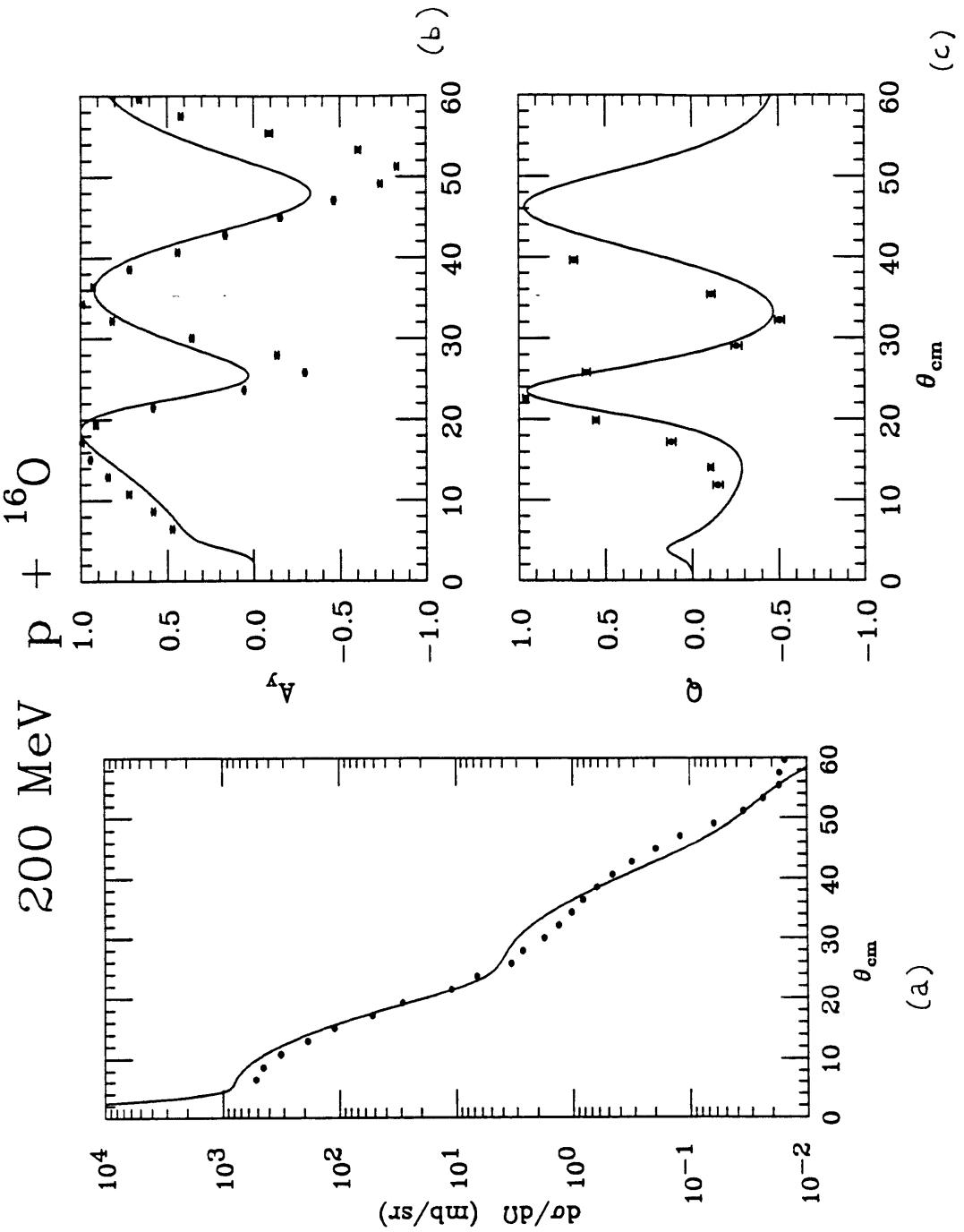

Fig. 2.6 Cross section (a), analyzing power (b) and spin rotation parameter (c) for 200 MeV ^{16}O scattering. Q data are from Ref. [St85].

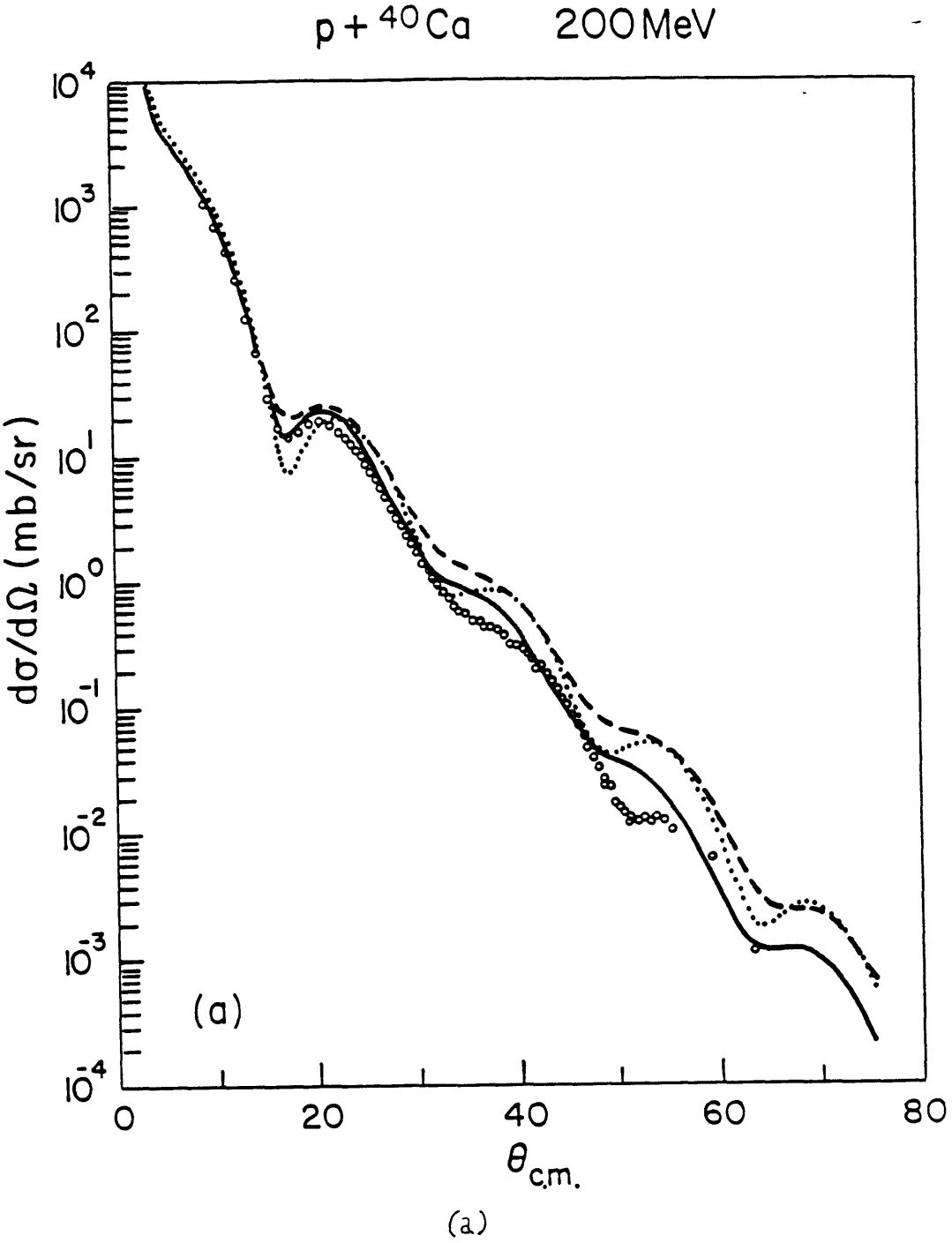

Fig. 2.7 Cross section (a), analyzing power (b) and spin rotation parameter (c) for 200 MeV ^{40}Ca scattering. The dashed curves use pseudoscalar coupling and include Pauli blocking. The dotted curves use pseudovector coupling but omit Pauli blocking. Data is from Ref. [St85].

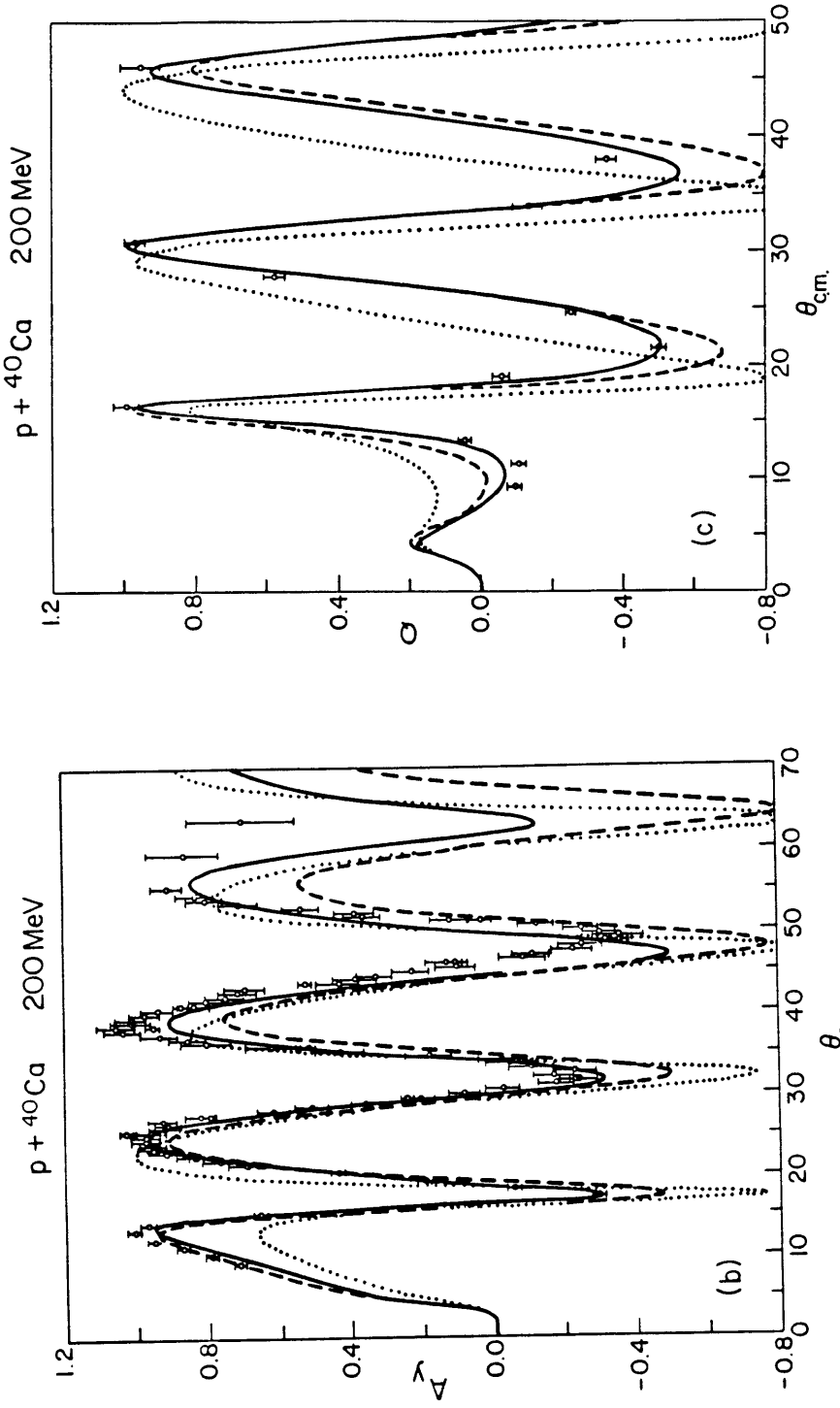
p + 40Ca 200 MeV
(b)
Ay
θc.m.
p + 40Ca 200 MeV
(c)
σ
θc.m.

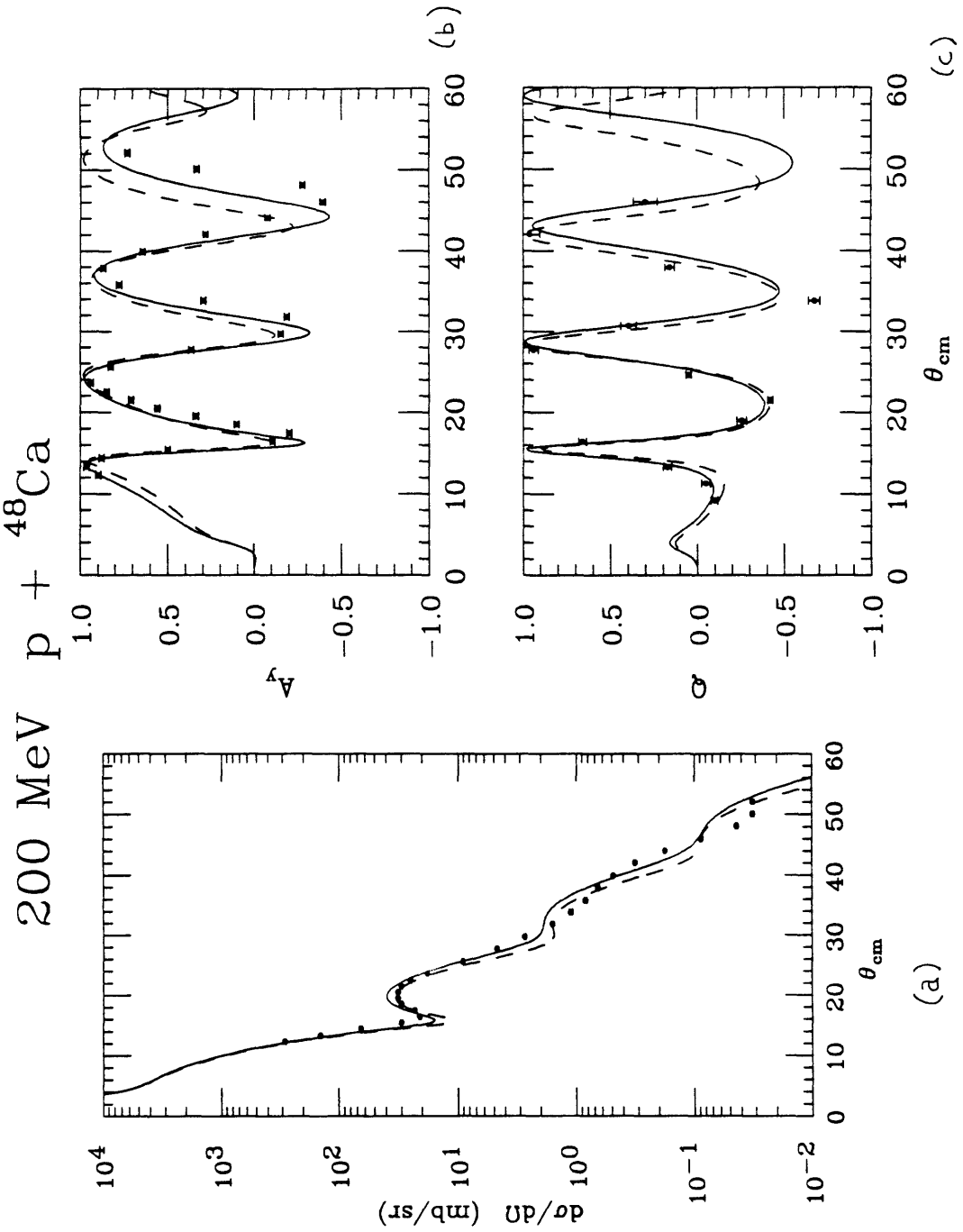

Fig. 2.8 Cross section (a), analyzing power (b) and spin rotation parameter (c) for 200 MeV ^{48}Ca scattering. The dotted curves include a small tensor potential. Data are from Ref. [St85].

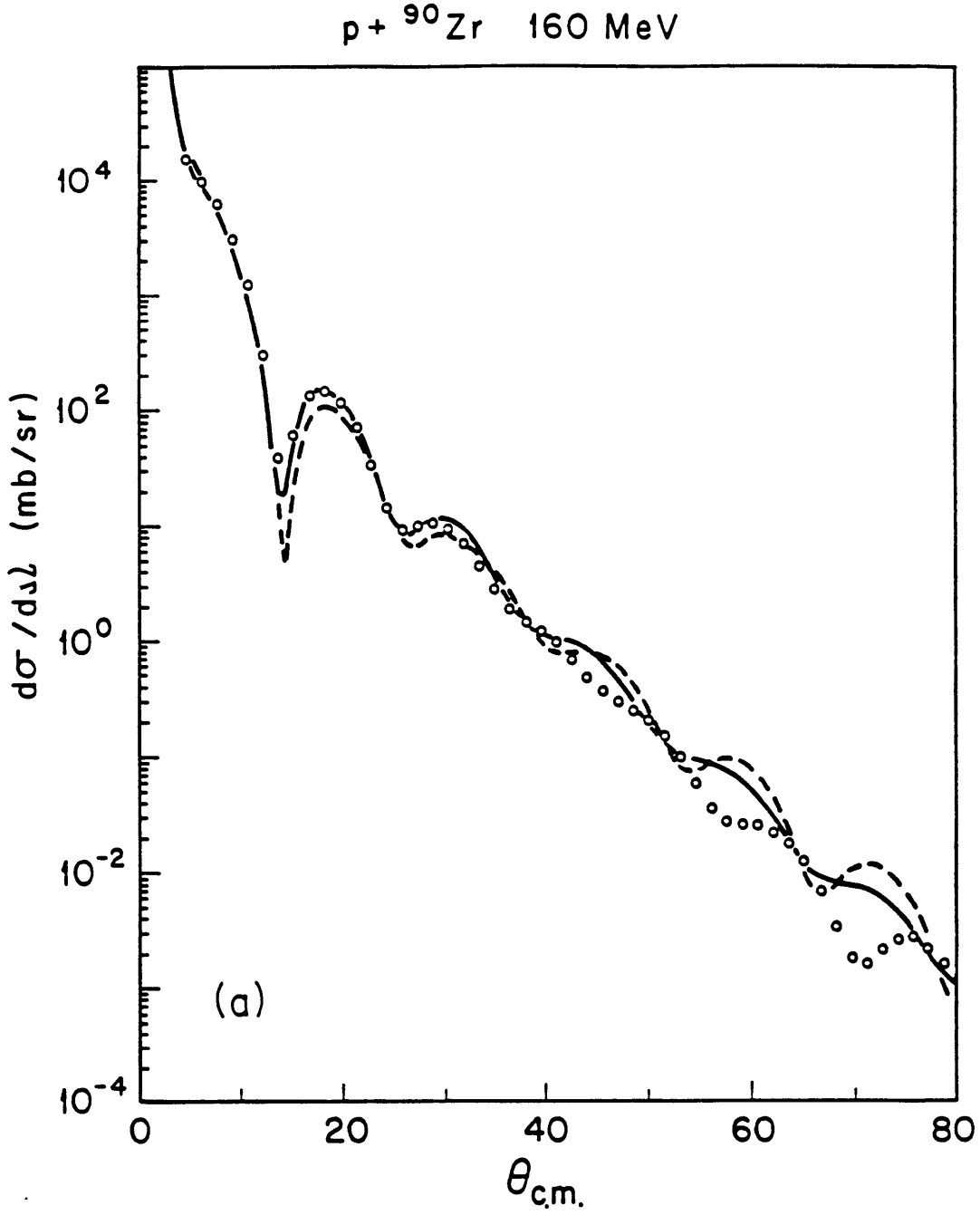

(a)

Fig. 2.9 Cross section (a), analyzing power (b) and spin rotation parameter (c) for 160 MeV ^{90}Zr scattering. The dashed curves use pseudovector coupling but omit the Pauli blocking correction. Data are from Ref. [Sc82].

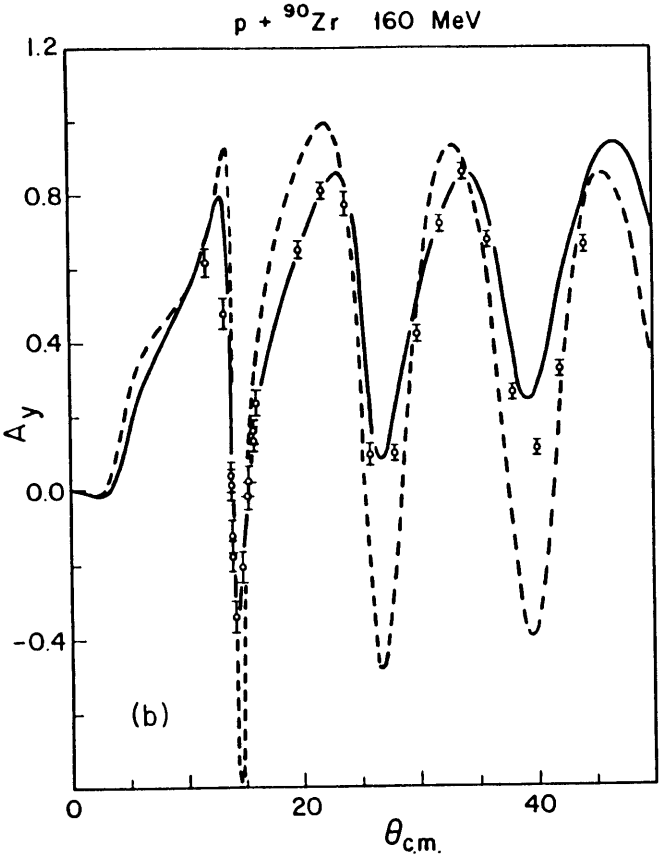
p + 90Zr 160 MeV
1.2
0.8
0.4
0.0
-0.4
Ay
(b)
0
20
40
θc.m.

(b)

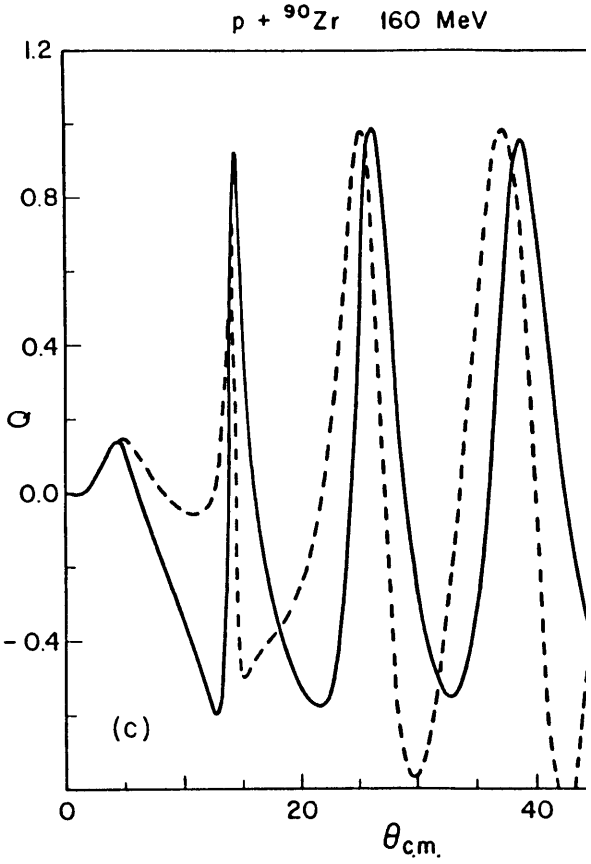
p + 90Zr 160 MeV
1.2
0.8
0.4
0.0
-0.4
Q
(c)
0
20
40
θc.m.

(c)

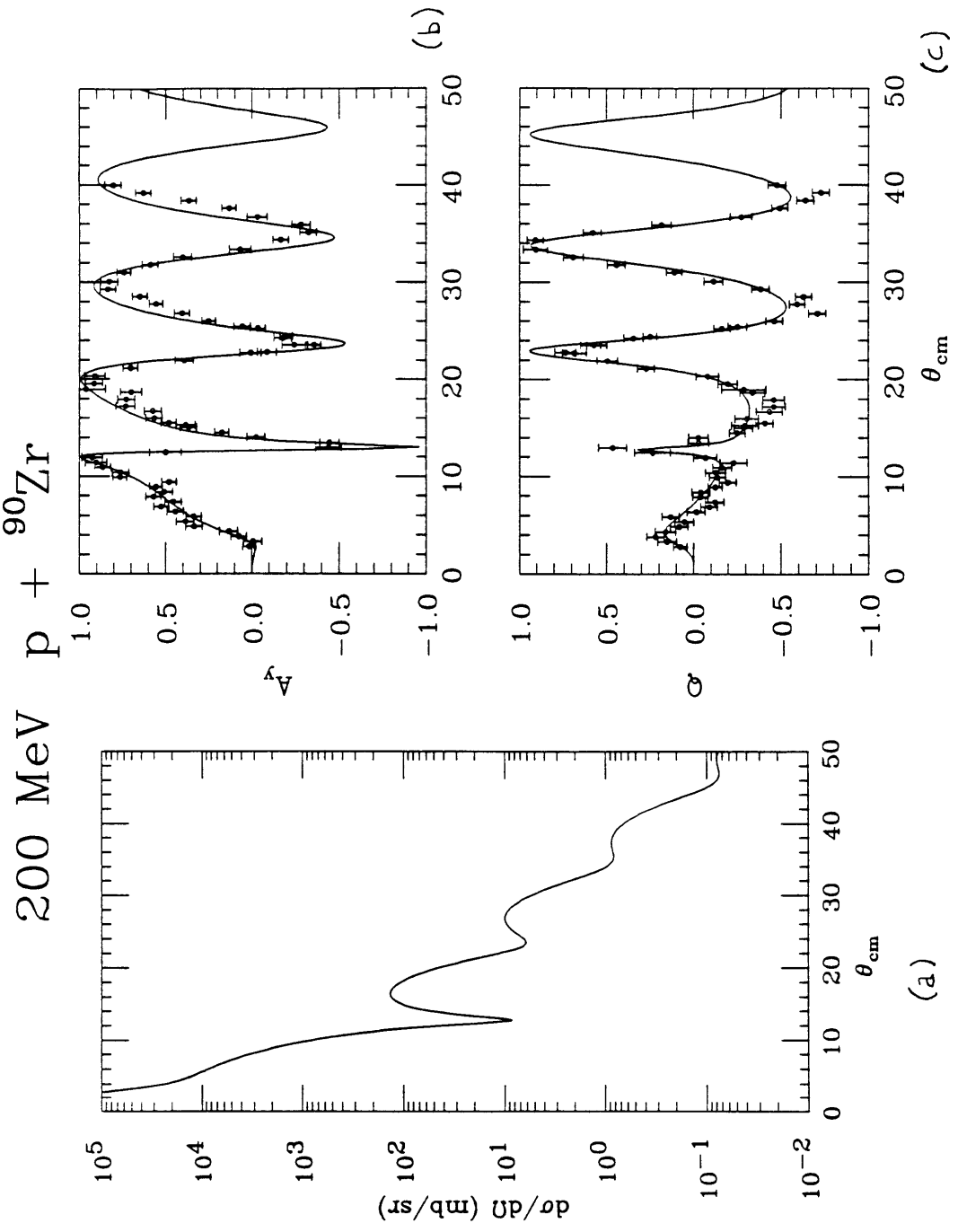

Fig. 2.10 Cross section (a), analyzing power (b) and spin rotation parameter (c) for 200 MeV ^{90}Zr scattering. Preliminary TRIUMF data are from [Hi87]

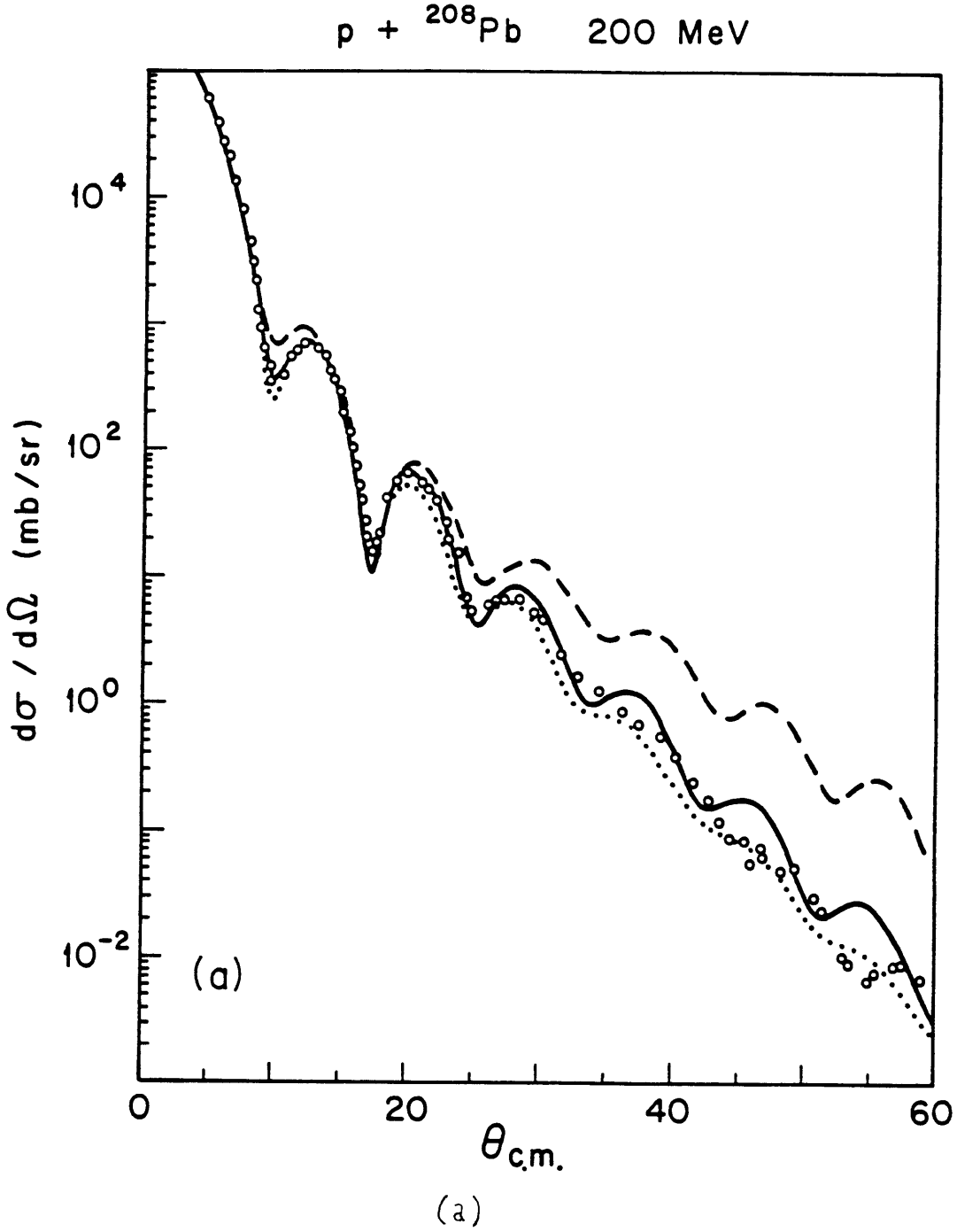

Fig. 2.11a Cross section for 200 MeV ^{208}Pb scattering. The dashed curve is the original RIA calculation. The dotted curve differs from the solid curve in that empirical densities, described in Section III.C. are used. Data are from Ref. [Hu81a].

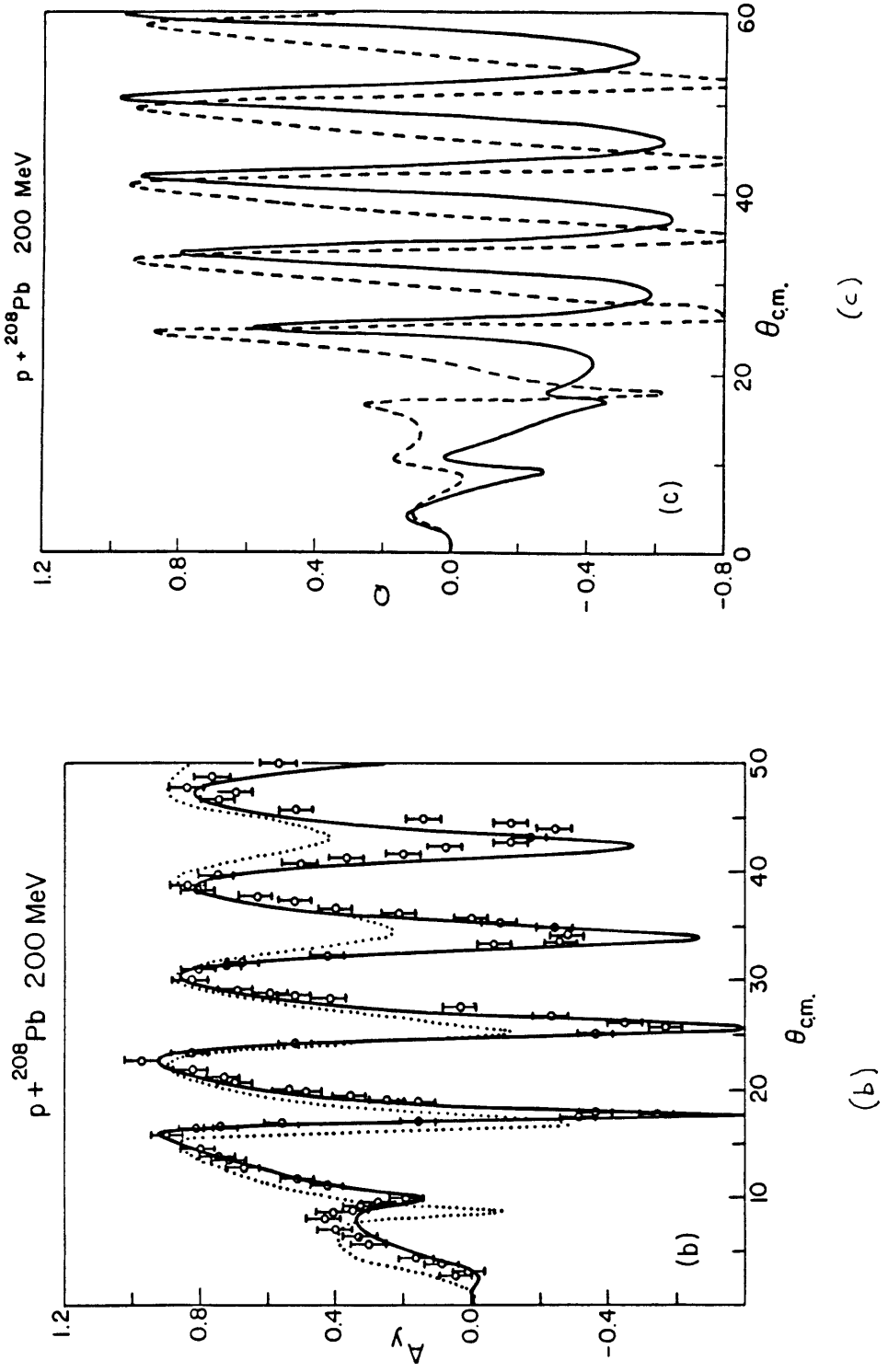

Fig. 2.11b–c (b)Analyzing power for 200 MeV ^{208}Pb scattering. The dotted curve is the nonrelativistic calculation of Ref. [Ri85]. Data are from Ref. [Hu81a]. (c) Spin rotation parameter for 200 MeV ^{208}Pb scattering. The dashed curve omits the Pauli blocking correction.

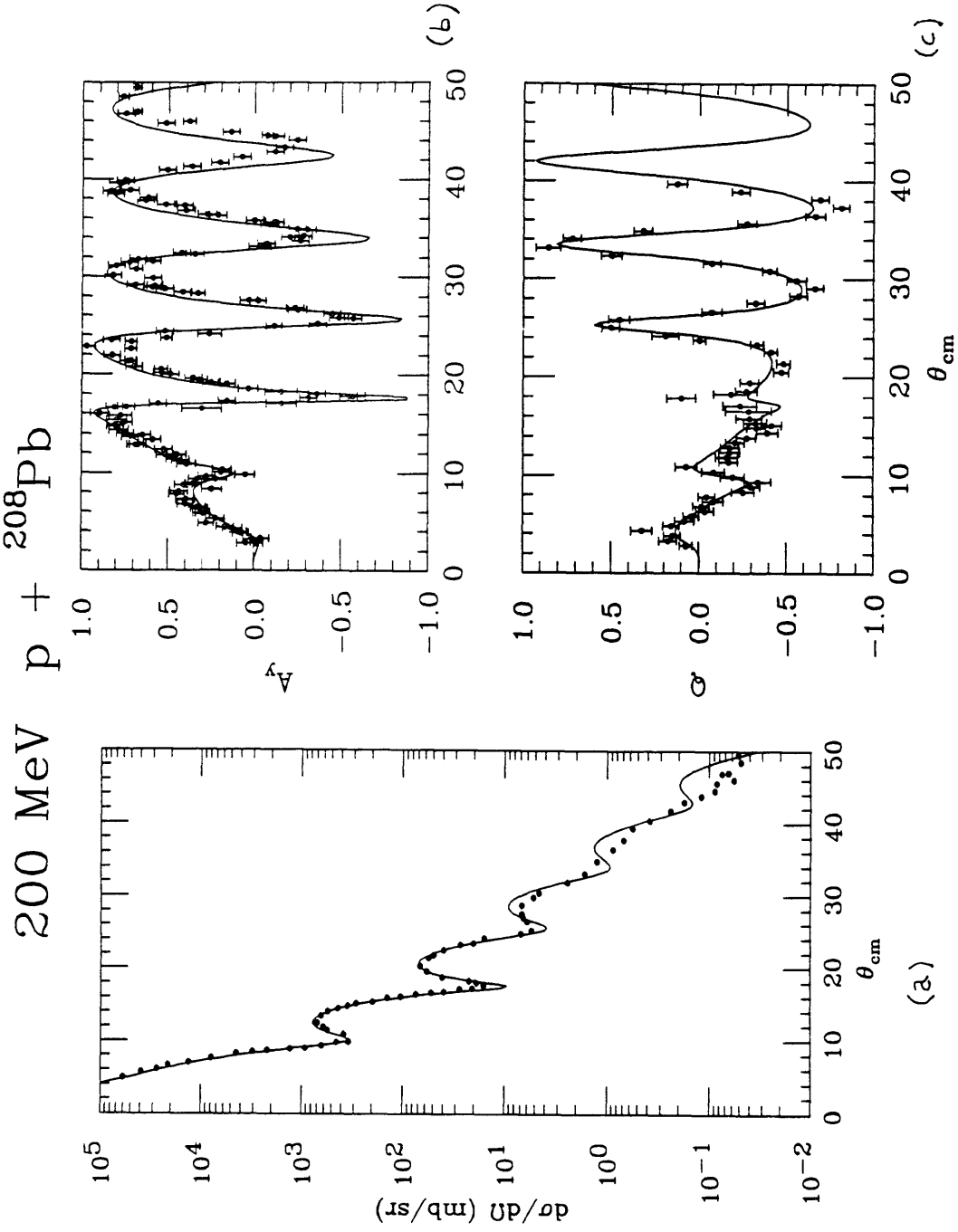

Fig. 2.12 Cross section (a), analyzing power (b) and spin rotation parameter (c) for 200 MeV ^{208}Pb scattering. Preliminary TRIUMF data are from [Hi87]

Calculations for 300 MeV and 400 MeV are just as successful; some of these will be shown in part 2.H.4.

2.H.3 Sensitivities of the 200 MeV Calculations

We now look at at the importance of various features of the model in producing the good agreement with the data.

The most important single feature is the explicit treatment of nucleon exchange. In Figs. 2.11a and 2.15 we compare the full calculation for 200 MeV ^{208}Pb scattering (solid curve) with the original RIA using the MRW parametrization of F^S and F^V (dashed curve). (For the latter calculation, we have used new parameters for the pn invariants since there is an apparent misprint in the tables of Ref. [McN83a].) The RIA is good only until about 30°, beyond which the cross section is too large and the analyzing power is far too negative. Our treatment of exchange brings both observables close to the data over a much larger range of scattering angles.

An explicit treatment of exchange is important because of the odd behavior of the MRW amplitudes under interchange of the two nucleons. In Fig. 2.13 we show the Lorentz scalar invariant F^S_{pp} at $T_{\rm lab} = 200$ MeV as a function of the NN center of mass scattering angle. Due to exchange contributions, F^S rises dramatically at large angles. Note that 60° scattering off of a heavy nucleus corresponds to 180° in the NN frame, so the amplitudes are needed at large angles.

The original RIA only fit the NN amplitudes up to *60 degrees in the NN frame* ([McN83a], [Sh83]). One such fit is shown in Fig. 2.13. However, for scattering from a heavy nucleus at nucleon-nucleus angles beyond $\approx$ 30°, the NN amplitudes are needed at much larger NN angles. Indeed, the MRW curve in Fig. 2.13 is very sensitive to the fit to the forward NN amplitude.

Thus the simple RIA with the original parametrization of the NN amplitudes is essentially calculating *random noise* for large nucleon-nucleus scattering angles. I.e.

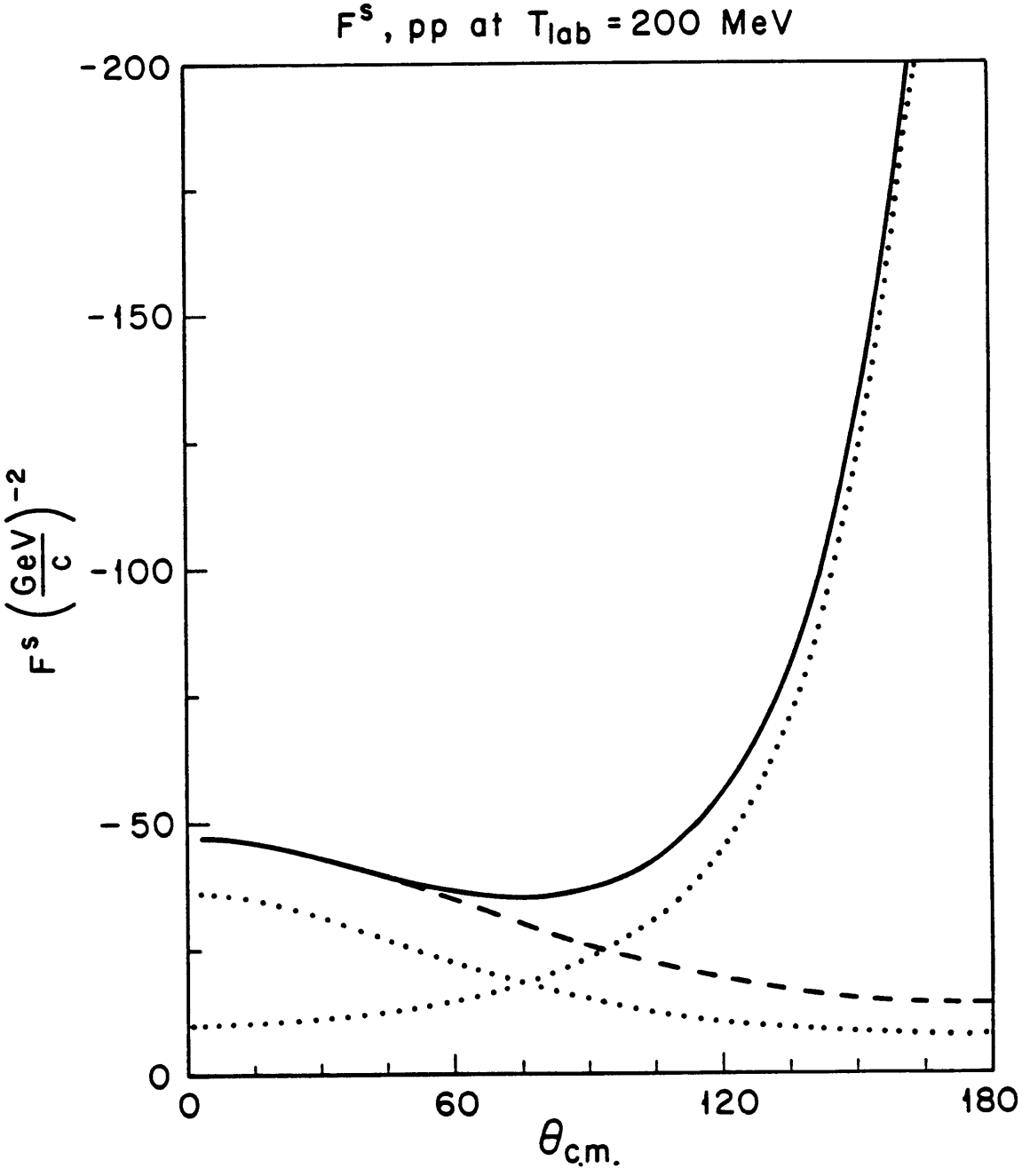

Fig. 2.13 Imaginary part of the invariant F^S for pp scattering at 200 MeV. The solid curve shows the values from the Arndt phase shifts [Ar82]. The dashed curve is the MRW fit [McN83a], extrapolated to large q. The F^S of our model is the sum of direct and exchange pieces which are respectively the decreasing and increasing dotted curves.

the RIA results for scattering beyond 60° depend solely on gross extrapolations of fits to the far forward NN amplitudes. Therefore, the conclusions in Ref. [Dr85] about large angles are incorrect.

Note, the RIA calculations in Refs.[Ra85] and [Cl83b] (but not those in Refs. [McN83b], [Sh83] or [Dr85]) use the Breit frame prescription for the NN amplitudes. Here, NN amplitudes at the experimental $T_{\rm lab}$ and a large scattering angle are replaced by NN amplitudes at a higher effective $T_{\rm lab}$ and a smaller scattering angle (which gives the same momentum transfer). This somewhat alleviates the problem but at the cost of introducing unphysical reactive content into the NN amplitudes. For example, 200 MeV NN amplitudes can be replaced with up to 800 MeV amplitudes, which include unphysical pion production.

After the identification and local treatment of the exchange amplitude, we make a choice on the type of "pion" coupling used and include a rough treatment of Pauli blocking. Figs. 2.7a–c show the cross section, A_y, and Q for ^{40}Ca at 200 MeV. The dashed curves differ from the calculation for the solid curves in that pseudoscalar coupling is used. The resulting cross section is too large. The dotted curves omit the Pauli blocking correction (but use a pseudovector pion) for which the cross section is too large and has too much structure. Furthermore, the spin observables disagree with the data at small angles.

Other comparisons of calculations with and without Pauli blocking (for ^{90}Zr and ^{208}Pb) are shown in Figs. 2.9, 2.11c, 2.17 and 2.18.

The small tensor potential was not included in the primary calculations for Figs. 2.5 through 2.12. Its small effect on the observables at 500 MeV has been demonstrated by Clark et al [Cl83c]. It has a similar small effect at lower energies. Figs. 2.8a–c show $\frac{d\sigma}{d\Omega}$, A_y and Q calculations for ^{48}Ca at 200 MeV. The solid curves use the same conventions as in the other figures while the dotted curves include the tensor potential (with a pseudovector pion coupling and no Pauli blocking factor for U^T). There is only

a small change in Q at forward angles. The tensor potentials for ^{48}Ca are about twice as big as for ^{40}Ca because of the $f_{\frac{7}{2}}$ neutrons. Therefore, the effect of the tensor potential in ^{16}O and ^{40}Ca is even smaller than for ^{48}Ca.

Finally, there are sensitivities to the nuclear structure input. These must be taken into account before detailed comparisons are made with other models and the data at large scattering angles. We give examples of this uncertainty for 200 MeV ^{12}C and ^{208}Pb scattering. For ^{12}C we form an alternative baryon density by unfolding the proton charge form factor from the experimental carbon charge density. For ^{208}Pb we use the Gauss III parameters of Ref. [Ri85] for the proton and neuton densities. Then we use a nuclear matter approximation to obtain the ratio of baryon to scalar densities. Our prescription, based on the relativistic mean field theory of Ref. [Se86] is to approximate $\rho_S = \left\langle \sqrt{1-\frac{v^2}{c^2}} \right\rangle \rho_B$ by

$$\rho_S(r) = \rho_B(r)\left(1 - \frac{3}{10}\frac{k_F^2}{M^{*2}}\right). \qquad (2.H.4)$$

with k_F being the local Fermi momentum $k_F^3 = \frac{3\pi^2}{2}\rho_B$. Since at the saturation baryon density of .1934 fm^{-3}, the effective mass is $M^* = .56M$, we use a linear interpolation,

$$\frac{M^*}{M} \approx 1 - .44\frac{\rho_B}{.1934\ fm^{-3}}\ . \qquad (2.H.5)$$

When the densities are calculated in this way for ^{12}C, proton and neutron densities are taken to be equal. Hartree densities for ^{12}C and ^{208}Pb are compared with these alternate densities in Fig. 2.14.

The differences in the resulting cross sections and analyzing powers for the choices of nuclear input are significant. For ^{12}C, the observables found from using the empirical density are shown in Figs. 2.5a–2.5c by the dashed curves. Beyond 60° the phases of spin observables are very different.

For Pb, cross sections computed from the two sets of densities are likewise compared in Fig. 2.10a. The Hartree values are larger and have more structure at larger

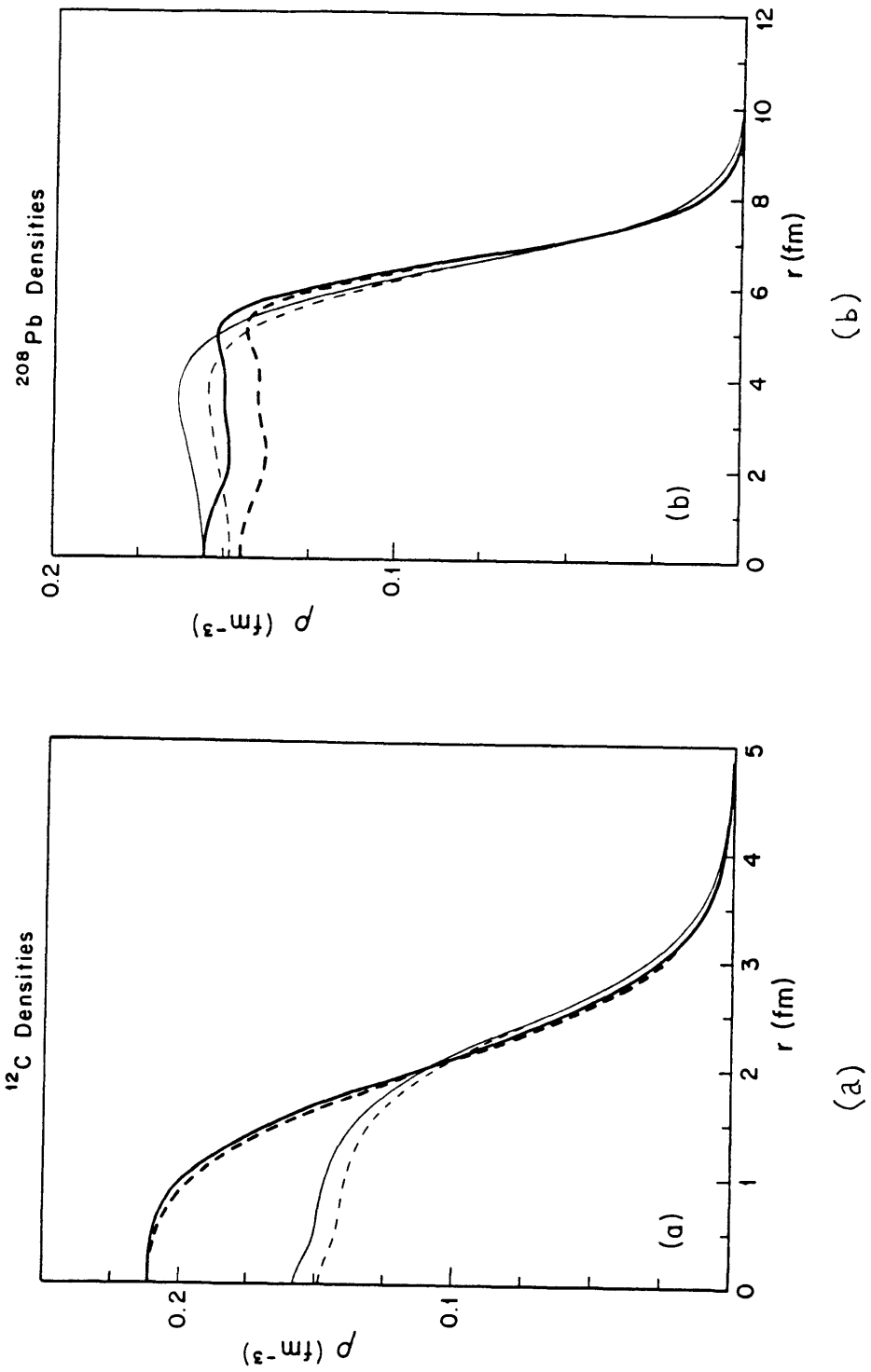

Fig. 2.14 Comparison of baryon and scalar densities for ^{12}C (a) and ^{208}Pb (b), from Hartree calculations and empirical sources described in the text. Solid curves are baryon densities and dashed curves are scalar densities. Heavy curves are from the Hartree calculation of Ref. [Ho81]; thin curves are from empirical sources.

angles. Analyzing powers are compared in Fig. 2.15. Again, the two sets of densities give similar results at small angles, but beyond 50° there is much more structure in the Hartree curve. Clearly, any comparison of relativistic model predictions for large–angle spin observables must take into account the fine details of the target structure. In addition, vacuum fluctuations may significantly reduce ρ_S relative to ρ_B; see Ref. [Ho84].

2.H.4 300 MeV and 400 MeV Observables

The calculations for scattering at 300 MeV and 400 MeV are just as successful. Calculations for ^{16}O and ^{208}Pb for energies near 300 and 400 MeV are shown in Figs. 2.16, 2.17 and 2.18. The solid theoretical curves use the same model choices as for the 200 MeV calculations. (See Appendix A for the parameters used for the 300 MeV NN amplitudes.)

In the large nuclei ^{90}Zr and ^{208}Pb at 200 MeV and 300 MeV, Pauli blocking substantially changes Q (see Figs. 2.9c, 2.11c, and 2.15c) at forward angles. However, the only published experimental data on the spin rotation parameter Q for either nucleus are for ^{208}Pb at 290 MeV [Ha85]. They agree very well with the Pauli blocked calculation.

Even though the Pauli blocking effect for A_y is smaller at higher energies, its inclusion in our calculation gives a very noticeable change in A_y at forward angles, as shown in Fig. 2.17b, for 300 MeV and Fig. 2.18 for 400 MeV. The A_y values are moved up from the unblocked values to give agreement with experiment.

2.I Other Microscopic Calculations for 200 MeV

In this section we note some other work on microscopic calculations of optical potentials applicable to 200 MeV elastic scattering.

Tjon and Wallace [Wa85] have performed a complete calculation of the invariant amplitude $\hat{\mathcal{F}}$ [Tj85]. Within their model for the NN interaction, there is no further

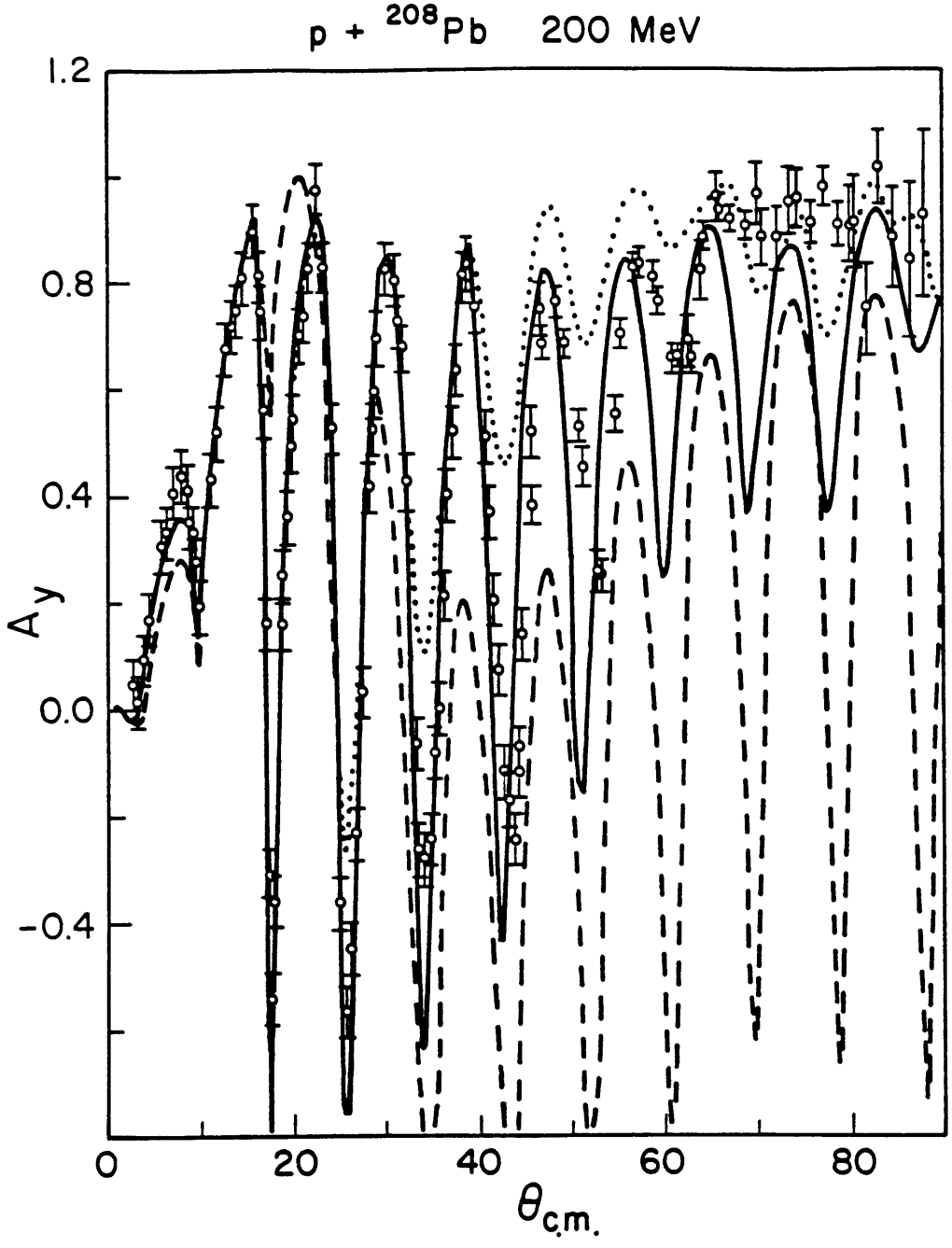

Fig. 2.15 Large–angle analyzing power for 200 MeV ^{208}Pb scattering. The dashed curve is the original RIA calculation. The dotted curve differs from the solid curve in that empirical densities for ^{208}Pb were used. Data are from Ref. [Dr85].

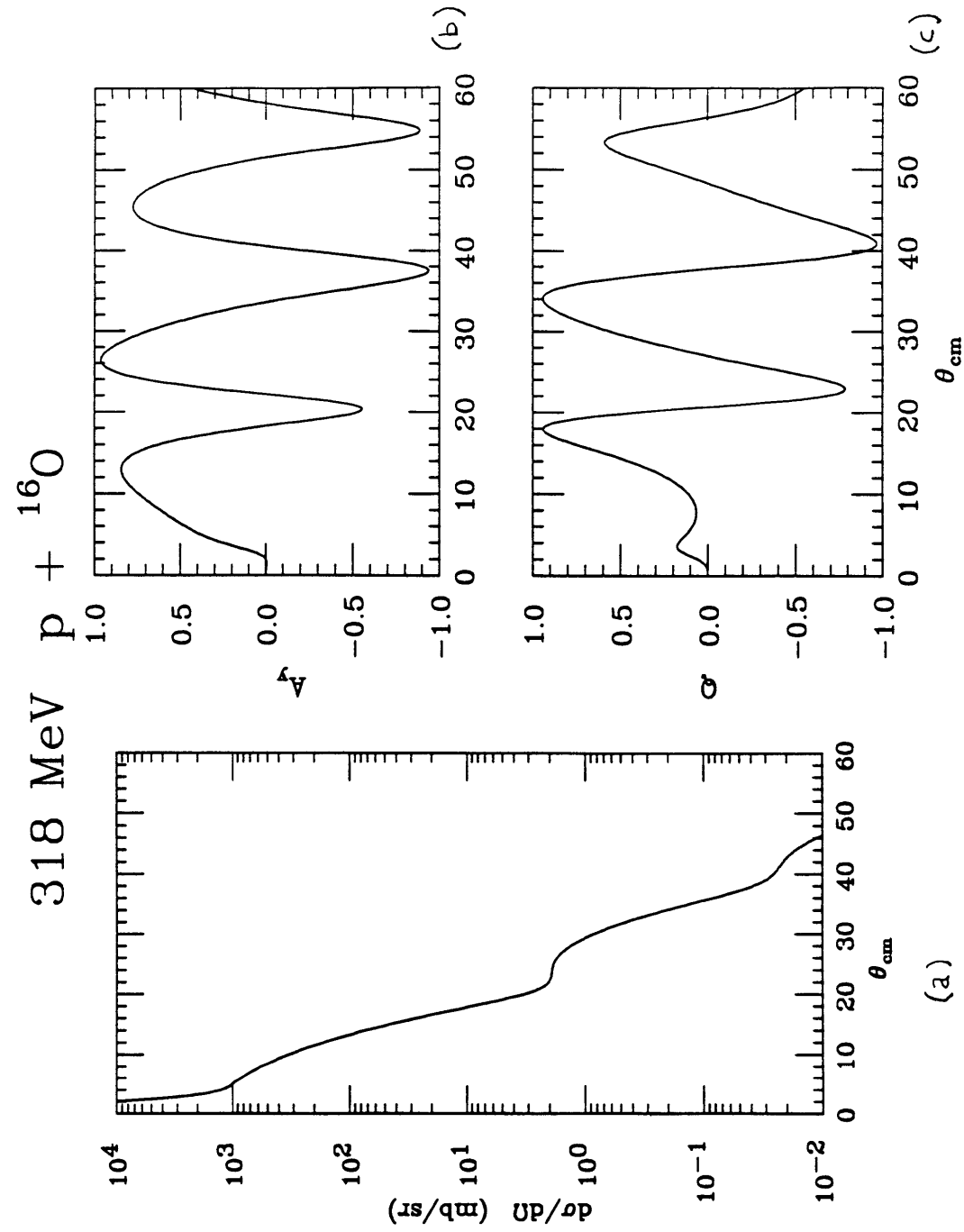

Fig. 2.16 Cross section (a), analyzing power (b) and spin rotation parameter (c) for 318 MeV ^{16}O scattering.

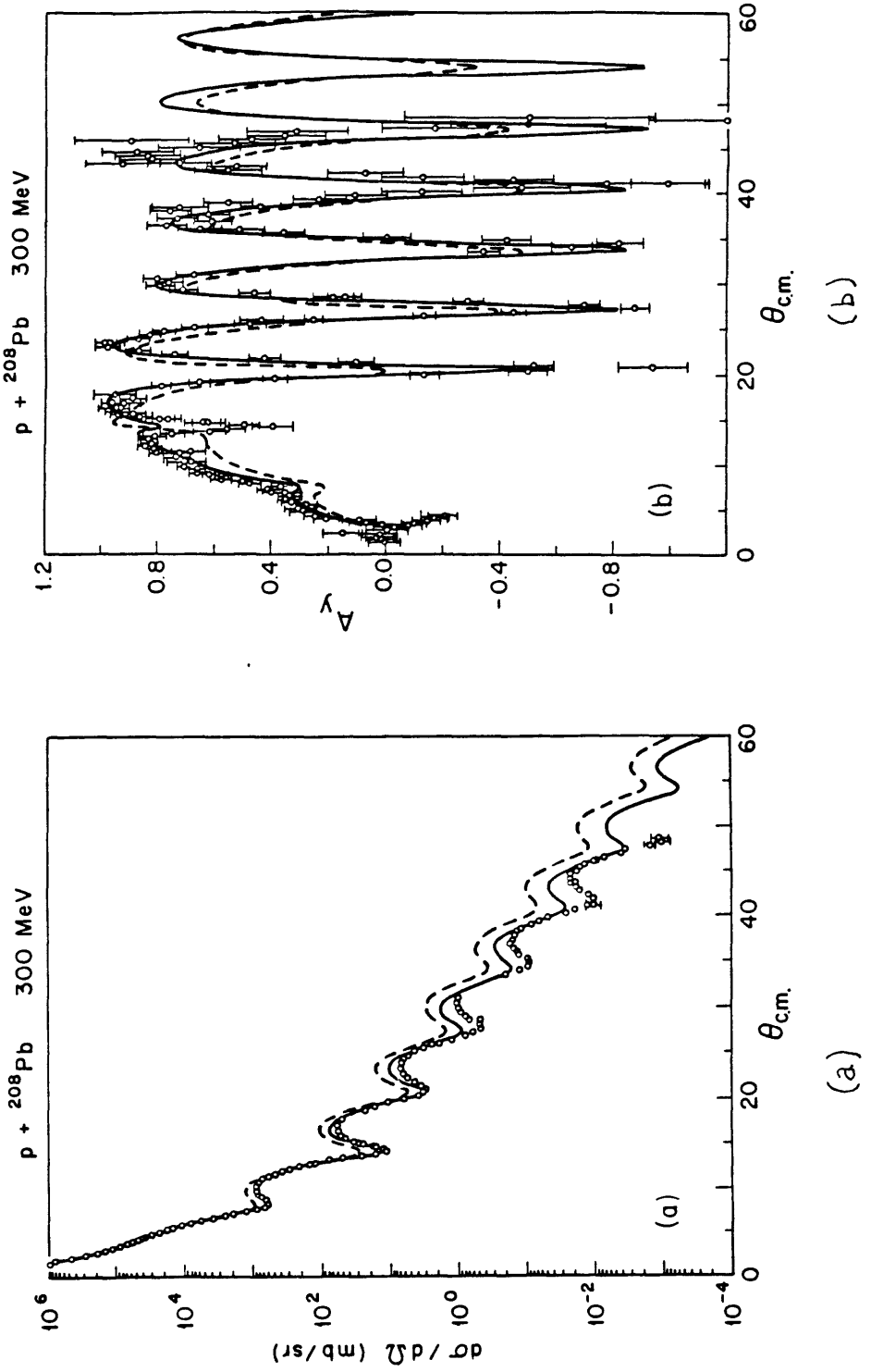

Fig. 2.17 Cross section (a), analyzing power (b) and spin rotation parameter (c) for 300 and 290 MeV ^{208}Pb scattering. The dashed curves in 15a and 15b omit the Pauli blocking correction. The dashed curve in 15c is a non-relativistic calculation of Bauhoff et al [Ba85]. The TRIUMF Data are from [Ha85].

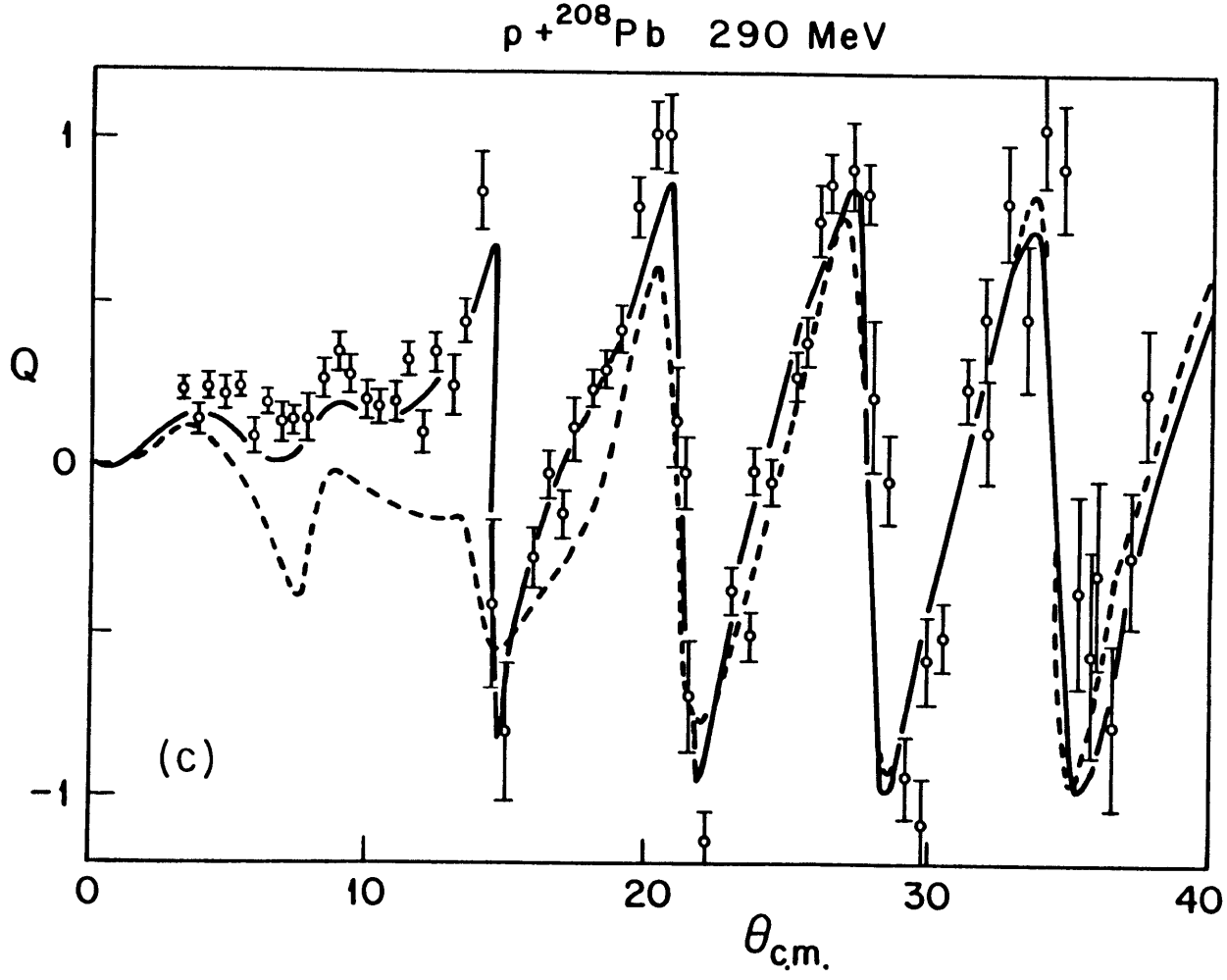

(c)

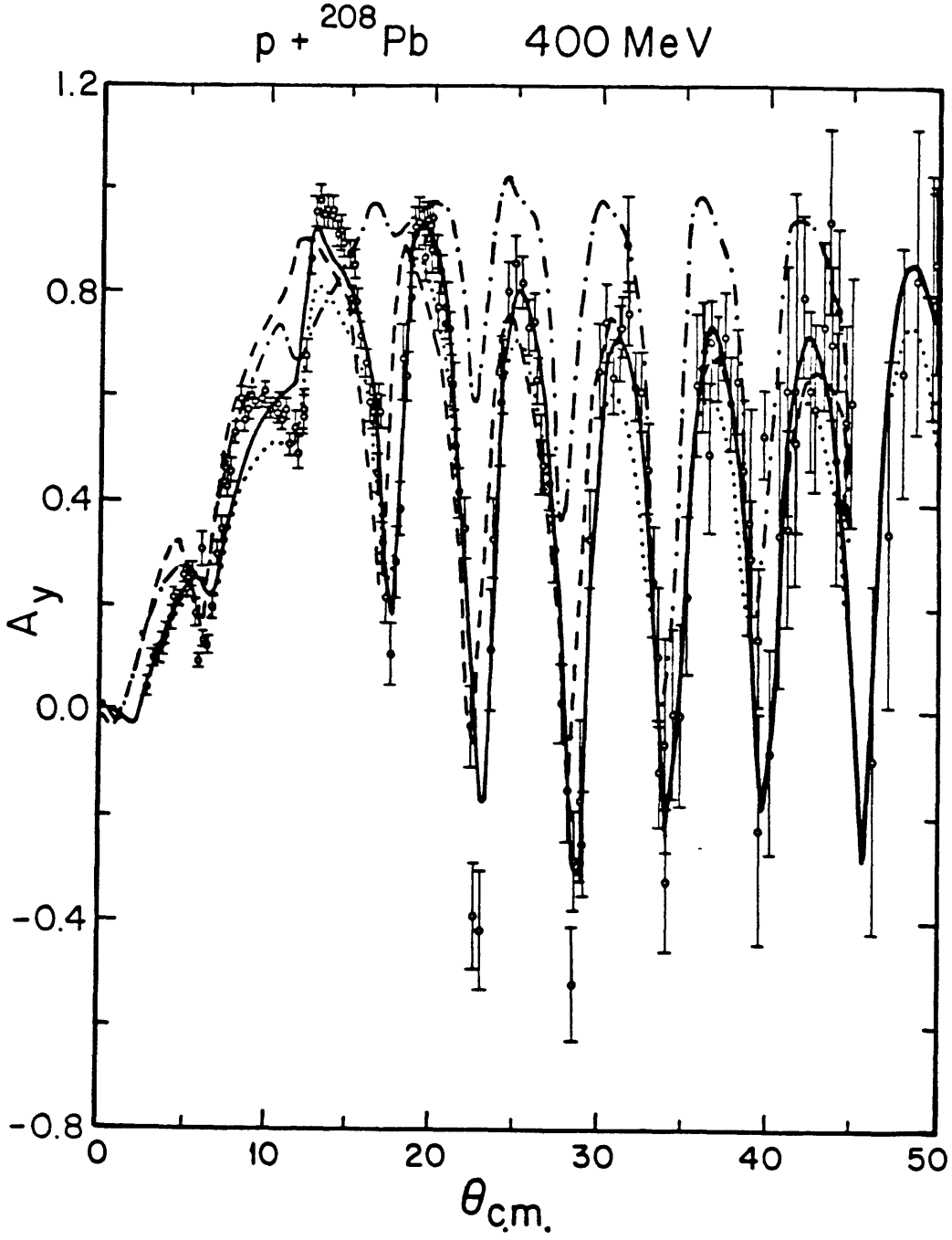

Fig. 2.18 Analyzing power for 400 MeV ^{208}Pb scattering. The solid curve includes Pauli blocking while the dotted curve does not. The nonrelativistic calculation with medium modifications [Ri85] is dashed, while the dot–dashed curve is the nonrelativistic KMT impulse result of Ref. [Ra85]. The TRIUMF Data are from Ref. [Hu81b].

ambiguity in the form of $\hat{\mathcal{F}}$. The $\hat{\mathcal{F}}$ matrix elements were calculated using NN data for the positive energy free spinor matrix elements and a meson model for the rest. Pseudovector coupling is used for the pion to insure that the pion–exchange contribution to the optical potential is well-behaved. However, Ref. [Wa85] presents results for the potentials and scattering observables without any correction for Pauli blocking as in our Eq. (2.G.1). An important additional difference with our work is that they do not make the separation into direct and exchange invariants, and so they do not use the particular kinematics which are built into the $t\rho$ folding for each part, described in Section 2.D.

The spin observables for ^{40}Ca which they calculate agree with the data about as well as our results, while the cross sections are too large beyond $\approx 30°$, probably due to the omission of Pauli blocking and an explicit treatment of exchange. It would be interesting to see their calculations for ^{208}Pb where we find large Pauli blocking effects.

The nonrelativistic calculation of Rikus and von Geramb [Ri85] used an effective interaction (nonrelativistic, with central and spin–orbit pieces) generated from a Brueckner calculation using the Paris potential. Pauli blocking is thus built into the interaction from the beginning. Also, since they begin with a model t–matrix, they make the separation into direct and exchange parts and then do the folding with the nonrelativistic densities as we do in Eq. (2.F.1). The agreement with the Pb data for cross sections and polarizations is good except for the small angle values of the polarization, where nonrelativistic calculations typically miss the second minimum. However, for Q, there are larger differences. In Fig. 17c we show the calculation of Bauhoff [Ba85] for ^{208}Pb at 290 MeV. Here, the nonrelativistic calculation has the wrong sign for Q at forward angles ($\leq 15°$).

Nonrelativistic impulse approximation calculations [Ra85] give poor spin observables near 200 MeV. Although the medium–modified nonrelativistic calculations do much better in certain cases (for example, ^{40}Ca [Ba84]), there are no published nonrelativistic results which systematically reproduce all the spin observables shown here.

We do not claim our good relativistic description is unique. Some nonrelativistic calculations have also reproduced selective spin observables. It would be useful to have a systematic series of nonrelativistic calculations of all 200 MeV spin observables.

These relativistic calculations have smaller Pauli blocking corrections than in nonrelativistic works. It is an important open question to further understand the role of relativity and/or medium modifications in giving good agreement with data.

Thies [Th85] has claimed that the *non*relativistic propagator is badly behaved at short distances. Thus, he postulates that if short–ranged correlations are included, the final results will be less sensitive to this short–distance problem. However, Cooper and Jennings [Co86] have estimated a short distance correlation parameter and find its effects to be much too small. Furthermore, the medium modifications in Ref. [Ri85] may be quite different from Thies's correlations. Thus, there are many open questions in comparing relativity and/or medium modifications.

Section 2.J Conclusions

We have presented a new formalism for calculating relativistic optical potentials for elastic proton scattering from closed shell nuclei. This formalism contains important physics not in the original relativistic impulse approximation.

First, exchange terms are explicitly included in the optical potential. This allows one to deal with the dramatic increase of the relativistic NN amplitudes at large scattering angles. A proper treatment of exchange is crucial for describing large angle analyzing power and cross section data.

Next, ambiguities in the relativistic form of the NN amplitude are resolved by using a pseudovector coupling for the pion. This reduces both the strength and energy dependence of the real scalar and vector optical potentials.

Finally, medium modifications from Pauli blocking are incorporated using relativistic Brueckner results for nuclear matter in a local density approximation. Pauli blocking reduces the imaginary optical potential.

Calculations for ^{12}C, ^{16}O, ^{40}Ca, ^{48}Ca, ^{90}Zr and ^{208}Pb at $T_{\rm lab}$=200 MeV including these three corrections *quantitatively* reproduce all measured elastic spin observables. Both the analyzing power and spin rotation function are reproduced out to about 60 degrees. If Pauli blocking is omitted or if pseudoscalar pion coupling is used, the spin observables are significantly worse. In particular, Q for ^{208}Pb at 290 MeV changes dramatically if Pauli blocking is omitted.

The energy dependence of these corrections has been examined with calculations at $T_{\rm lab}$ = 300 and 400 MeV. As $T_{\rm lab}$ increases, the importance of Pauli blocking diminishes. At 400 MeV in ^{208}Pb, Pauli blocking has a much smaller effect on A_y than do medium modifications in nonrelativistic calculations.

Also, the difference between pseudoscalar and pseudovector amplitudes is not important at $T_{\rm lab}$ = 400 MeV. Furthermore, current experimental data does not extend to large enough angles for an explicit treatment of exchange to be crucial. Therefore, these calculations essentially agree with the original RIA at $T_{\rm lab}$= 500 MeV and above.

Much theoretical work needs to be done to get a formalism which is satisfactory at still lower energies and for larger scattering angles. This will require more detailed calculations of Pauli blocking, the resolution of other ambiguities in the NN amplitudes and more constraints on the target densities.

ACKNOWLEDGEMENTS

T. Drake, O. Hausser and E. Stephenson are thanked for providing preliminary experimental data.

Chapter 3. Quasi–Elastic Proton Scattering

3.A Introduction

3.A.1 Quasi-elastic Proton Scattering

When we study the inelastic scattering of protons by nuclei and look at energy losses ω beyond those for excitation to discrete states, the cross section shows a broad peak at around $\omega = \frac{q^2}{2M}$ where q is the momentum transfer. This energy loss is close to that for free NN scatttering, and the momentum width of the peak is related to the Fermi momentum of nuclear matter; the scattering mechanism must be similar to free NN scattering, and this peak is termed the quasi-free or quasi-elastic peak. It is now quite feasible to measure the complete set of observables for inclusive (p,p) and (p,n) reactions at intermediate energies. These observables involve the spin orientations of the incoming and outgoing (fast) nucleon.

The quasielastic process may provide some very clear tests to see if the influence of the nuclear medium on NN scattering shows some signature of relativistic dynamics. In contrast to the study of excitations to discrete states, we probably would not need to know the wavefunctions for excited states. Simple models for the target may suffice; in fact, Fermi gas models for the target seem to work well for quasielastic electron scattering [Ro80].

It can also test the parts of the relativistic NN interaction not seen in elastic scattering, where at lab energies $\geq$ 400 MeV, only the scalar and vector NN amplitudes

are important. Without the constraint of the same final and initial states, all Lorentz terms will contribute; we can study the quasielastic charge exchange reaction (inclusive (p,n)) for which the pion, via the pseudoscalar invariant, is expected to play the major role. Furthermore, quasi-free knockout will test the part of the impulse approximation which leads to nuclear reactions, also untested in the elastic studies.

However, protons are strongly absorbed in the nuclear medium and the scattering wavefunction is strongly diminished and distorted. Calculations of the cross section are very sensitive to the way these distortions are treated and this uncertainty is expected to be at least as large as the effect of the enhanced lower components. So comparison of theory with cross section data is not likely to reveal a clear signature of relativistic dynamics.

However, there may be much more to learn from the spin observables of quasielastic scattering, which are defined similarly to those of elastic scattering. If the distortions have a dependence on spin orientation which is small (or calculable) and the larger distortion from the central potentials comes as normalization corrections to the impulse approximation cross section, then the situation is much better for the spin observables. The uncertainty in normalization of cross sections cancels out to allow comparisons of other features of the calculation.

Nonrelativistic calculations of spin observables ([Sm85], for example) do not predict values differing very much from the free NN values. But recent measurements of the polarization P in a 500 MeV Los Alamos experiment [Ca85] gives a value significantly below the free value. This change is likely due to an NN interaction differing from the free one, or possibly collective excitation of the target. The high energy transfers of these experiments, of order $\geq$60 MeV, would seem to make collective excitations unlikely. The focus here will be on the changes to the NN interaction in the nuclear medium, as resulting from a relativistic treatment.

In a previous work [Ho86], relativistic effects were calculated for the spin observables at the quasielastic peak. This corresponds to the target nucleons being at rest.

In this work, a full relativistic plane wave impulse calculation is performed for a particular model of the target in order to map out the full dependence on energy loss. The full response will give an indication of the effect of Fermi motion of the target nucleons and will indicate the importance of the various simplifications chosen for the target.

Another new feature of this work is the use of different spinors for projectile and target plane waves. This will permit the separate examination of the relativistic effects on the projectile and target in giving differences from the nonrelativistic calculation.

3.A.2 Observables; Notation

In this work, double–differential cross sections will be calculated per *energy* bin; these are related to cross sections per momentum bin by:

$$\frac{d^3\sigma}{d\Omega_1 dE_1'} = \frac{dk_1}{dE_1'}\frac{d^3\sigma}{d\Omega_1 dk_1} = \frac{E_1'}{k_1}\frac{d^3\sigma}{d\Omega_1 dk_1} \tag{3.A.1}$$

where E_1' is the final total energy and k_1 the magnitude of the final 3–momentum of the proton.

The notation for the initial and final momenta and possible spin orientation directions of the scattered proton are shown in Fig. 3.1. The analyzing power A_y and the spin–transfer coefficients $D_{i'j}$ are defined in Eqs. (3.B.31) and (3.B.32). The meaning of A_y here is similar to its definition in the elastic case (Fig. B.2); $D_{i'j}$ measures the likelihood of a proton beginning with spin aligned along $\hat{j}$ to scatter to a state with spin aligned along $\hat{i}'$.

3.B Formalism for RPWIA

3.B.1 Fermi Gas Model

The model for quasielastic scattering process is that of scattering from a relativistic Fermi gas whose parameters are chosen in accordance with the particular proton

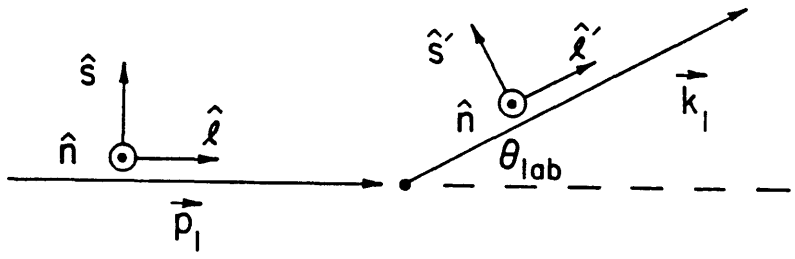

Fig. 3.1 Definition of the spin polarization directions $\hat{n}$, $\hat{s}$, $\hat{l}$, $\hat{s}'$ and $\hat{l}'$; see Eq. (3.B.32).

scattering process. The physical justification for this simple model is in the large energies considered, 400–800 MeV, for which surface effects in the finite nucleus will probably not be important. The model will give a cross section *per nucleon*; we will then figure in an effective number of nucleons to get the experimental cross section.

The quasielastic scattering process in this model is diagrammed in Fig. 3.2. The scattering takes place in the medium, where the mean scalar fields are $\overline{S}$ and $\overline{V}$; the scalar field gives rise to relativistic effective masses for the interacting nucleons. The mean vector field $\overline{V}$ simply shifts the energies of all particles by a fixed amount and will not affect the scattering calculation. The momentum states are occupied up to k_F for both protons and neutrons.

The choices for $\overline{S}$ and k_F are given in the next section.

3.B.2 Parameters of the Fermi Gas Model

$\overline{S}$ and k_F will be chosen to be averages over the volume of the finite nucleus for p–A scattering at a specific lab energy. To do this averaging, we use the transmission

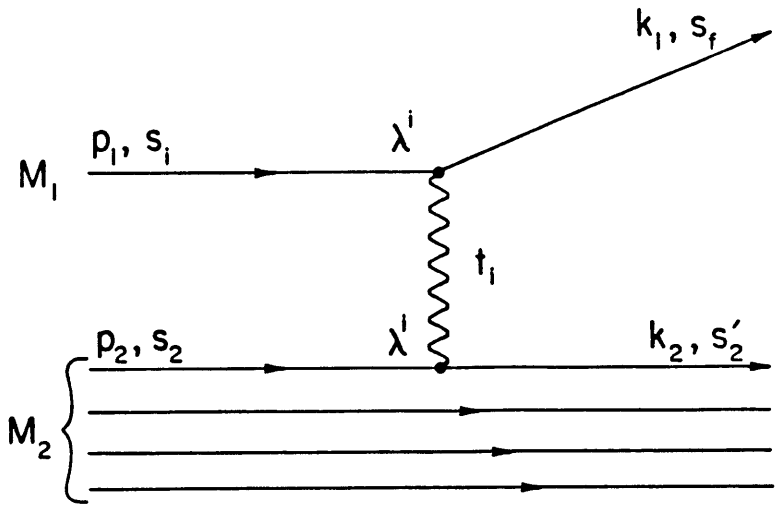

Fig 3.2 Schematic diagram of the impulse approximation for quasielastic proton scattering. The index i is summed over the five invariant amplitudes in Table 1.2.

probability for a proton of lab energy E to pass through the nucleus at an impact parameter b, $T(b,E)$. In the eikonal approximation, [Am83] this is:

$$T(b,E) = \exp\left\{\frac{4M}{k}\int_0^\infty dz\,\mathrm{Im}\,V_c(b,z)\right\} \qquad (3.B.1)$$

where

$$V_c = S + \frac{E}{M}V + \frac{1}{2M}(S^2 - V^2) \qquad (3.B.2)$$

and where we have dropped the spin-orbit and Darwin terms. Then, with $T(b)\rho(b,z)$ as the weighting factor for p–A collisions, we calculate an average density:

$$\langle\rho\rangle = \frac{\int bdb\,T(b)\int dz\rho(b,z)^2}{\int bdb\,T(b)\int dz\rho(b,z)} \qquad (3.B.3)$$

then we use

$$k_F = \left(\frac{3}{2}\pi^2\langle\rho\rangle\right)^{\frac{1}{3}} \qquad (3.B.4)$$

in the Fermi gas model.

We compute two values of the "average scalar field". The first comes from using relativistic optical potential fits to elastic scattering [Ko85]. Assuming that the scalar potential is roughly proportional to the baryon density,

$$S(r,E) \approx S_0(E)\frac{\rho(r)}{\rho_0} \tag{3.B.5}$$

where S_0 is the value at the origin of the scalar real optical potential, we define and average scalar potential by

$$\overline{S}(E) \approx S_0\frac{\langle\rho\rangle}{\rho_0} \tag{3.B.6}$$

which is used for the definition

$$M_1 \equiv M + \overline{S}(E)\ , \tag{3.B.7}$$

the effective mass of the projectile in the medium.

The second $\overline{S}$ value comes from a similar definition, but now using the Walecka model mean field values of the scalar potential:

$$\overline{S}_{\rm mft}(E) = S_{\rm mft}\frac{\langle\rho\rangle}{\rho_0} \tag{3.B.8}$$

where $S_{\rm mft} = -0.44M$, the nuclear matter value in QHD-I. Then we use

$$M_2 \equiv M + \overline{S}_{\rm mft}(E) \tag{3.B.9}$$

for the appropriate mass of the target nucleons. Typical values for M_1 and M_2 are from $0.80M$ to $0.90M$ (see Table 3.1). In fact, the two values are similar although M_1 is slightly larger than M_2.

3.B.3 Invariant Amplitude and Cross Sections

We now use the relativistic impulse approximation for the scattering amplitude of the projectile of momentum $\mathbf{p}_1$ by a target nucleon of momentum $\mathbf{p}_2$. We use the

Target	T_{lab} (MeV)	M_1/M	M_2/M	k_F (fm^{-1})	A_{eff}
^{12}C	200	0.85	0.84	0.97	4.33
^{12}C	400	0.86	0.84	0.98	4.63
^{12}C	500	0.91	0.87	0.91	2.86
^{12}C	800	0.92	0.90	0.83	1.97
^{40}Ca	200	0.82	0.81	1.04	8.53
^{40}Ca	400	0.83	0.80	1.05	9.70
^{40}Ca	500	0.90	0.85	0.94	6.01
^{40}Ca	800	0.91	0.89	0.85	4.25
^{208}Pb	200	0.82	0.82	1.02	12.44
^{208}Pb	400	0.86	0.83	0.98	12.81
^{208}Pb	500	0.88	0.85	0.95	11.86
^{208}Pb	800	0.82	0.82	1.02	12.44

Table 3.1

Fermi gas model parameters used for proton quasi-elastic calculations

form (1.C.7) for $\hat{\mathcal{F}}$. Using the notation of [Bj64], the invariant matrix element for the process in Fig. 3.2 is

$$\mathcal{M} = \sum_{i=S}^{T} \overline{U}_1(k_1, s_f)\lambda^i U(p_1, s_i)\, t_i(q, T_{\text{eff}})\, \overline{U}(k_2, s')\lambda^i U_2(p_2, s) \qquad (3.B.10)$$

where the λ^i are given in Table 1.2 and the functions $t_i(q, T_{\text{eff}})$ are related to the invariant amplitudes $F_i(q, T_{\text{eff}})$ introduced in Section 2.1 by:

$$t_i(q, T_{\text{eff}}) = \frac{8\pi k_{\text{eff}} E_{\text{eff}}}{M} F_i(q, T_{\text{eff}}) \qquad (3.B.11)$$

The kinematic quantities k_{eff}, T_{eff} and E_{eff} are the momentum, kinetic energy and total energy of the projectile in the frame where particle 2 is at rest:

$$T_{\text{eff}} = \frac{E_1 E_2 - \mathbf{p}_1 \cdot \mathbf{p}_2 - M^2}{M} \qquad (3.B.12a)$$

$$E_{\rm eff} = T + M = \sqrt{k_{\rm eff}^2 + M^2} \qquad (3.B.12b)$$

The NN amplitudes are evaluated at the values $T_{\rm eff}$ and NN center of mass effective scattering angle $\theta_{\rm eff}$

$$\theta_{\rm eff}^{\rm cm} = 2\sin^{-1}\left[\frac{-q^2}{2MT_{\rm eff}}\right]^{\frac{1}{2}} . \qquad (3.B.12c)$$

Note that these equations use the *free* momenta for evaluating the NN amplitudes: changes in the momenta from the free values come from the real part of V_c; V_c is small for these energies.

Squaring $\mathcal{M}$ and summing over the unobserved spins of the target nucleon gives:

$$\sum_{s,s'} \mathcal{M}^* \mathcal{M} = \sum_{i,j=S}^{T} {\rm Tr}_1 \left\{ \frac{\not k_1 + M_1}{2M_1} \left[\frac{1+\gamma_5 \not s_f}{2}\right] \lambda_j \frac{\not p_1 + M_1}{2M_1} \left[\frac{1+\gamma_5 \not s_i}{2}\right] \lambda_i \right\} \cdot {\rm Tr}_2 \left\{ \frac{\not k_2 + M_2}{2M_2} \lambda_j \frac{\not p_2 + M_2}{2M_2} \lambda_i \right\} t_i^* t_j \qquad (3.B.13)$$

where we have used

$$\sum_s U_2(k_2,s)\overline{U}_2(k_2,s) = \frac{\not k_2 + M}{2M} \qquad (3.B.14)$$

and

$$U_1(k,s)\overline{U}_1(k,s) = \frac{\not k + M_1}{2M_1}\left[\frac{1+\gamma_5 \not s}{2}\right] \qquad (3.B.15)$$

where the spin four–vector s satisfies $s^2 = -1$ and:

$$s_f \cdot k_1 = s_i \cdot p_1 = 0 \qquad (3.B.16)$$

Reference [Bj64] gives the general expression for the differential cross section in terms of $|\mathcal{M}|^2$. The differential cross section to scatter from spin state j to spin state i' with particle 2 unobserved is:

$$d\sigma_{j\to i'} = \frac{1}{|\mathbf{v}_1 - \mathbf{v}_2|} \frac{M_2^2}{E_1^* E_1'^*} \frac{d^3k_1}{(2\pi)^3} \int \frac{d^3k_2}{(2\pi)^3} \frac{M_2^2}{E_2^* E_2'^*} \cdot (2\pi)^4 \delta^4(k_1^* + k_2^* - p_1^* - p_2^*) \frac{1}{2} \sum_{s,s'} \mathcal{M}^* \mathcal{M} \qquad (3.B.17)$$

In this expression, the starred quantities use M_1 and M_2 for the masses for calculating the energy:

$$\begin{aligned} E_1^* &= \sqrt{\mathbf{p}_1^2 + M_1^2} \\ E_1^{*\prime} &= \sqrt{\mathbf{k}_1^2 + M_1^2} \\ E_2^* &= \sqrt{\mathbf{p}_2^2 + M_2^2} \\ E_2^{*\prime} &= \sqrt{\mathbf{k}_2^2 + M_2^2} \end{aligned} \tag{3.B.18}$$

Since the spinors are parametrized by M_1 and M_2 and not M, the $\frac{M}{E}$ factors and the δ function in the usual formula for $d\sigma$ are in terms of the E^*'s.

Use

$$|\mathbf{v}_1 - \mathbf{v}_2| \approx \frac{|\mathbf{p}_1|}{E_1^*} \tag{3.B.19}$$

as the approximate incident flux in nuclear matter. Also, use

$$d^2k_1 = k_1 E_1' dE_1' d\Omega_1' \tag{3.B.20}$$

(no * on E_1' here; we want the differential *free* energy for the cross section). The 3-space integral on $\mathbf{k}_2$ picks out the value

$$\mathbf{k}_2 = \mathbf{p}_1 + \mathbf{p}_2 - \mathbf{k}_1 \tag{3.B.21}$$

from the 3-space part of the energy–momentum conserving delta function. Finally, we now do the Fermi motion averaging over the possible values of $\mathbf{p}_2$. The result is:

$$\frac{d\bar{\sigma}_{j\to i'}}{d\Omega_1' dE_1'} = \frac{1}{|\mathbf{p}_1|}\frac{M_1^2 E_1'}{E_1'^*}\int_{p_{min}\le p_2\le k_F} \frac{d^3p_2}{\frac{4}{3}\pi k_F^3}\frac{M_2^2}{E_2^* E_2'^*} \cdot \frac{\delta(E_1^* + E_2^* - E_2'^* - E_1'^*)}{(2\pi)^2}\frac{1}{2}\sum_{s,s'} \mathcal{M}^*\mathcal{M} \tag{3.B.22}$$

where the minimum momentum for the target nucleon is:

$$p_{\min} = \left| \frac{|\mathbf{q}|}{2} - \frac{\omega}{2}\sqrt{1 - \frac{4M_2^2}{q^2}} \right| . \tag{3.B.23}$$

The integral over d^3p_2 is evaluated as follows:

$$\int_{p_{\min}\le p_2\le k_F} d^3p_2\,\delta(E_1^* + E_2^* - E_2^{*\prime} - E_1^{*\prime}) = \int_{p_{\min}}^{k_F} dp_2 \frac{p_2 E_2^{*\prime}}{|\mathbf{q}|}\int d\phi\Big|_{\chi=\chi_0} \qquad (3.B.24)$$

Here the angle χ between $\mathbf{p}_2$ and $\mathbf{q}$ is fixed by the energy conserving delta function:

$$\cos\chi = \cos\chi_o = \frac{q^2 + 2\omega E_2^*}{2p_2|\mathbf{q}|} \qquad (3.B.25)$$

where the four–momentum transfer is

$$\begin{aligned}\mathbf{q} &= \mathbf{k}_2 - \mathbf{p}_2 = \mathbf{p}_1 - \mathbf{k}_1\\ \omega &= E_2^{*\prime} - E_2^* = E_1^* - E_1^{*\prime}\end{aligned} \qquad (3.B.26)$$

Then this gives:

$$\frac{d\bar{\sigma}_{j\to i'}}{d\Omega_1' dE_1'} = \frac{|\mathbf{k}_1|}{|\mathbf{p}_1|}\frac{M_1^2 E_1'}{E_1'^*}\int_{\substack{p_{\min}\le p_2\le k_F\\ 0\le\phi\le 2\pi}} \frac{dp_2\,d\phi}{\frac{4}{3}\pi k_F^3}\frac{p_2 E_2'^*}{|\mathbf{q}|}\frac{M_2^2}{E_2^* E_2'^*} \cdot \frac{1}{(2\pi)^2}\frac{1}{2}\sum_{s,s'}\mathcal{M}^*\mathcal{M}\Big|_{\chi=\chi_0} \qquad (3.B.27)$$

Now define

$$\Theta(\mathbf{p}_2) = \frac{|\mathbf{k}_1|}{|\mathbf{p}_1|}M_1^2\frac{E_1'}{E_1'^*}\frac{1}{\frac{4}{3}\pi k_F^3}\frac{M_2^2}{E_2^* E_2'^*}\frac{p_2 E_2'^*}{|\mathbf{q}|} \qquad (3.B.28)$$

then the formula simplifies to

$$\frac{d\bar{\sigma}_{j\to i'}}{d\Omega_1' dE_1'} = \int_{\substack{p_{\min}\le p_2\le k_F\\ 0\le\phi\le 2\pi}} dp_2\,d\phi\,\Theta(\mathbf{p}_2)\frac{1}{2}\sum_{s,s'}\mathcal{M}^*\mathcal{M}\Big|_{\chi=\chi_0} \qquad (3.B.29)$$

3.B.3 Observables

To get the unpolarized cross section, we sum (3.B.29) on spins s_i and s_f with a factor of $\frac{1}{2}$ (average over the initial spins):

$$\frac{d\bar{\sigma}}{d\Omega_1' dE_1'}\Big|_{\text{unpol}} = \int_{\substack{p_{\min}\le p_2\le k_f\\ \chi=\chi_0}} dp_2\,d\phi\Theta(\mathbf{p}_2)\frac{1}{4}\sum_{s,s',s_i,s_f}\mathcal{M}^*\mathcal{M} \qquad (3.B.30)$$

The analyzing power A_y is:

$$
\begin{aligned}
A_y &= \frac{\frac{d\bar{\sigma}}{d\Omega_1' dE_1'}(\mathbf{s}_f = \hat{n}) - \frac{d\bar{\sigma}}{d\Omega_1' dE_1'}(\mathbf{s}_f = -\hat{n})}{\frac{d\bar{\sigma}}{d\Omega_1' dE_1'}(\mathbf{s}_f = \hat{n}) + \frac{d\bar{\sigma}}{d\Omega_1' dE_1'}(\mathbf{s}_f = -\hat{n})} \\
&= \frac{\int dp_2\, d\phi \Theta(\mathbf{p}_2) \frac{1}{4} \sum_{s_i,s,s'} \{\mathcal{M}^* \mathcal{M}(\mathbf{s}_f = \hat{n}) - \mathcal{M}^* \mathcal{M}(\mathbf{s}_f = -\hat{n})\}}{\int dp_2\, d\phi \Theta(\mathbf{p}_2) \frac{1}{4} \sum_{s_i,s,s'} \{\mathcal{M}^* \mathcal{M}(\mathbf{s}_f = \hat{n}) + \mathcal{M}^* \mathcal{M}(\mathbf{s}_f = -\hat{n})\}} \\
&= \frac{\int dp_2\, d\phi \Theta(\mathbf{p}_2) \frac{1}{4} \sum_{s_i,s,s'} \{\mathcal{M}^* \mathcal{M}(\mathbf{s}_f = \hat{n}) - \mathcal{M}^* \mathcal{M}(\mathbf{s}_f = -\hat{n})\}}{\frac{d\bar{\sigma}}{d\Omega_1' dE_1'}\Big|_{\text{unpol}}}
\end{aligned}
\tag{3.B.31}
$$

The spin correlation functions, for initial spin direction j going to final spin direction i', are given by:

$$
\begin{aligned}
D_{i'j} &= \frac{\frac{d\bar{\sigma}}{d\Omega_1' dE_1'}(j \to i') - \frac{d\bar{\sigma}}{d\Omega_1' dE_1'}(j \to -i') - \frac{d\bar{\sigma}}{d\Omega_1' dE_1'}(-j \to i') + \frac{d\bar{\sigma}}{d\Omega_1' dE_1'}(-j \to -i')}{\frac{d\bar{\sigma}}{d\Omega_1' dE_1'}(j \to i') + \frac{d\bar{\sigma}}{d\Omega_1' dE_1'}(j \to -i') + \frac{d\bar{\sigma}}{d\Omega_1' dE_1'}(-j \to i') + \frac{d\bar{\sigma}}{d\Omega_1' dE_1'}(-j \to -i')} \\
&= \frac{\int dp_2\, d\phi \Theta(\mathbf{p}_2) \frac{1}{4} \sum_{s,s'} \{\mathcal{M}^* \mathcal{M}(j \to i') - \mathcal{M}^* \mathcal{M}(j \to -i') - \mathcal{M}^* \mathcal{M}(-j \to i') + \mathcal{M}^* \mathcal{M}(-j \to -i')\}}{\int dp_2\, d\phi \Theta(\mathbf{p}_2) \frac{1}{4} \sum_{s,s'} \{\mathcal{M}^* \mathcal{M}(j \to i') + \mathcal{M}^* \mathcal{M}(j \to -i') + \mathcal{M}^* \mathcal{M}(-j \to i') + \mathcal{M}^* \mathcal{M}(-j \to -i')\}}
\end{aligned}
\tag{3.B.32}
$$

The denominator is again the unpolarized cross section, so this becomes

$$
D_{i'j} = \frac{\int dp_2\, d\phi \Theta(\mathbf{p}_2) M_{i'j}}{\frac{d\bar{\sigma}}{d\Omega_1' dE_1'}\Big|_{\text{unpol}}} \tag{3.B.33}
$$

where

$$
\begin{aligned}
M_{i'j} = &\frac{1}{4} \sum_{s_2,s_2'} \Big\{ \mathcal{M}^* \mathcal{M}(\mathbf{s}_i = \hat{j}, \mathbf{s}_f = \hat{i}') - \mathcal{M}^* \mathcal{M}(\mathbf{s}_i = \hat{j}, \mathbf{s}_f = -\hat{i}') \\
&- \mathcal{M}^* \mathcal{M}(\mathbf{s}_i = -\hat{j}, \mathbf{s}_f = \hat{i}') + \mathcal{M}^* \mathcal{M}(\mathbf{s}_i = -\hat{j}, \mathbf{s}_f = -\hat{i}') \Big\}
\end{aligned}
\tag{3.B.34}
$$

The traces needed to evaluate (3.B.31)–(3.B.34) were found with a computer algebra program. The needed spin sums are:

$$\sum_{s,s',s_i,s_f} \mathcal{M}^*\mathcal{M} = t_S^* t_S(1+K_1\cdot P_1)(1+K_2\cdot P_2) + t_P^* t_P(1-K_1\cdot P_1)(1-K_2\cdot P_2)$$
$$+ 2t_V^* t_V[2 - K_1\cdot P_1 - K_2\cdot P_2 + K_1\cdot K_2 P_1\cdot P_2 + K_1\cdot P_2 K_2\cdot P_1]$$
$$+ 2t_A^* t_A[2 + K_1\cdot P_1 + K_2\cdot P_2 + K_1\cdot K_2 P_1\cdot P_2 + K_1\cdot P_2 K_2\cdot P_1]$$
$$+ 8t_T^* t_T[3 - K_1\cdot P_1 K_2\cdot P_2 + 2K_1\cdot K_2 P_1\cdot P_2 + K_1\cdot P_2 K_2\cdot P_1]$$
$$+ 2\mathrm{Re}(t_V^* t_S - 6t_T^* t_A)[K_1\cdot K_2 + K_1\cdot P_2 + K_2\cdot P_1 + P_1\cdot P_2]$$
$$+ 2\mathrm{Re}(t_A^* t_P - 6t_T^* t_V)[K_2\cdot P_1 + K_1\cdot P_2 - K_1\cdot K_2 - P_1\cdot P_2]$$
$$+ 4\mathrm{Re}(t_A^* t_V - t_T^* t_S - t_T^* t_P)[K_1\cdot K_2 P_1\cdot P_2 - K_2\cdot P_1 K_1\cdot P_2] \qquad (3.B.35)$$

where $K_i = k_i/M_i$ and $P_i = p_i/M_i$.

$$\sum_{s_i,s,s'} \mathcal{M}^*\mathcal{M} = 4\,\mathrm{Im}\left[t_S^* t_V + 2t_T^* t_A - \frac{M_1}{M_2}(t_A^* t_V + 2t_T^* t_S)\right]$$
$$\cdot\left\{\tfrac{1}{2}(E_2 + E_2^{*\prime})\mathbf{p}_1\times\mathbf{k}_1 + \tfrac{1}{2}E_1^*\mathbf{k}_1\times(\mathbf{p}_2+\mathbf{k}_2) - \tfrac{1}{2}E_1^{*\prime}\mathbf{p}_1\times(\mathbf{p}_2+\mathbf{k}_2)\right\}\cdot\frac{\mathbf{s}_f}{M_1^2 M_2} \qquad (3.B.36)$$

and the lengthy expression for $M_{i'j}$ is given in Appendix D.

Now to get the cross section per nucleus, we estimate the effective number of nucleons by an eikonal weighting procedure similar to the one in Sec. 3.B.2:

$$A_{\mathrm{eff}} = \frac{\int b\,db\,T(b)\int dz\,\rho(b,z)}{\int b\,db\int dz\,\rho(b,z)}A \qquad (3.B.37)$$

Values for A_{eff} are listed in Table 3.1. They are much smaller than A and depend on energy. Then we assume:

$$Z_{\mathrm{eff}} = \frac{Z}{A}A_{\mathrm{eff}} \qquad N_{\mathrm{eff}} = \frac{N}{A}A_{\mathrm{eff}} \qquad (3.B.38)$$

and we assume the total scattering from Z_{eff} protons and N_{eff} neutrons is:

$$\frac{d^3\overline{\sigma}}{d\Omega_1' dE_1'} = Z_{\mathrm{eff}}\frac{d^3\overline{\sigma}(pp)}{d\Omega_1' dE_1'} + N_{\mathrm{eff}}\frac{d^3\overline{\sigma}(pn)}{d\Omega_1' dE_1'} \qquad (3.B.39)$$

The total analyzing power is then

$$A_y = \left[Z_{\text{eff}} \frac{d^3\overline{\sigma}\,(pp)}{d\Omega_1' dE_1'} A_y(pp) + N_{\text{eff}} \frac{d^3\overline{\sigma}\,(pn)}{d\Omega_1' dE_1'} A_y(pn) \right] \Big/ \frac{d^3\overline{\sigma}}{d\Omega_1' dE_1'} \qquad (3.B.40)$$

and the total $D_{i'j}$ is:

$$D_{i'j} = \left[Z_{\text{eff}} \frac{d^3\overline{\sigma}\,(pp)}{d\Omega_1' dE_1'} D_{i'j}(pp) + N_{\text{eff}} \frac{d^3\overline{\sigma}\,(pn)}{d\Omega_1' dE_1'} D_{i'j}(pn) \right] \Big/ \frac{d^3\overline{\sigma}}{d\Omega_1' dE_1'} \qquad (3.B.41)$$

To summarize the calculation, k_F for the Fermi gas model and the spinor paramters M_1 and M_2 are calculated from (3.B.7) and (3.B.9). Cross sections and spin observables for (pp) and (pn) scattering are individually calculated with Eqs. (3.B.30)–(3.B.32), which involves a numerical integration of p_2: the Arndt amplitudes are evaluated at effective energies and scattering angles (3.B.12a–c) to give the functions $t_i(q, E)$ to use in formulae (3.B.13). Then, effective nucleon numbers (3.B.37)–(3.B.38) are used to get the nuclear cross sections and spin observables (3.B.39)–(3.B.41).

3.B.4 (p,n) charge exchange reaction

We also apply the formalism of this section to the (p,n) charge exchange reaction (inclusive (p,n) scattering). If we treat the Arndt amplitude as all "direct", then the charge exchange amplitude is the isovector amplitude:

$$F_{\text{ch-ex}} = F_{pp} - F_{pn} \qquad (3.B.42)$$

to be used for protons scattering from the target neutrons. So for the charge exchange observables we use (3.B.42) for the amplitudes in (3.B.13), to give a (pn) cross-section, and (3.B.39) to give a nuclear cross-section, with $Z_{\text{eff}} = 0$.

The comparative strength of the Lorentz components of the isovector amplitude (3.B.42) is very different from that of the isovector amplitude

$$F_{\text{av}} = F_{pp} + F_{pn} \qquad (3.B.43)$$

especially the pseudoscalar component, so that the (p,n) reaction can provide new information on the form of $\hat{\mathcal{F}}$. Because of the importance of the pseudoscalar amplitude in charge exchange, we make a point of investigating the coupling choice $\lambda^P_{pv} = \pm\frac{\not{q}\gamma_5}{2M}$ in place of the choice $\lambda^P_{ps} = \gamma_5$ of the original RIA (Table 1.2). As mentioned in Chapter 2, the fit to the NN data is unchanged by this choice, but when this coupling is used for spinors in the nuclear medium, this choice gives:

$$\overline{U}_{1'}(\mathbf{k}_1)\lambda^P_{pv}U(\mathbf{p}_1) = \overline{U}_{1'}(\mathbf{k}_1)\frac{\not{q}\gamma_5}{2M}U_1(\mathbf{p}_1) = \frac{M_1}{M}\overline{U}_1(\mathbf{k}_1)\lambda^P_{ps}U(\mathbf{p}_1) \qquad (3.B.44)$$

i.e. they are different by a factor of $\frac{M_1}{M}$ with another factor of $\frac{M_2}{M}$ for the second vertex in Fig 3.1. Then for the pseudovector model, we multiply by these factors:

$$F^P_{pv} = \frac{(M_1 M_2)}{M^2}F^P_{ps} \qquad (3.B.45)$$

to get the desired F^P amplitude.

3.C Results

In this section, results are presented for cross sections and spin observables calcualted using the formalism of section 3.B. First, cross sections at 800 MeV are compared to published (though recently corrected) LAMPF data [Ch80]. then spin observables at $T_{\rm lab}$=500 MeV and $T_{\rm lab}$ =420 MeV are compared with recent Lampf and TRIUMF experiments. Then, predictions are made for spin observables at several other angles and energies. Finally, calculations for the (p,n) reaction are presented

3.C.1 800 MeV (p,p')

Cross sections for 800 MeV proton scattering from ^{12}C, ^{40}Ca and ^{208}Pb are shown in Figs. 3.3–5. The data are taken from Ref. [Ch80], but its normalization has recently been corrected; so the comparison should be taken only as a rough indicator of the

success of the normalization (via A_{eff}, Eq. (3.B.37)), the position of the peak center, and the shape of the peak.

Calculations with $M_1 = M_2 = M$ (nonrelativistic, solid curves) and with effective M's from Table 3.1 (relativistic, dashed curves) are shown along with the LAMPF data as published in [Ch80]. (The normalization is as presented in the calculation of 3.B and has not been adjusted.) The peak positions and widths of both calculations agree with this data set. The normalization is good in the middle of the range of angles shown, but is wrong by up to 50% at the extremes. The data do not have simple parabolic shapes, indicating modes of excitation not covered by the simple Fermi gas model and giving strength at the high and low ω values for the peak.

The use of relativistic wavefunctions ($M_1 \neq M$, $M_2 \neq M$) gives a shift in the peak position of about 10 MeV. This is to be expected from the binding from the scalar field. The position of the quasielastic peak is the energy lost to a stationary target nucleon *in the medium*. If the target particle picks up 3–momentum q, then

$$\omega_{\text{peak}} = (\mathbf{q}^2 + M_2^2)^{\frac{1}{2}} - M_2 \qquad (3.C.1)$$

where it was was assumed that the vector and potential and M_2 are independent of energy. Thus, the shift of the quasielastic peak due to the scalar potential is:

$$\Delta E = (\mathbf{q}^2 + M_2^2)^{\frac{1}{2}} - (\mathbf{q}^2 + M^2)^{\frac{1}{2}} - M_2 + M \qquad (3.C.2)$$

which is about 10 MeV for $|\mathbf{q}| \approx$450 MeV and the M_2's in Table 3.1.

While in a few instances the relativistic calculation gives slightly better agreement with the data, the change is not significant and one must conclude that there is no clear signature for relativity in the cross section.

The same binding energy shift is larger in quasifree electron scattering, where the effective mass of the target nucleons (as given by (3.B.9) with $T(b) = 1$) is about $.7M$, compared to the effective mass $M_2 \approx 0.9M$ for proton scattering. In fact,

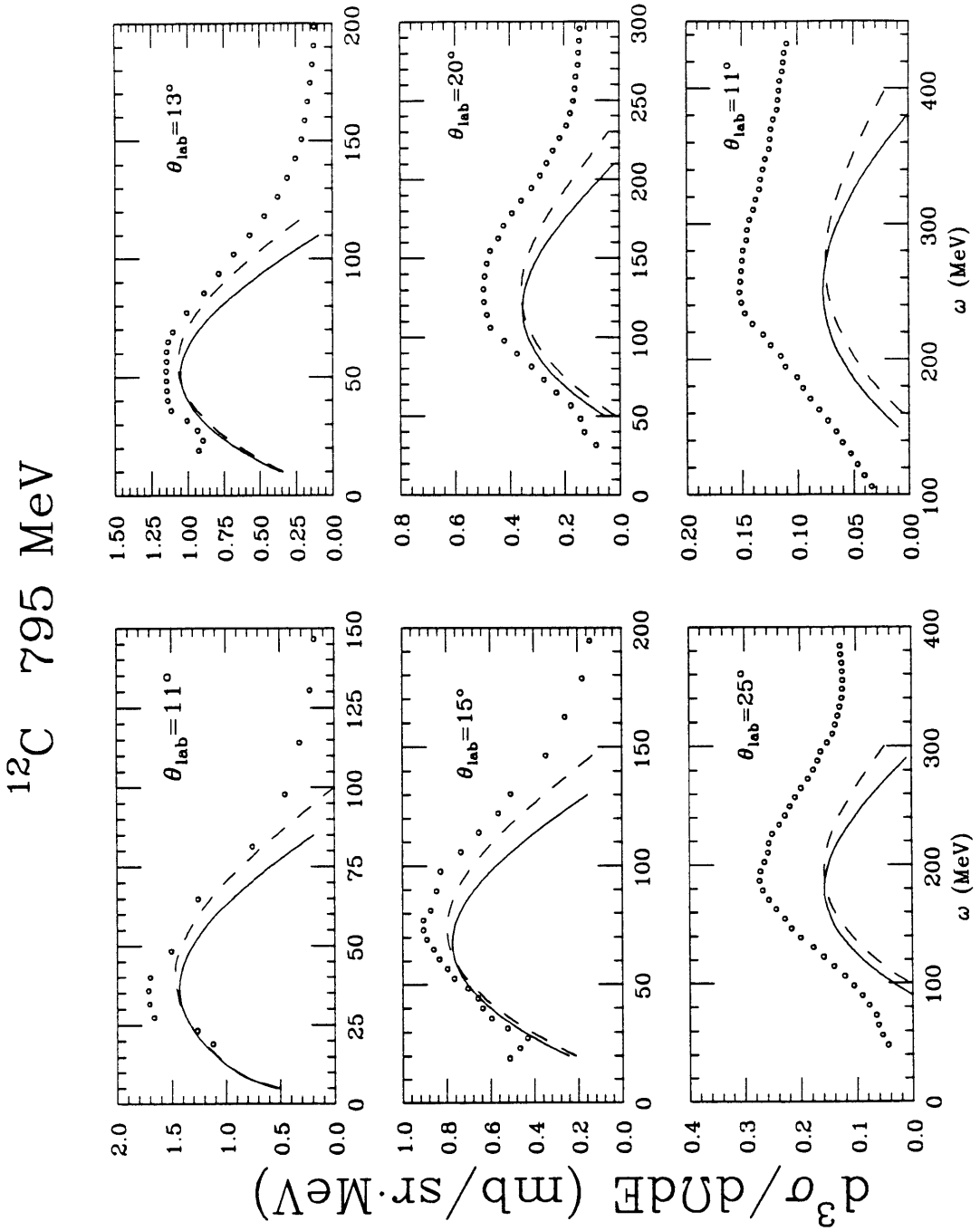

Fig. 3.3 Cross section vs. energy loss for (p,p') scattering on ^{12}C at 795 MeV and various scattering angles. The solid curves use $M_1 = M_2 = M$. The dashed curves use effective relativistic masses for M_1 and M_2. Data are from Chrien et al, Ref. [Ch80].

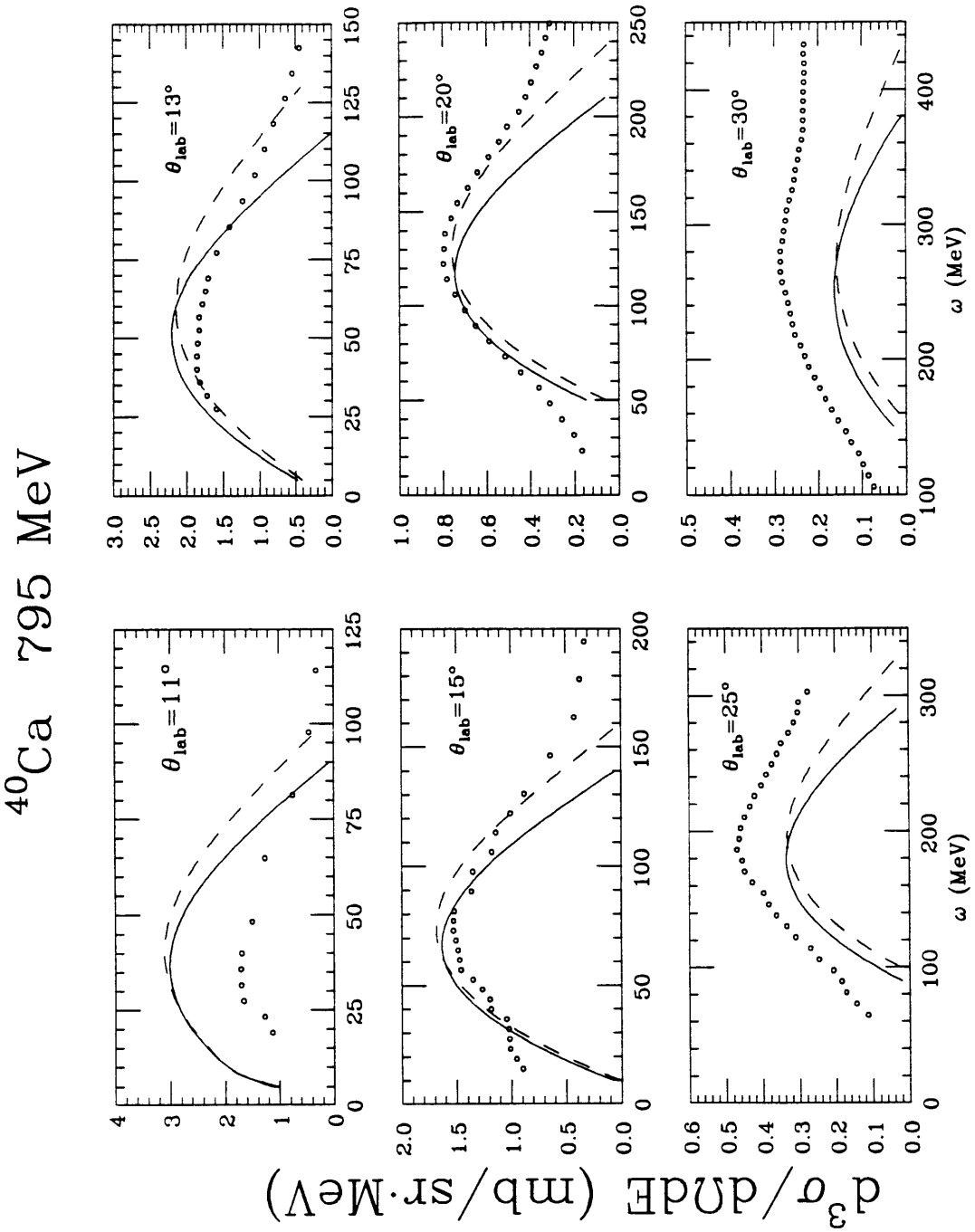

Fig. 3.4 Same as Fig. 3.3 but for (p,p') scattering on ^{40}Ca. Data are from Ref. [Ch80].

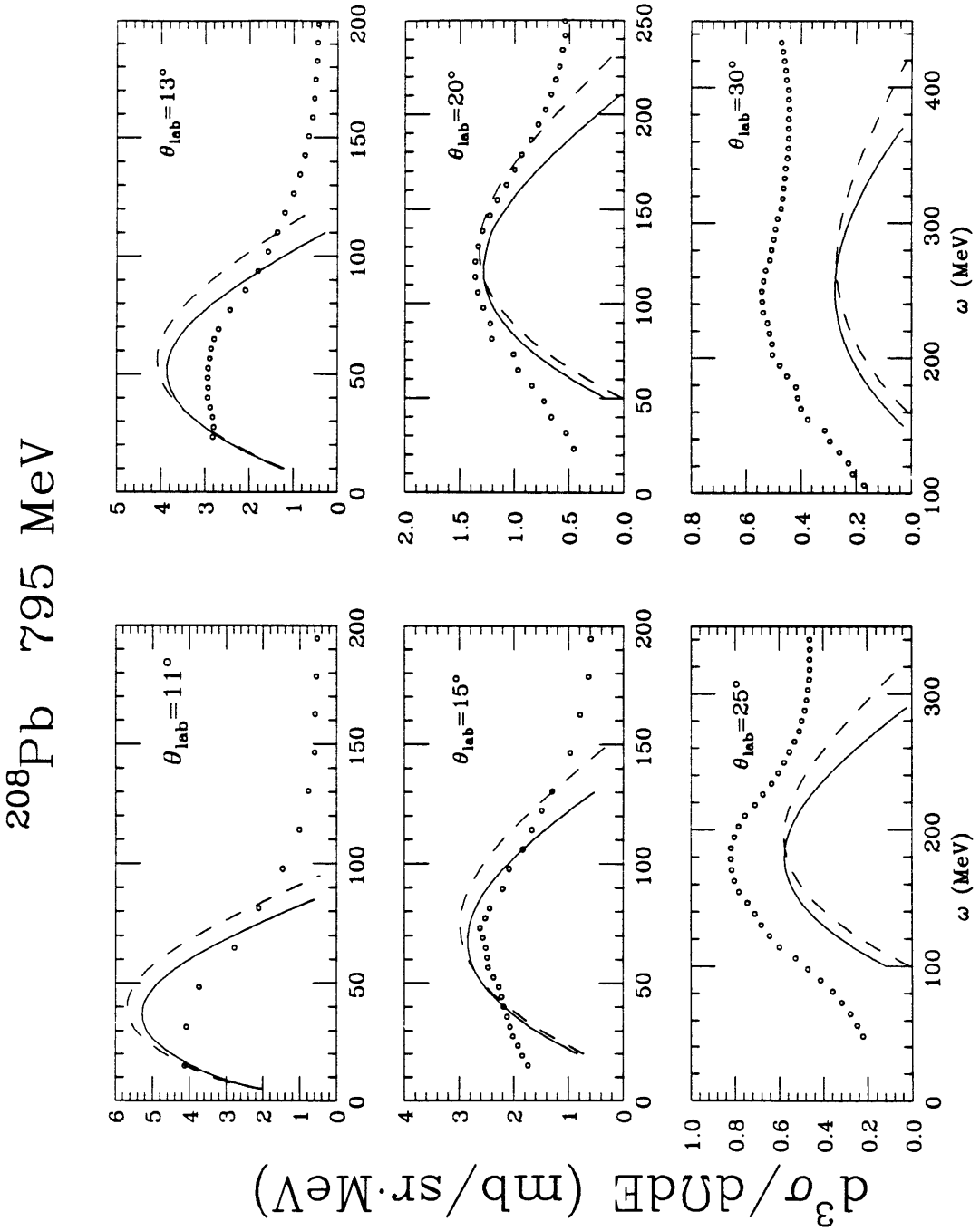

Fig. 3.5 Same as Fig. 3.3 but for (p,p') scattering on ^{208}Pb. Data are from Ref. [Ch80].

Rosenfelder [Ro80] found that a relativistic Fermi gas model with $\langle M^* \rangle$=0.71M gave a good description of the data for 800 MeV quasielastic electron scattering from ^{40}Ca. Thus, the relativistic Fermi gas model is consistent with both electron and proton data.

3.C.2 300–500 MeV (p,p')

Spin observables at 500 MeV and $\theta_{\rm lab} = 18.5°$ have been measured at LAMPF [Ca85]. At this energy and lab angle, the quasielastic peak occurs at $|\mathbf{q}| \approx 300$ MeV and $\omega \approx 60$ MeV. Data are plotted in Fig. 3.6–7, along with the nonrelativistic (solid) and relativistic (dashed) calculations. The two other sets of curves will be discussed below. The polarization was found to be equal to the analyzing power, within errors. This is true for the theoretical model used here, although it is not necessary for inelastic scattering.

For both ^{40}Ca and ^{208}Pb, the polarization was found to be about 40% below the free value at the quasielastic peak. The RPWIA model also predicts such a decrease in A_y. The correction to A_y from including spin-orbit distortions were estimated in [Ho85] for Pb, at the peak; the size and direction of these corrections are indicated in Fig. 3.7 by the small arrows at the quasi-elastic peak position. While they do decrease A_y, this correction is much smaller than the observed decrease. Without a change in the NN interaction, the decrease in A_y is hard to explain, and all nonrelativistic calculations to date have predicted A_y close to the free value.

The shape of the A_y data for Pb is not predicted well by either calculation for the Fermi gas model. At low ω, the increase is probably due to nuclear structure effects; nonrelativistic calculations based on the RPA surface response theory of Bertsch et al [Es84] give such an increase in A_y at low ω. But the RPA corrections are small at ω =66 MeV and so don't explain the reduction in A_y at the quasi-elastic peak. The slope may also have some contribution from multiple scattering, which would be consistent with the fact that the slope is not as large for ^{40}Ca.

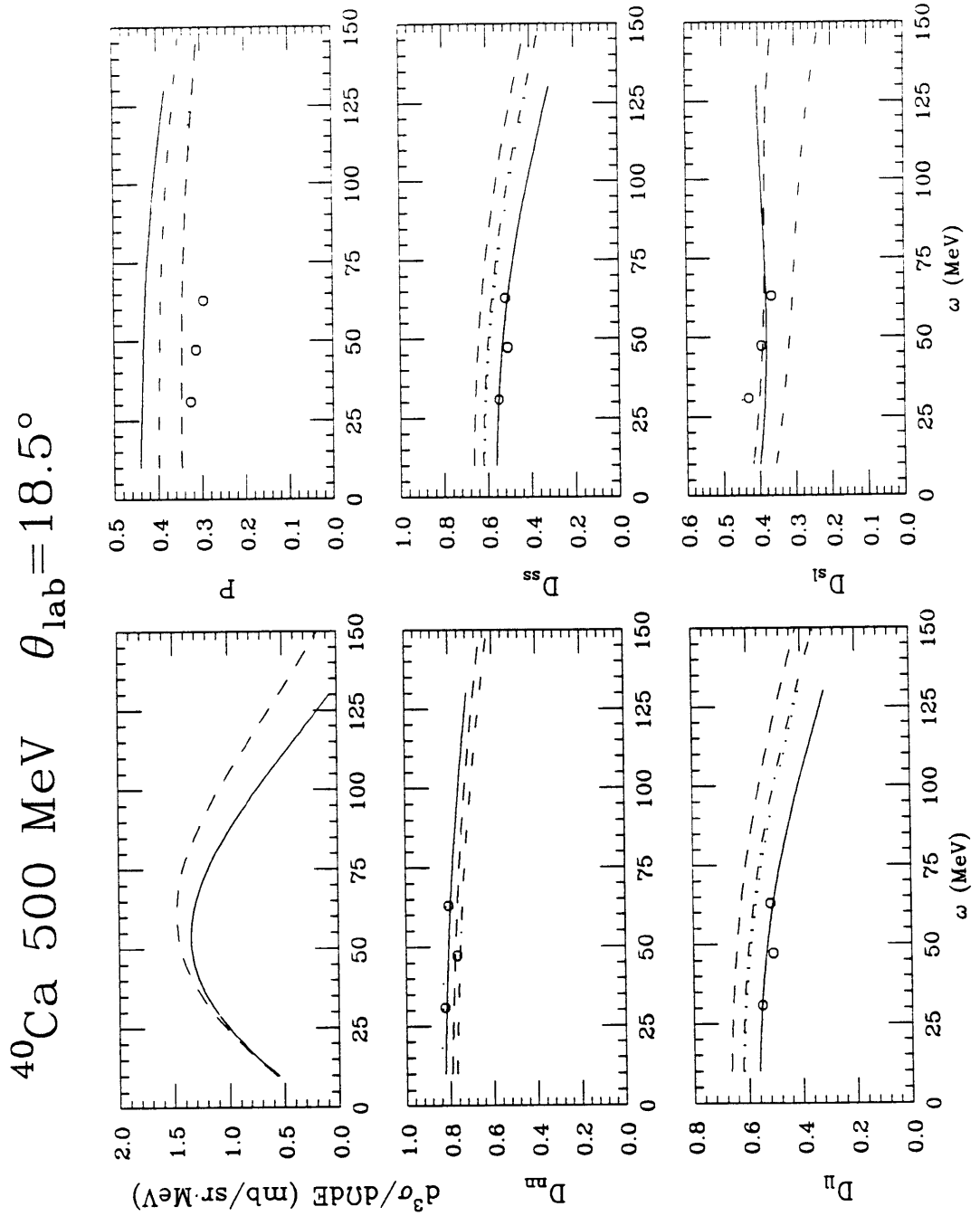

Fig. 3.6 Cross section and spin observables for (p,p') scattering on ^{40}Ca at 500 MeV, $\theta_{\rm lab} = 18.5°$. Solid curves use free masses, $M_1 = M_2 = M$. Dashed curves use relativistic effective masses for M_1 and M_2. Dotted curves include only projectile relativity, $M_1 \neq M_2 = M$. Dot-dash curves include only target relativity, $M_2 \neq M_1 = M$. Data are from Ref. [Ca85].

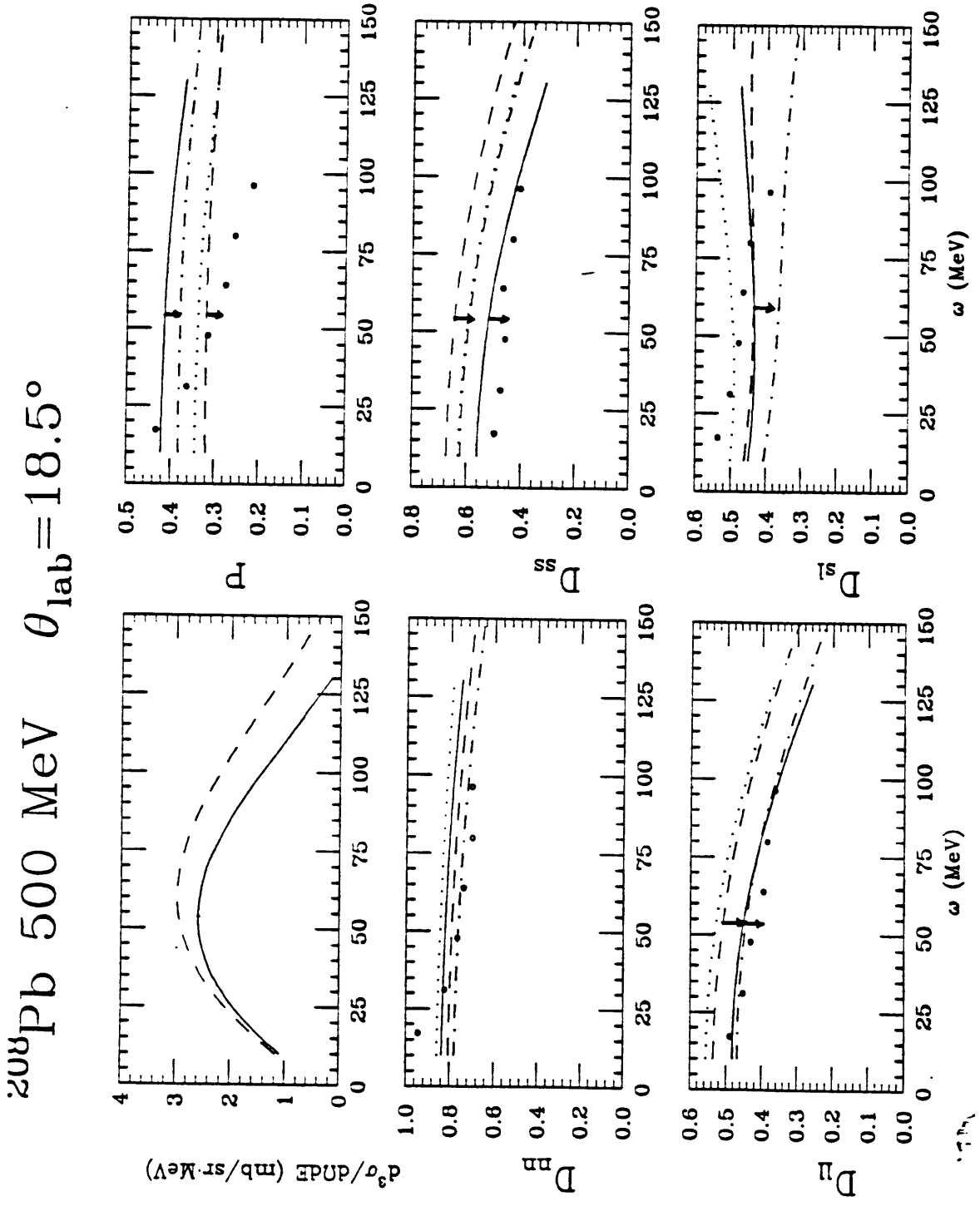

Fig. 3.7 Same as Fig. 3.6 but for (p,p') scattering on ^{208}Pb. Data are from Ref. [Ca85]. Small arrows are explained in the text.

The results are mixed for the other observables. The measured D_{nn} is slightly smaller than the free calculation, in agreement with the M^* prediction, although generally for D_{nn} and $D_{s'l}$ the data are close to the free *and* M^* predictions. But for D_{ss} and D_{ll}, the relativistic model predicts an increase from the free values, which is not seen in the data. Part of this increase may be cancelled by $\mathbf{L}\cdot\mathbf{S}$ distortions, estimated in [Ho86] to reduce both $D_{l'l}$ and $D_{s's}$. With $\mathbf{L}\cdot\mathbf{S}$ corrections included, the data may lie between the two curves, making this measurement inconclusive with the target model used here.

By using different spinors for the target and projectile nucleons in the formalism of Section 3.B one can examine the separate roles of M_1 and M_2 in giving deviations from the free calculation. In Figs 3.6–3.7, the dotted curves use only projectile relativity, i.e. $M_1 \neq M_2 = M$. The dash-dot curves use only target relativity, $M_2 \neq M_1 = M$. While for the polarization, the projectile's wavefunction gives most of the change for the relativistic calculation, for $D_{s's}$ and $D_{l'l}$, the contributions are of comparable size, constructive in the first case and cancelling in the second. So the full set of spin observables in general shows sensitivity to target *and* projectile wavefunctions.

Fig. 3.8 presents some recent *preliminary* TRIUMF data for 420 MeV proton scattering on ^{12}C at $\theta_{\rm lab} = 23°$. The result is similar to what was seen at 500 MeV for ^{40}Ca and ^{208}Pb: relativistic spinors reduce A_y to improve agreement with the data while increasing $D_{s's}$ and $D_{l'l}$ away from the data. Also, note that the slope of the spin observables is not a problem for the theory, as with Pb at 500 MeV.

In Figs 3.9–13, various other predictions for observables are shown. Observables for 300 MeV and 400 MeV scattering form Ca are predicted for free and relativistic calculations. There are now large differences for $D_{s's}$ and $D_{s'l}$ at forward angles. However, at these lower energies, nucleon exchange and the density dependence of the amplitudes, shown to be important in Chapter 2 for elastic scattering should be considered (along with corrections for $\mathbf{L}\cdot\mathbf{S}$ distortions and nuclear structure).

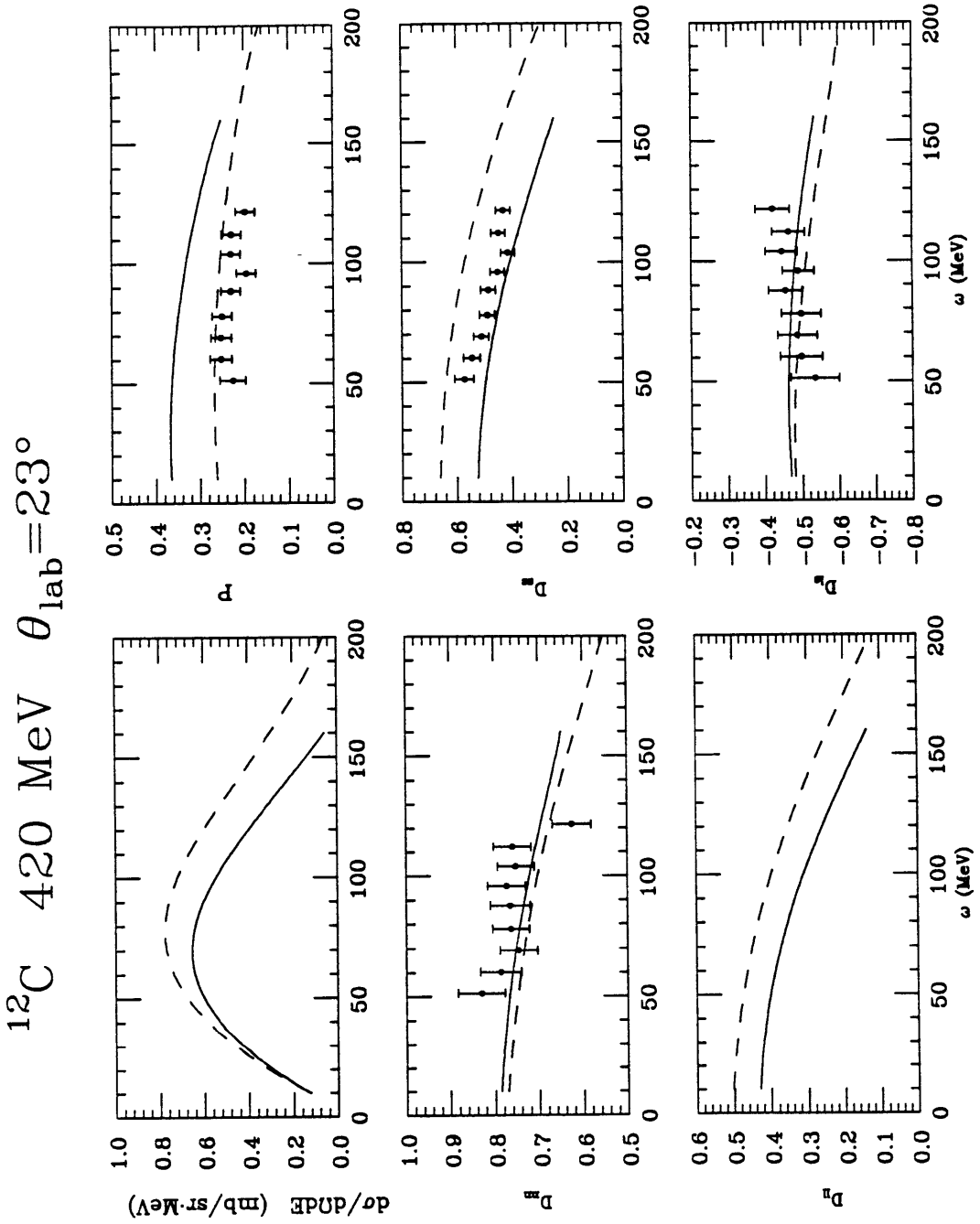

Fig. 3.8 Scattering observables for 420 MeV proton scattering on ^{12}C. Solid curve uses nonrelativistic wavefunctions; dashed curve uses relativistic wavefunctions. Data are from Ref. [Hi87]

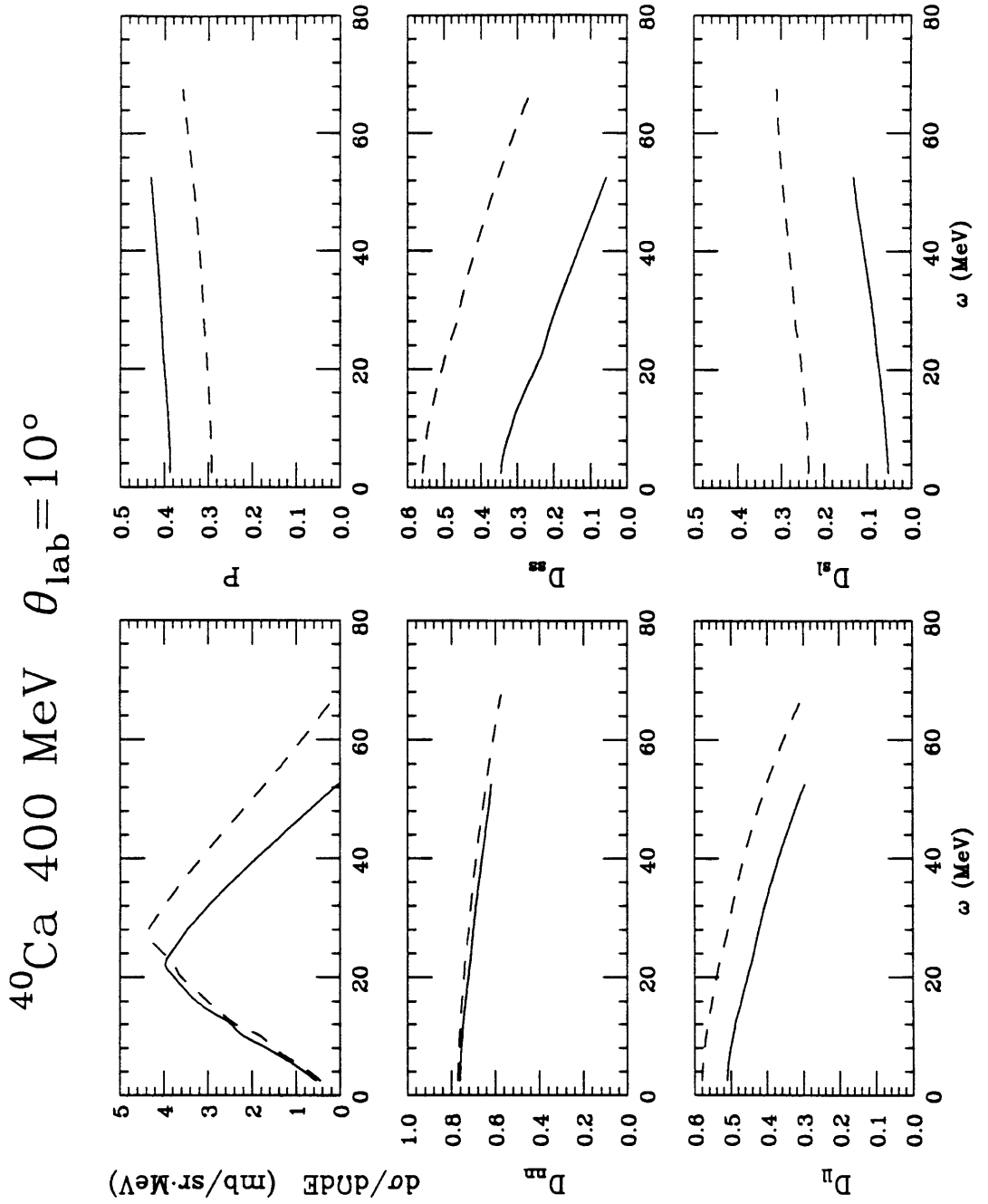

Fig. 3.9 Scattering observables for (p, p') scattering on Ca at 400 MeV, at $\theta_{\rm lab} = 10°$.

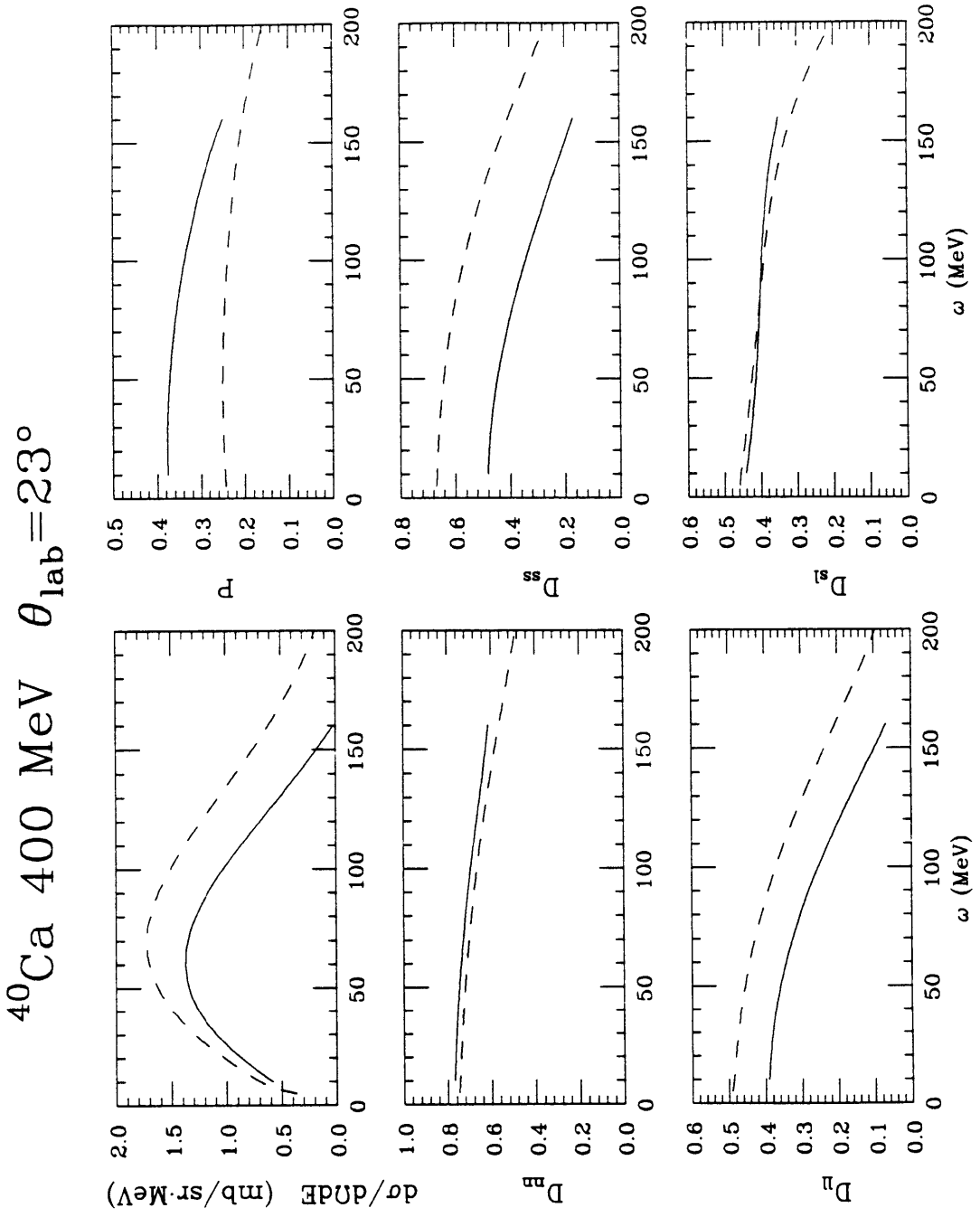

Fig. 3.10 Same as Fig. 3.9. but for scattering at $\theta_{\rm lab} = 23°$

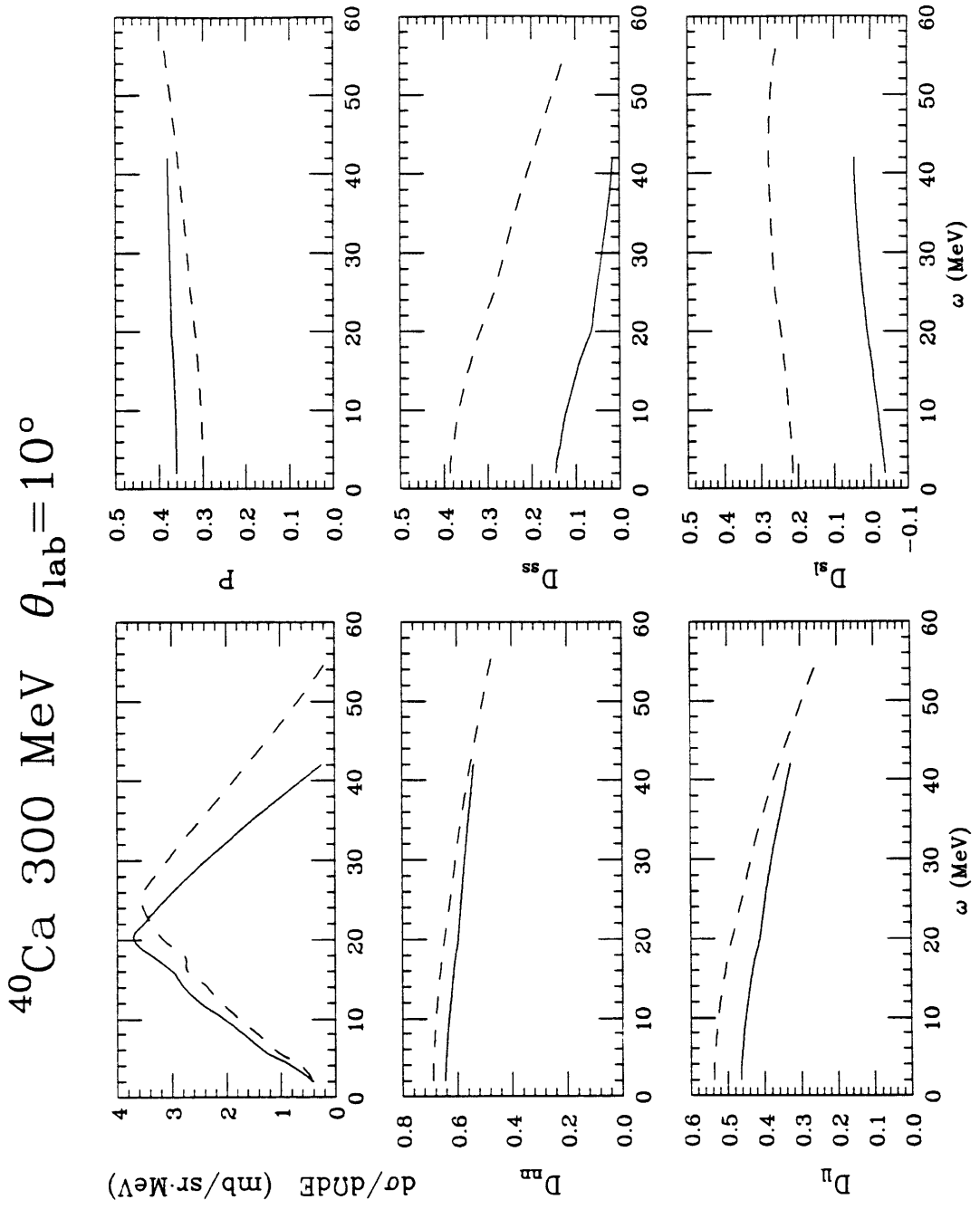

Fig. 3.11 Observables for (p,p') scattering on ^{40}Ca at 300 MeV at $\theta_{\rm lab} = 10°$. The solid curve uses $M_1 = M_2 = M$. The dashed curve uses relativistic effective masses for M_1 and M_2.

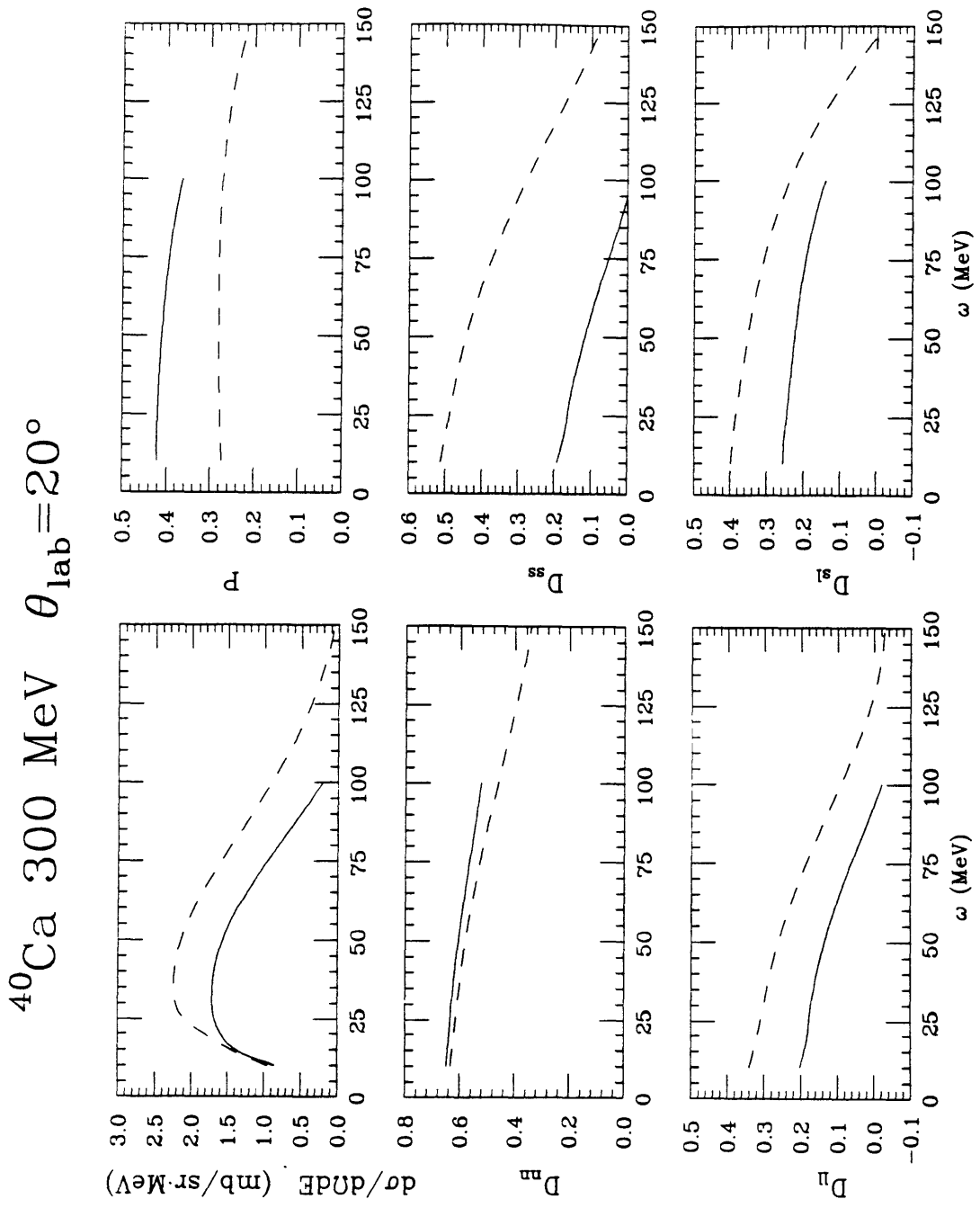

Fig. 3.12 Same as Fig. 3.11, but for scattering at $\theta_{\rm lab} = 20°$.

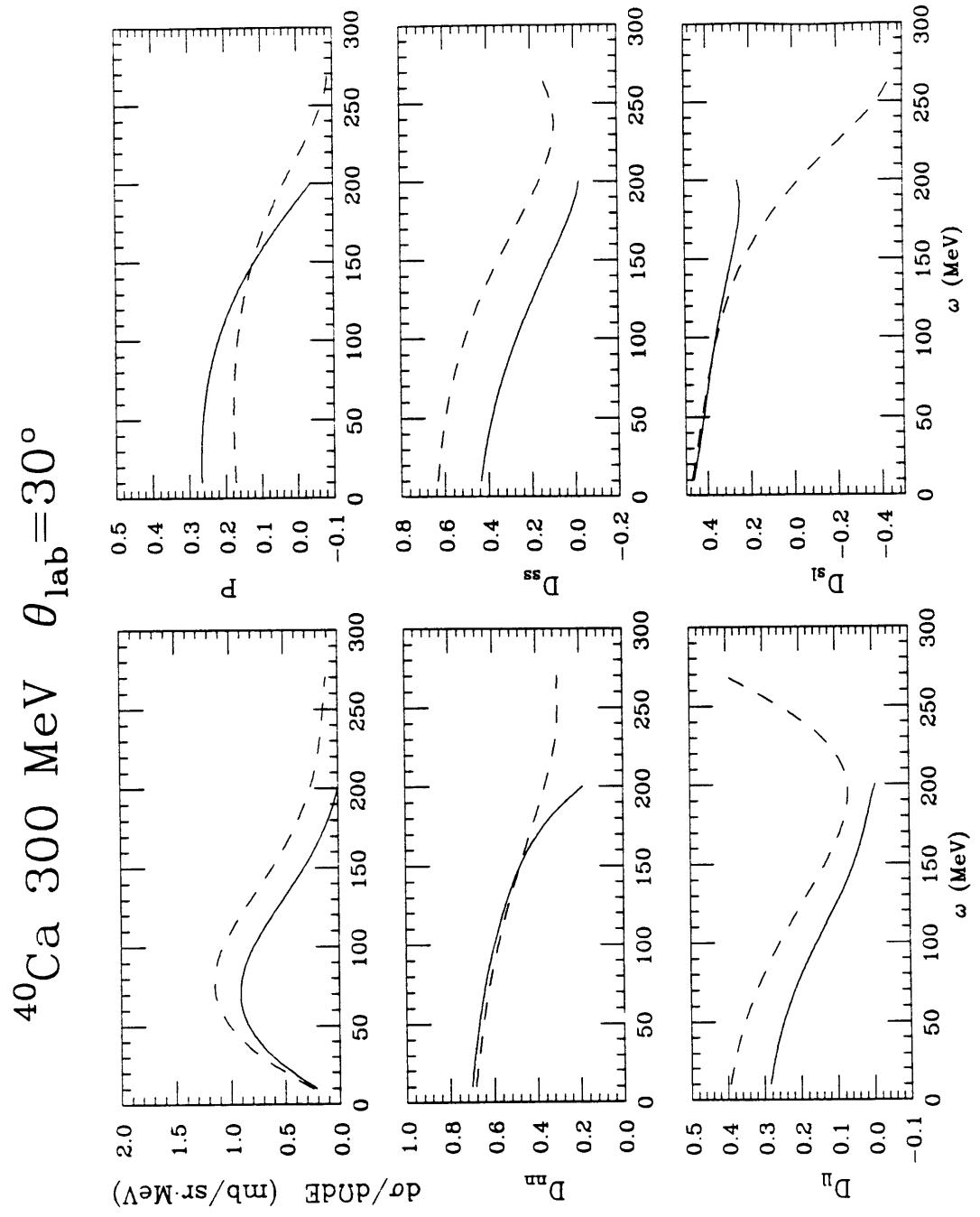

Fig. 3.13 Same as Fig. 3.11, but for scattering at $\theta_{\rm lab} = 30°$.

3.C.3 500–800 (p,n)

Calculations for the (p,n) reaction are shown in Figs. 3.14–3.15, for ^{12}C(p,n) at 800 and 500 MeV and lab angles 9° and 18.5°, respectively. The calculations follow the model of section 3.B.3 with the (p,n) Q value of 18.1 MeV simply added to the ω values to compare with experiment. Three calculations are shown: nonrelativistic (solid curve); relativistic with pseudoscalar coupling for the P invariant (dotted curve) and relativistic with pseudovector coupling (dashed).

Preliminary Los Alamos cross sections [Je85] are shown with the 800 MeV set. Of the two relativistic calculations, the normalization is better matched by the pseudoscalar coupling model, but as with (p,p′) scattering, a better handle on the distortions leading to proper normalization is needed. Assuming that the same distortions apply to (p,p′) and (p,n) scattering, having absolute cross sections for both reactions at a given angle would give the common normalization factor and then the coupling choices could be better compared with experiment.

Of the spin observables, the (p,n) spin transfers most sensitive to the model choices are now D_{nn} and $D_{s's}$, for which the difference in the predictions is very large.

3.D Test of Fermi Gas Model

All of our calculations have been based on a local Fermi gas approximation. To test this we make an improved local density approximation. In the calculation of Section 3.B, effective parameters are obtained by averaging over local values in the nucleus *first*. Another approach to the calculation would be to perform this averaging afterward, that is, calculating the scattering observables for the *local* Fermi gas parameters and then averaging these over the nuclear volume. This calculation proceeds as follows:

Define local values of k_F, M_1 and M_2 by:

$$k_F(r) = \left(\frac{3}{2}\pi^2 \rho_B(r)\right)^{\frac{1}{3}} \qquad (3.D.1a)$$

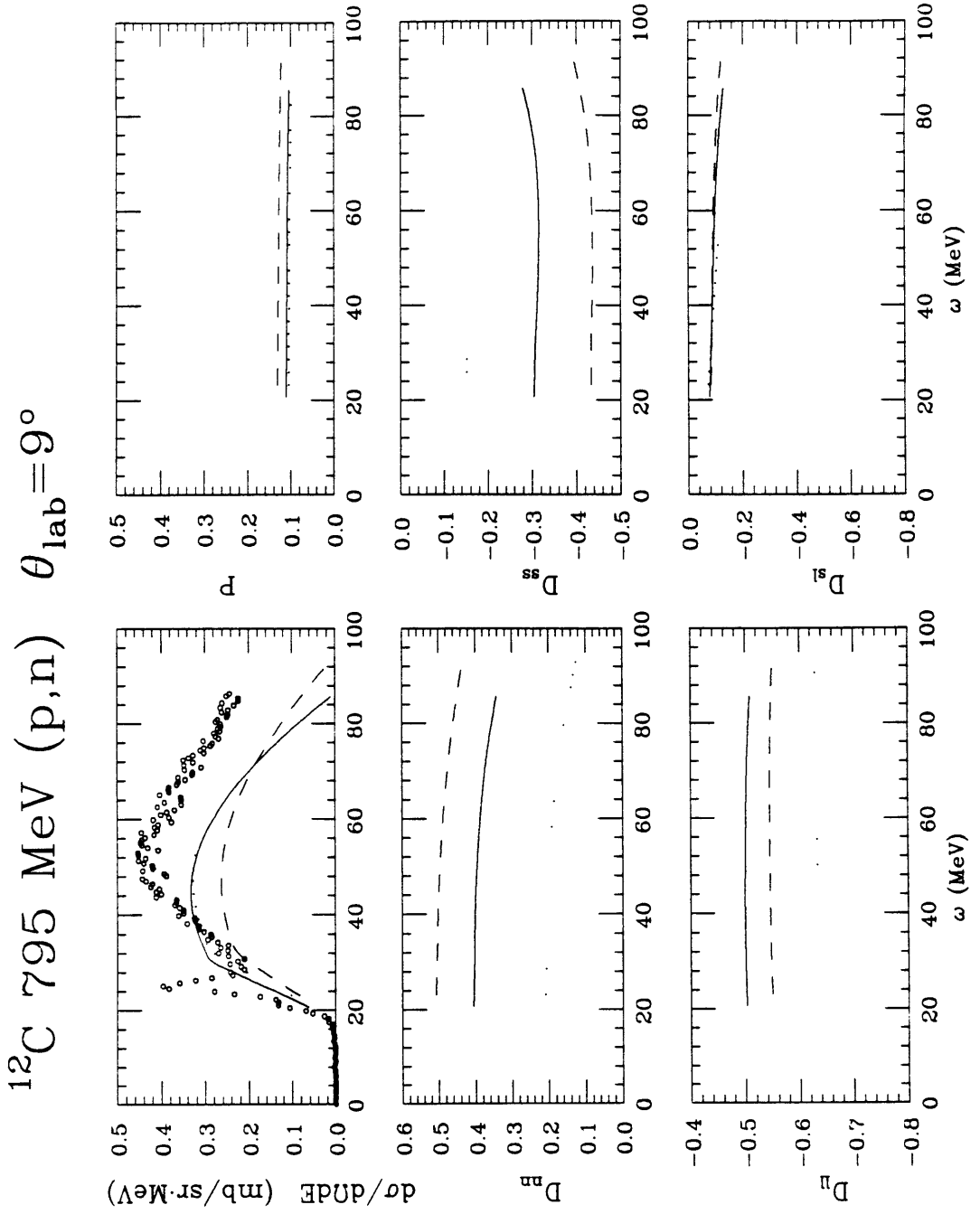

Fig. 3.14 Cross section and spin observables for (p,n) scattering on ^{12}C at 795 MeV at $\theta_{lab} = 9°$. The solid curve uses $M_1 = M_2 = M$. The dotted curve uses relativistic M's with pseudoscalar coupling. The dashed curve uses relativistic M's with pseudovector coupling. Data are from Ref. [Je85].

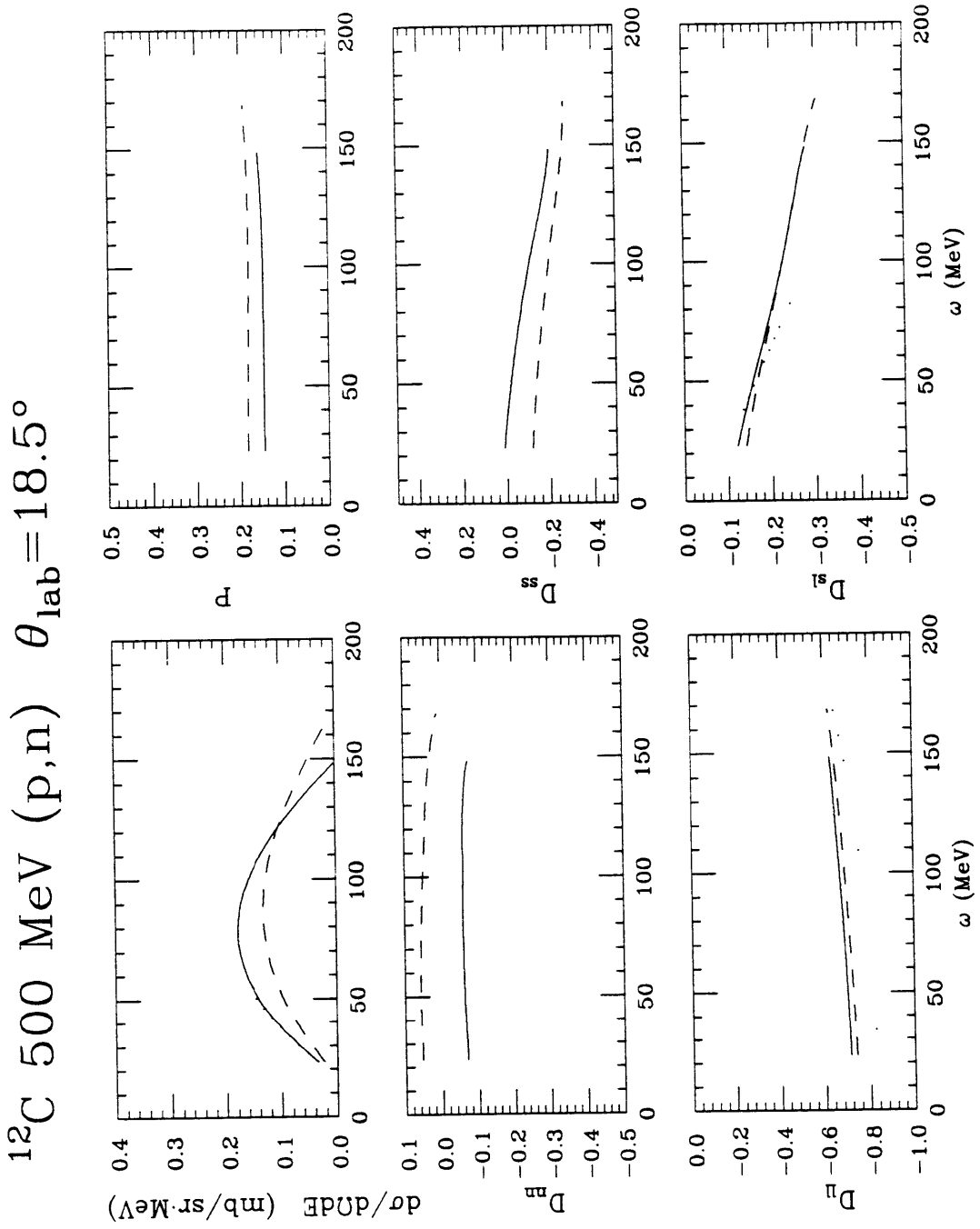

Fig. 3.15 Same as Fig. 3.14 but for (p,n) scattering on ^{12}C at 500 MeV and $\theta_{\rm lab} = 18.5°$.

$$M_1(r) = M - S(r) \qquad M_2(r) = M - .44\frac{\rho(r)}{\rho_0} \qquad (3.D.1b)$$

We use these values in Eqs. (3.B.10) and (3.B.22) to get local cross sections and then average the result:

$$\frac{d^3\overline{\sigma}}{d\Omega_1' dE_1'} = \int b\,db \int dz\, T(b) \Big\{ \rho_p(r) \frac{d^3\overline{\sigma}}{d\Omega_1' dE_1'} \Big(pp, M_1(r), M_2(r), k_F(r) \Big) + \rho_n(r) \frac{d^3\overline{\sigma}}{d\Omega_1' dE_1'} \Big(pn, M_1(r), M_2(r), k_F(r) \Big) \Big\} . \qquad (3.D.2)$$

The spin observables are calculated in a similar fashion.

Calculations using both averaging schemes are compared in Fig. 3.14 for 800 MeV proton scattering on ^{40}Ca at $\theta_{\rm lab} = 20°$. The dashed curves are calculated using Eqs. (3.D.1) and (3.D.2). The solid curves are the corresponding nonrelativistic calculation, using $M_1 = M_2 = M$ in place of (3.1b).

Comparing these results to the data and the calculation of Section 3.B (the dash–dot and dotted curves in Fig. 3.14), the cross section is too sharply peaked, and there is a change in the shapes of the spin observables. This averaging scheme then gives too much of a contribution from the low–density nuclear surface, indicating that the surface response is of some importance and that one must use care in adapting Fermi gas models to a finite nucleus. But we conclude that the uncertainties in using a Fermi gas model do not obscure the difference between relativistic and nonrelativistic calculations of quasielastic spin observables.

3.E Conclusion

In this chapter, models for quasielastic (p,p′) and (p,n) scattering have been presented. These models enable one to calculate cross sections and spin observables as a function of energy loss ω by using a relativistic plane wave impulse approximation in combination with a Fermi gas model for the nuclear target. It is seen that the use of relativistic wavefunctions does have a significant effect on predictions of some

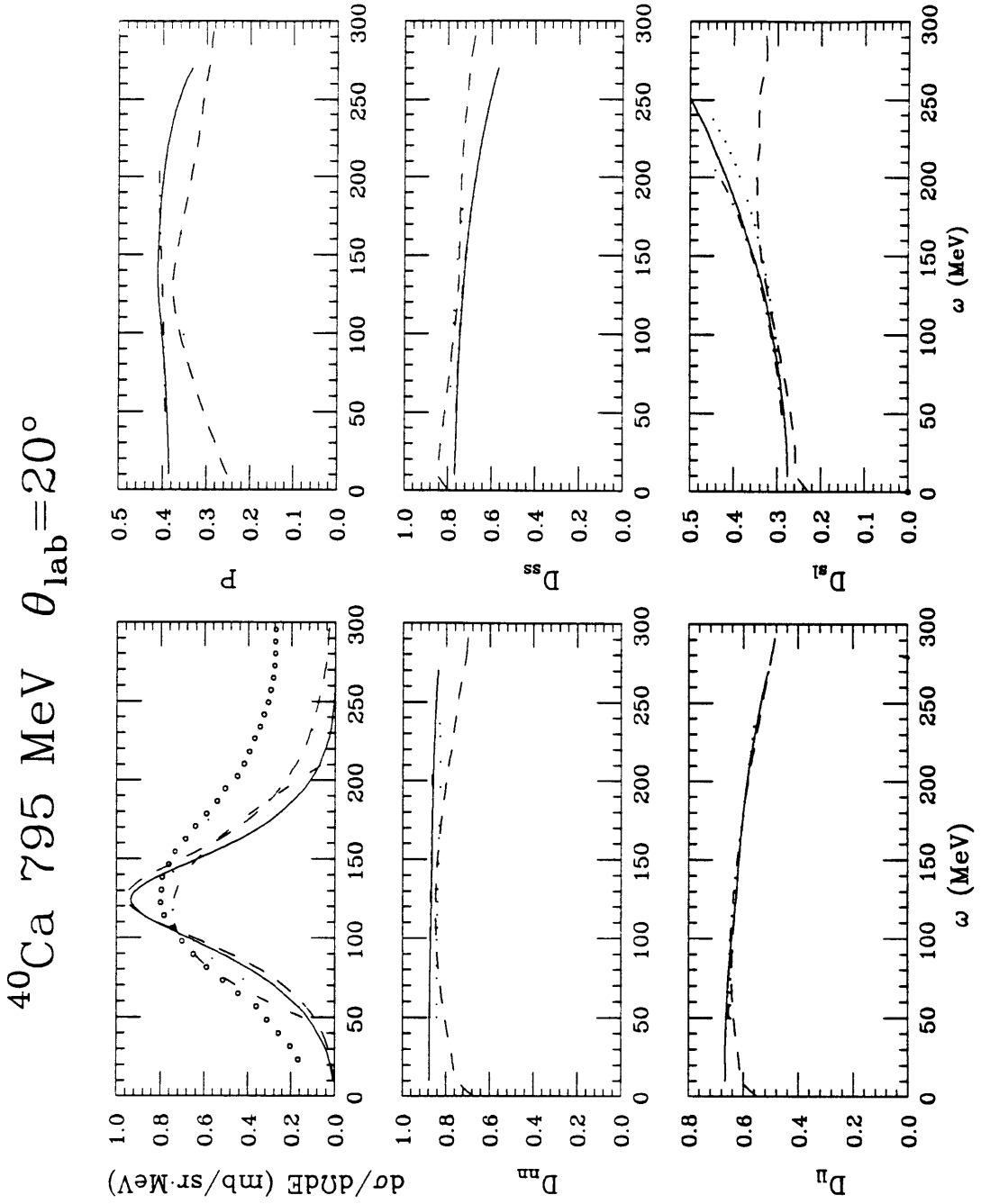

Fig. 3.16 Observables for (p,p') scattering on ^{40}Ca at 795 MeV and $\theta_{\rm lab} = 20°$. The dash-dot and dotted curves are the nonrelativistic and relativistic calculations using effective parameters as described in Section 3.B. The solid and dashed curves are nonrelativistic and relativistic calculations using the local density averaging scheme of Section 3.D, Eq. (3.D.2)

spin observables. The particular observables most affected depends on the lab energy, scattering angle and whether the reaction considered is (p,p′) or (p,n).

Comparison with the rather small amount of available data (without considering $\mathbf{L} \cdot \mathbf{S}$) gives mixed but encouraging results for relativistic models. Cross sections are reasonably well reproduced except for the overall normalization. For 500 MeV (p,p′), the relativistic model predicts a polarization P in agreement with an observed decrease from the nonrelativistic value, but worsens the agreement with $D_{s's}$ and $D_{l'l}$. Similar results are seen at 420 MeV with ^{12}C.

For other lab energies and scattering angles, other spin observables present themselves as good tests for relativistic dynamics. At lower energies and for the (p,n) reaction, the model predicts large differences in some of the spin observables which may provide very clear comparisons of relativistic and nonrelativistic models. In the (p,n) case, one may also be able to distinguish between choices for the coupling of the pion (pseudoscalar invariant amplitude).

The work in this chapter represents only the first pass for a relativistic (p,p′) quasielastic calculation; much more theoretical work needs to be done. Most important for the central result will be the inclusion of spin-orbit distortions which are estimated to improve the overall agreement with the data but which must be incorporated into the full calculation before an unambiguous comparison with experiment can be made. It will also be useful to have a relativistic surface response theory so that surface corrections may be applied to simple target models. It is hoped that such a correction can improve the calculation of this model at low values of the energy loss ω. Better yet, full relativistic DWIA calculations should be done to confirm all the approximations for the target made here.

Finally, more experimental data are needed to map out the behavior of the spin observables over a wide range of energies and scattering angles to compare with the theoretical predictions for these trends. Charge exchange (p,n) spin observable data are

needed to compare with theoretical predictions; absolute (p,n) cross sections would be useful for eliminating the uncertainty in distortions (normalization) for the (p,n) cross sections.

Acknowledgements:

Ken Hicks and Otto Hausser of TRIUMF are thanked for providing preliminary data for 420 MeV $^{12}C(p,p')$ scattering.

Chapter 4. Relativity and Nuclear Magnetic Moments

This chapter discusses a short but important calculation which helped to remove a long-standing objection to relativistic descriptions of nuclear structure, for example the Hartree calculations for finite nuclei used to describe the target nucleus in proton scattering.

4.A Dudley's Dilemma

Relativistic Hartree studies of closed–shell nuclei ([Ho81], [Se86]) give good descriptions of the spin-orbit splittings of the nucleon levels and charge densities. Following this success, it is natural to ask if the relativistic description could do as well as the nonrelativistic theory in predicting the magnetic moments of "closed–shell–plus–one" nuclei, for which the "Schmidt" values agree well with experiment.

Consider a nucleus which has one additional (or less) nucleon from a double–closed–shell configuration, e.g. ^{39}Ca or ^{209}Bi. The additional nucleon is in a level with angular momentum quantum number j. In the extreme single-particle model, the magnetic moment of the nucleus is just that of the last nucleon.

4.A.1 Nonrelativistic Formula

In nonrelativistic theory, the magnetic moment operator is a sum of orbit and spin parts:

$$M_z = \mu_0 (g_k^{(l)} l_z + g_k^{(s)} s_z) \qquad (4.A.1)$$

			Relativistic		
Nucleus	Orbital	Schmidt	No Backflow	Backflow	Expt
^{15}N	$1p_{\frac{1}{2}}$	-.26	0.02	-.12	-.28
^{15}O	$1p_{\frac{1}{2}}$	0.64	0.67	0.52	0.72
^{17}F	$2d_{\frac{5}{2}}$	4.79	5.05	4.92	4.72
^{17}O	$2d_{\frac{5}{2}}$	-1.91	-1.91	-2.05	-1.89
^{39}K	$1d_{\frac{3}{2}}$	0.13	0.86	0.50	0.39
^{39}Ca	$1d_{\frac{3}{2}}$	1.15	1.17	0.81	1.02
^{41}Sc	$1f_{\frac{7}{2}}$	5.79	6.40	6.10	5.43
^{41}Ca	$1f_{\frac{7}{2}}$	-1.91	-1.91	-2.23	-1.60
^{89}Y	$2p_{\frac{1}{2}}$	-.26	0.08	-.09	-.14
^{91}Zr	$2d_{\frac{5}{2}}$	-1.91	-1.90	-2.17	-1.30
^{207}Pb	$3p_{\frac{1}{2}}$	0.64	0.67	0.53	0.59
^{209}Bi	$1h_{\frac{9}{2}}$	2.62	5.07	3.90	4.08

Table 4.1

where

$$g_k^{(l)} = \begin{cases} 1 & \text{proton} \\ 0 & \text{neutron} \end{cases} \qquad \text{and} \qquad g_k^{(s)} = \begin{cases} +5.5858 & \text{proton} \\ -3.8263 & \text{neutron} \end{cases}$$

The magnetic moment (in units of nuclear magnetons) is then the matrix element of this operator for the odd nucleon wavefunction with $m = j$:

$$\begin{aligned} \mu_z &= \frac{1}{\mu_0}\langle\psi_{j,j}|M_z|\psi_{j,j}\rangle \\ &= \begin{cases} (j-1)g_k^{(l)} + \mu_{\mathrm{p,n}} & j = l + \frac{1}{2} \quad \text{(Parallel)} \\ \frac{j}{j+1}\left[(j+\frac{3}{2})g_k^{(l)} - \mu_{\mathrm{p,n}}\right] & j = l - \frac{1}{2} \quad \text{(Anti - parallel)} \end{cases} \end{aligned} \tag{4.A.2}$$

where $\mu_0 = \frac{e\hbar}{2M_pc}$ and $\mu_{\mathrm{p,n}} = \frac{1}{2}g_{\mathrm{p,n}}^{(s)}$. These "Schmidt" magnetic moments agree well with experiment; see Table 4.1.

4.A.2 Relativistic Formula

When relativistic dynamics and wavefunctions are used, there is a different result. With a single-particle wavefunction of the odd nucleon given by

$$\psi_{n\kappa m} = \begin{pmatrix} \frac{iG_{n\kappa}}{r}\Phi_{\kappa m} \\ -\frac{F_{n\kappa}}{r}\Phi_{\kappa m} \end{pmatrix}$$

we get (see Appendix E):

$$\begin{aligned}
\mu_z &= \frac{1}{\mu_0}\langle\psi_{j,j}|M_z|\psi_{j,j}\rangle \\
&= \omega\left(\frac{1+\tau_3}{2}\right)\left(\frac{2j+1}{2j+2}\right)\frac{M_p c}{\hbar}\int_0^\infty rF_{n\kappa}(r)G_{n\kappa}(r)\,dr \\
&- \omega\lambda\left(\frac{j}{j+1}\right)^{\frac{1}{2}}\left[\left(\frac{j}{j+1}\right)^{\frac{\omega}{2}}\int_0^\infty |G_{n\kappa}(r)|^2\,dr + \left(\frac{j}{j+1}\right)^{-\frac{\omega}{2}}\int |F_{n\kappa}(r)|^2\,dr\right]
\end{aligned}$$

$$\text{where} \quad \omega = \begin{cases} -1, & \text{Parallel} \\ +1, & \text{Anti-parallel} \end{cases} \quad \text{and} \quad \lambda = \begin{cases} 1.7928 & \text{odd proton} \\ -1.931 & \text{odd neutron} \end{cases} \tag{4.A.3}$$

So in the relativistic case, we need to have the radial wavefunctions to calculate μ_z. As a first guess, one might suppose that the odd nucleon moves through the mean fields of an undisturbed core; then we can use the mean fields of the Hartree calculation of [Ho81] and find the single–particle solution for the last orbital. Using the resulting radial functions $G_{n\kappa}(r)$ and $F_{n\kappa}(r)$ to calculate μ_z with (4.A.3), the results are listed in Table 4.1 in the column labelled "No Backflow". In general, the agreement with experiment has gotten much worse.

The physical reason for this change is somewhat obscured by the full expression in (4.A.3). The first term arises from the electromagnetic current, which is the expectation value of the operator $\frac{e}{2}(1+\tau_3)\vec{\alpha}$, the charge times the Dirac velocity operator (see Appendix E). For spinors of momentum $\mathbf{k}$ *in the presence of a mean scalar field yielding an effective mass* M^*, this is

$$\mathbf{j}_{\mathrm{EM}} = e\left(\frac{1+\tau_3}{2}\right)\mathbf{v} = e\left(\frac{1+\tau_3}{2}\right)\frac{\mathbf{k}}{\sqrt{\mathbf{k}^2+M^{*2}}}\,. \tag{4.A.4}$$

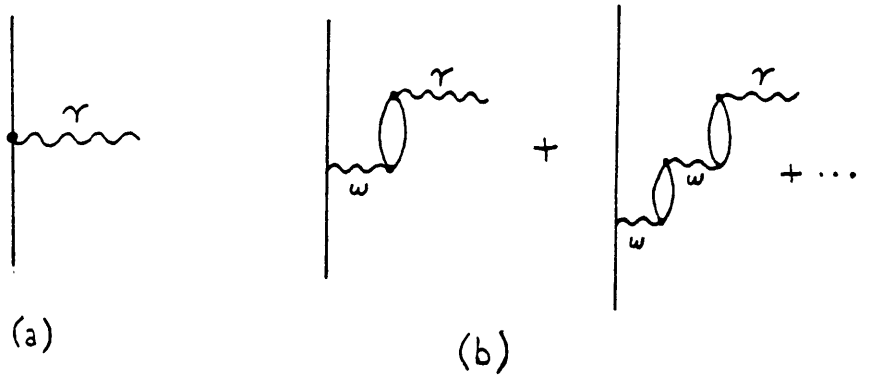

Fig. 4.1 Nucleon–core interactions contributing to the quasiparticle current.

Since M^* in the nuclear medium can be of order $M/2$, the convection current is significantly enhanced from its free value. Thus, the strong nuclear scalar field which gives a spin-orbit interaction consistent with that observed in finite nuclei drives magnetic moments away from their observed values. This inconsistency ("Dudley's Dilemma") was noted by Miller [Mi75].

4.B Quasi–Particle Current

Eq.(4.A.3) for the magnetic moment neglects the interaction between the valence nucleon and the core. But in QHD-I —the model field theory underlying the nuclear structure calculation which we are testing— the photon probe and the valence nucleon can both couple to Lorentz vector, isoscalar excitations of the nuclear medium. Or, put another way, the repulsive vector interaction pushes the core nucleons to give rise to a new vector, isoscalar current (a "backflow" current). In diagrams, the interaction depicted in Fig. 4.1b must be included in the total electromagnetic current.

One must find how the *total* electromagnetic current of the nuclear system reacts to the addition of the valence particle. In 1981 Matsui [Ma81] calculated the resulting total baryon current resulting the removal (or addition) of a particle from nuclear matter. This calculation uses the approach of Landau Fermi liquid theory. It is self-consistent,

so that the backflow is now taken into account. In the nuclear matter rest frame, the *quasi*particle baryon current for the addition of a particle to momentum state $\mathbf{k}_i$ is:

$$\tilde{\mathbf{j}}_i \equiv \frac{\delta \mathbf{j}_B}{\delta n_i} = \frac{\mathbf{k}_i}{(\mathbf{k}_i^2 + M^{*2})^{\frac{1}{2}}} \frac{1}{1+\alpha} \qquad (4.B.1)$$

where

$$\alpha = \frac{2}{3\pi^2} \frac{\frac{g_\omega^2}{m_\omega^2} k_F^3}{(k_F^2 + M^{*2})^{\frac{1}{2}}} \qquad (4.B.2)$$

(4.B.1) shows that the baryon current, enhanced by the low value of M^* is now suppressed by the backflow effect.

Eq.(4.B.1) may also be derived from the relativistic random phase approximation (RRPA). To complete the discussion of the quasiparticle current, one can also show that it is indeed the current that couples to the electromagnetic field. See Ref. [McN86].

4.C Local Density Approximation

To make a simple test of the backflow correction in finite nuclei, we make a local density approximation to incorporate (4.B.1) into (4.A.3). We multiply the isoscalar part of the Dirac moment by the suppression factor in (4.B.1). Thus, for the backflow–corrected magnetic moment in finite nuclei, we use:

$$\begin{aligned}
\mu_z &= \frac{M_z}{\mu_0} \\
&= \frac{\omega}{2}\left(\frac{2j+1}{2j+2}\right)\frac{M_p c}{\hbar}\int_0^\infty \left(\frac{1}{(1+\alpha(r))} + \tau_3\right) r F_{n\kappa}(r) G_{n\kappa}(r)\, dr \\
&- \omega\lambda\left(\frac{j}{j+1}\right)^{\frac{1}{2}}\left[\left(\frac{j}{j+1}\right)^{\frac{\omega}{2}}\int_0^\infty |G_{n\kappa}(r)|^2\, dr + \left(\frac{j}{j+1}\right)^{-\frac{\omega}{2}}\int |F_{n\kappa}(r)|^2\, dr\right]
\end{aligned}$$

$$\text{where} \quad \omega = \begin{cases} -1, & \text{Parallel} \\ +1, & \text{Anti-parallel} \end{cases} \quad \text{and} \quad \lambda = \begin{cases} 1.7928 & \text{odd proton} \\ -1.931 & \text{odd neutron} \end{cases} \qquad (4.C.1)$$

where now $\alpha(r)$ is given its local value:

$$\alpha(r) \equiv \frac{2}{3\pi^2} \frac{\frac{g_V^2}{m_V^2} k_F^3(r)}{(k_F^2(r) + M^*(r)^2)^{\frac{1}{2}}} \qquad (4.C.2)$$

			Relativistic		
Nucleus	Orbital	Schmidt	No Backflow	Backflow	Expt.
^{15}N+^{15}O	$1p_{\frac{1}{2}}$	0.38	0.67	0.40	0.44
^{17}F+^{17}O	$1d_{\frac{5}{2}}$	2.88	3.14	2.87	2.83
^{39}K+^{39}Ca	$1d_{\frac{3}{2}}$	1.28	2.03	1.31	1.41
^{41}Sc+^{41}Ca	$1f_{\frac{7}{2}}$	3.88	4.49	3.87	3.83

Table 4.2

with

$$k_F(r) \equiv \left(\frac{3\pi^2}{2}\rho_B(r)\right)^{\frac{1}{3}} \qquad \text{and} \qquad M^*(r) \equiv M - g_S\phi(r)\ . \qquad (4.C.3)$$

ρ_B, and $\phi(r)$ are taken from the Hartree calculation of [Ho81] for the core nucleus, which is either ^{16}O, ^{40}Ca, ^{90}Zr or ^{208}Pb.

The results are shown in Table 4.1 under "Backflow". Generally the agreement with experiment (and the Schmidt values) is improved.

Note however that the backflow correction is only for the isoscalar current. There will be no correction for the isovector current in the QHD-I model, but *both* currents were enhanced by the small relativistic effective mass in (4.A.4). So it is more sensible to compare the isoscalar moments (the sum of odd proton and odd neutron values) to the Schmidt values and experiment. These are listed in Table 4.2, where it is seen that the relativistic values with backflow are now very close to the Schmidt values.

Static magnetic moments are thus *not* an obvious problem for relativistic treatments of nuclear structure as was once supposed, but it is necessary to go beyond the independent particle model and include the interaction with the nuclear core.

Though both relativistic and nonrelativistic calculations now give essentially the same results for isoscalar moments, it is important to note that they come about in different ways; for the nonrelativistic calculation, the current for the valence nucleon

gives a magnetic moment in agreement with experiment. In the relativistic case, one must look at its *quasi*particle current. The nucleon behaves as a particle of mass M^*, but this effect just happens to be cancelled out by the interaction with the core. This is not surprising when one considers that in relativistic models, the strongly attractive scalar potential is similarly cancelled by the strongly repulsive vector potential to give the relatively weak binding energy of nuclear matter. One simply concludes that static magnetic moments are not a very sensitive test for differences between relativistic and nonrelativstic theories of nuclear structure.

References

Ab72 M. Abramowitz and I. Stegun, eds., *Handbook of Mathematical Functions*, Dover Publications, New York (1972)

Ad84 D. L. Adams and M. Bleszynski, *Phys Lett.* **136B**, 10 (1984)

Am83 R. Amado et al., *Phys. Rev.* **C31**, 1340 (1983)

Ar82 R. A. Arndt and D. Roper, VPI and SU Scattering Analysis Interactive Dial-In Program and Data Base

Au70 N. Austern, *Direct Nuclear Reaction Theories*, Wiley, New York, 1970

Ba84 W. Bauhoff, Phys. Rev. **C30**, 1113 (1984)

Ba85 W. Bauhoff, private communication and in *Medium Energy Nucleon and Antinucleon Scattering*, Bad Honnef, West Germany, June 1985, edited by H. V. von Geramb, Springer–Verlag 1985

Bj64 J. D. Bjorken and S. Drell, *Relativistic Quantum Mechanics*, McGraw-Hill, New York, 1964

Ca85 Carey et al, Los Alamos 500 MeV experiment and private communication

Ch80 R. E. Chrien et al, *Phys. Rev.* **C21**, 1014 (1980)

Cl83a B. C. Clark, S. Hama and R. L. Mercer in *The Interaction Between Medium Energy Nucleons in Nuclei–1982*, Proceedings of the Workshop of the Interaction Between Medium Energy Nucleons in Nuclei, AIP Conf. Proc. No. 97, edited by H. O. Meyer, AIP, New York, 1983

Cl83b B. C. Clark, S. Hama, R. L. Mercer, L. Ray, and B. D. Serot, *Phys. Rev. Lett.*, **50**, 1644 (1983)

Cl83c B. C. Clark et al, *Phys. Rev. Lett.* **51**, 1808 (1983)

Co87 E. D. Cooper and B. Jennings, *Nucl. Phys.* **A458**, 717 (1986)

Dr85 T. Drake in *Medium Energy Nucleon and Antinucleon Scattering*, edited by H. V. von Geramb, Bad Honnef, West Germany 1985, Springer–Verlag

Es84 H. Esbensen and G. Bertsch, *Ann. Phys. (N.Y.)* **157**, 255 (1984)

Gl83 W. Glöckle, *The Quantum Mechanical Few–Body Problem*, Springer–Verlag Berlin 1983

Hi87 K. Hicks, private communicaton; TRIUMF data, to be published

Ha85 O. Hausser et al., to be published

Ho72 K. Holinde, K. Erkelenz and R. Alzetta, *Nucl. Phys.* **A194**, 161 (1972)

Ho81 C. J. Horowitz and B. D. Serot, *Nucl. Phys.* **A368**, 503 (1981)

Ho84 C.J. Horowitz and B. D. Serot, *Phys. Lett.* **140B**, 181 (1984)

Ho85 C. J. Horowitz, *Phys. Rev.* **C31**, 1340 (1985)

Ho86 C. J. Horowitz and M. J. Iqbal, *Phys. Rev.* **C33**, 2059 (1986)

Ho87 C. J. Horowitz and B. D. Serot, *Nucl. Phys.* **464A**, 613 (1987)

Hu81a D. A. Hutcheon et al., *Polarization Phenomena in Nuclear Physics*, G. G. Ohlsen, ed., (1980) (AIP,1981)

Hu81b D. A. Hutcheon et al., Phys. Rev. Lett. **47**, 315 (1981)

Ke59 A. Kerman, H. McManus and R. Thaler, *Ann. Phys.* (N.Y.) **8**, 551 (1959)

Je85 R. Jeppesen, Doctoral Thesis, University of Colorado, 1985

Ko85 A. M. Kobos, E. D. Cooper, J. I. Johansson and H. S. Sherif, *Nucl. Phys.* **A445**, 605 (1985)
Ko86 Koonin, Steven, *Computational Physics*, W. A. Benjamin, Reading MA, 1986
Lu87 J. D. Lumpe and L. Ray, *Phys. Rev.* **C35**, 1040 (1987)
Ma40 Margenau, *Phys. Rev.* **57**, 383 (1940)
Ma91 T. Matsui, *Nucl. Phys.* **A370**, 365 (1981)
McC68 I. E. McCarthy, *Introduction to Nuclear Theory*, John Wiley and Sons, New York, 1968
McN83a J. A. McNeil, L. Ray and S. J. Wallace, *Phys. Rev.* **C27**, 2123 (1983)
McN83b J. A. McNeil, J. R. Shepard and S. J. Wallace, *Phys. Rev. Lett.* **50**, 1439 (1983)
McN86 J. A. McNeil et al., *Resolution of the Magnetic Moment Problem in Relativistic Theories*, Univ. of Pennsylvania preprint; also, talk presented at *Second Conference on the Interaction Between Particle and Nuclear Physics*, May 26-31 1986, Lake Louise, Canada
Mi86 C. A. Miller et al, Phys. Lett. **169B**, 166 (1986)
Mi75 L. D. Miller, *Ann. Phys.* **91**, 40 (1975)
Mu87 D. P. Murdock and C. J. Horowitz, *Phys. Rev.* **C35**, 1442 (1987)
Ne72 J. W. Negele and D. Vautherin, *Phys. Rev.* **C5**, 1472 (1972)
Ra85 L. Ray and G. W. Hoffman, *Phys. Rev.* **C31**, 538 (1985)
Ri85 L. Rikus and H.V. von Geramb, *Nucl. Phys.* **A426**, 496 (1984)
Ro80 R. Rosenfelder, *Ann. Phys. (N.Y.)* **128**, 188 (1980)
Sc82 P. Schwandt et al, *Phys. Rev.* **C26**, 55 (1982)
Se86 B. D. Serot and J. D. Walecka, *The Relativistic Nuclear Many-Body Problem* in *Advances in Nuclear Physics* Vol. 16, ed. by Negele and Vogt, Plenum Press, New York, 1986
Sh83 J. R. Shepard, J. A. McNeil and S. J. Wallace, *Phys. Rev. Lett.* **50**, 1443 (1983)
Sm85 R. D. Smith and S. J. Wallace, *Phys. Rev.* **C32**, 1654 (1985)
Sm86 R. Smith, preprint and priv. comm.
St85 E. J. Stephenson in *Antinucleon– and Nucleon–Nucleus Interactions*, Telluride, Colorado, March 1985, edited by G. E. Walker et al, Plenum Press 1985
Ta72 J. R. Taylor, *Scattering Theory*, John Wiley and Sons Inc., New York, 1972
Th85 M. Thies, *Phys. Lett.* **162B**, 255 (1985)
Tj85 J. A. Tjon and S. J. Wallace, *Phys. Rev.* **C32**, 1667 (1985)
Wa74 J. D. Walecka, *Ann. Phys. (N.Y.)*, **83**, 491 (1974)
Wa85 S. J. Wallace, *Proceedings of the LAMPF Workshop on Dirac Appraoches to Nuclear Physics*, edited by J. R. Shepard, C. Y. Cheung and R. L. Boudrie, LA 10438–C

Appendix A. Transformation of NN Amplitudes; The MRW Matrix

The relativistic impulse approximation uses information from NN scattering to construct the (relativistic) N–nucleus optical potential. In Ref. [McN83a] (to be referred to as MRW) this information is cast in a Lorentz–invariant form so that quantities in the NN center of mass frame can be taken over to any other frame, e.g. the N–nucleus center of mass frame.

In the center of mass frame for the NN collision, the incoming nucleons have momenta and spins $\mathbf{k}_c$, s_1 and $-\mathbf{k}_c$, s_2. The outgoing nucleons have momenta and spins $\mathbf{k}'_c$, s'_1 and $-\mathbf{k}'_c$, s'_2. As in MRW, define $\mathbf{q} = \mathbf{k}_c - \mathbf{k}'_c$ and $\mathbf{k}_a = \frac{1}{2}(\mathbf{k}_c + \mathbf{k}'_c)$; then a mutually orthogonal set of unit vectors is $\hat{q}$, $\hat{k}_a \equiv \hat{z}$ and $\hat{n} \equiv \hat{q} \times \hat{z}$. The vector $\hat{n}$ is perpendicular to the scattering plane: $\mathbf{k}'_c \times \mathbf{k}_c = -k_a q \hat{n}$.

The NN scattering amplitude (in its nonrelativistic representation, a matrix in the Pauli spin–space of the two interacting nucleons) is parametrized so as to satisfy isospin, parity and time–reversal invariance. One representation is [Gl83],[Ar82]:

$$M(\mathbf{k},\mathbf{k}') = a + c(\vec{\sigma}_1\cdot\hat{n} + \vec{\sigma}_2\cdot\hat{n}) + m(\vec{\sigma}_1\cdot\hat{n}\vec{\sigma}_2\cdot\hat{n}) + (g+h)(\vec{\sigma}_1\cdot\hat{z}\vec{\sigma}_2\cdot\hat{z}) + (g-h)(\vec{\sigma}_1\cdot\hat{q}\vec{\sigma}_2\cdot\hat{q}) \ , \tag{A.1}$$

normalized so that the absolute value squared of a matrix element of (A.1) gives the cross section. a,....,h are complex quantities depending on the energy of the collision and the scattering angle.

Using

$$\vec{\sigma}_1 \cdot \vec{\sigma}_2 = \vec{\sigma}_1 \cdot \hat{n}\vec{\sigma}_2 \cdot \hat{n} + \vec{\sigma}_1 \cdot \hat{z}\vec{\sigma}_2 \cdot \hat{z} + \vec{\sigma}_1 \cdot \hat{q}\vec{\sigma}_2 \cdot \hat{q} \ , \tag{A.2}$$

other representations are possible for M. MRW write:

$$\begin{aligned}(2ik_c)^{-1}M &\equiv (2ik_c)^{-1}f_c \\ &\equiv A + B\vec{\sigma}_1 \cdot \vec{\sigma}_2 + iqC(\vec{\sigma}_1 \cdot \hat{n} + \vec{\sigma}_2 \cdot \hat{n}) + D\vec{\sigma}_1 \cdot \hat{q}\vec{\sigma}_2 \cdot \hat{q} + E\vec{\sigma}_1 \cdot \hat{z}\vec{\sigma}_2 \cdot \hat{z}\end{aligned} \tag{A.3}$$

In a similar way one can use *Dirac* spinor language for the nucleons to construct a relativistic NN amplitude. In place of f_c we will use $(2ik_c)\hat{\mathcal{F}}$, a matrix in the Dirac spinor space of the two nucleons, a $4 \times 4 \otimes 4 \times 4$ matrix with 256 components, which similarly depends on E_c and $q = |\mathbf{q}|$. Its relation to f_c is the following:

$$(2ik_c)^{-1}\chi^\dagger_{s_1'}\chi^\dagger_{s_2'}f_c(E_c,q)\chi_{s_1}\chi_{s_2} = \overline{U}(\mathbf{k}_c',s_1')\overline{U}(-\mathbf{k}_c',s_2')\hat{\mathcal{F}}(E_c,q)U(\mathbf{k}_c,s_1)U(-\mathbf{k}_c,s_2) \tag{A.4}$$

where the χ's are *Pauli* spinors for the different spin orientations and the U's are Dirac 4–component positive–energy spinors, normalized so that $\overline{U}U = 1$.

The information from NN scattering experiments which determines the 5 independent components of f_c will determine only a small number of the components of $\hat{\mathcal{F}}$, so without further theoretical input, some assumptions must be made about the form of $\hat{\mathcal{F}}$. The original choice for $\hat{\mathcal{F}}$ was

$$\hat{\mathcal{F}}(E_c) = \sum_L F^L(E_c,q)\lambda^L_{(1)} \cdot \lambda^L_{(2)} \tag{A.5}$$

where the L's stand for the Dirac matrix types given in Table 1.2 (see the discussion in the main text). The amplitude with this choice is a sum of five terms,

$$\begin{aligned}(2ik_c)^{-1}M = {} & F^S\overline{U}_{1'}U_1\,\overline{U}_{2'}U_2 + F^V\overline{U}_{1'}\gamma^\mu U_1\,\overline{U}_{2'}\gamma_\mu U_2 + F^T\overline{U}_{1'}\sigma^{\mu\nu}U_1\,\overline{U}_{2'}\sigma_{\mu\nu}U_2 \\ & + F^A\overline{U}_{1'}\gamma^5\gamma^\mu U_1\,\overline{U}_{2'}\gamma^5\gamma_\mu U_1 + F^P\overline{U}_{1'}\gamma^5 U_1\,\overline{U}_{2'}\gamma^5 U_2\end{aligned} \tag{A.6}$$

From the Lorentz invariance of the amplitude and of the bilinear combinations, each of the F^L's is a Lorentz–invariant function of the (invariant) quantities E_c and q.

Using the explicit expressions for the Dirac spinors U and the γ matrices, the right hand side of (A.6) can be expanded in terms of the independent set of spin operators and Pauli spinors, and the coefficients can be identified with those on the right hand side of (A.3). In this way, the 5 F^L's and the coefficients $A,\ldots,E$ can be written as linear combinations of one another. Specifically, one can derive a 5×5 matrix

$\mathcal{O}(E_c, k_a, q)$ which gives the MRW (center of mass) Wolfenstein parameters in terms of the F^L invariants:

$$\begin{pmatrix} A \\ B \\ C \\ D \\ E \end{pmatrix} = \begin{pmatrix} & & \\ & \mathcal{O}(E_c, k_a, q) & \\ & & \end{pmatrix} \begin{pmatrix} F^S \\ F^V \\ F^T \\ F^A \\ F^P \end{pmatrix} \tag{A.7}$$

For example, the F^S term of (A.6), omitting the Pauli spinor factors in the *Dirac* spinors, is:

$$F^S \left(\frac{E+M}{2M}\right)^2 \left[1 + \frac{(\vec{\sigma}_2 \cdot \mathbf{k}')(\vec{\sigma}_2 \cdot \mathbf{k})}{(E+M)^2}\right] \left[1 + \frac{(\vec{\sigma}_1 \cdot \mathbf{k}')(\vec{\sigma}_1 \cdot \mathbf{k})}{(E+M)^2}\right] \tag{A.8}$$

Using

$$\vec{\sigma} \cdot \mathbf{k}' \, \vec{\sigma} \cdot \mathbf{k} = \mathbf{k}' \cdot \mathbf{k} + i\vec{\sigma} \cdot (\mathbf{k}' \times \mathbf{k})$$

the definitions of $\mathbf{k}_a$ and $\mathbf{q}$ and with the notation $\sigma_{1n} \equiv \vec{\sigma}_1 \cdot \hat{n}$, this is:

$$\begin{aligned} F^S \left(\frac{E+M}{2M}\right)^2 & \left[1 + \frac{\mathbf{k}_a^2 - \frac{\mathbf{q}^2}{4} - iqk_a\sigma_{2n}}{(E+M)^2}\right] \left[1 + \frac{\mathbf{k}_a^2 - \frac{\mathbf{q}^2}{4} - iqk_a\sigma_{1n}}{(E+M)^2}\right] \\ &= F^S \left(\frac{E+M}{2M}\right)^2 \left\{ \left[1 + \frac{\mathbf{k}_a^2 - \frac{\mathbf{q}^2}{4}}{(E+M)^2}\right] - iqk_a \left[1 + \frac{k_a - \frac{\mathbf{q}^2}{4}}{(E+M)^2}\right] (\sigma_{1n} + \sigma_{2n}) \right. \\ &\qquad \left. - \frac{k_a^2 \mathbf{q}^2}{(E+M)^4} [\vec{\sigma}_1 \cdot \vec{\sigma}_2 - \sigma_{1q}\sigma_{2q} - \sigma_{1z}\sigma_{2z}] \right\} \end{aligned} \tag{A.9}$$

where (A.2) was used in the last step. From this last expression, one can read off the contributions of F^S to A, C, B, D and E respectively, thus giving the first column of the MRW matrix. The other entries are found similarly.

Much of the discussion of MRW deals with finding the NN amplitudes in the "Breit frame", a kinematic prescription which deals with the fact that the other $A-1$ nucleons in the recoiling nucleus carry away some momentum from the NN collision. The Breit frame amplitude has the form

$$(2ik_c)^{-1} M = A + B\vec{\sigma}_1 \cdot \vec{\sigma}_2 + iq(C_1\sigma_{1n} + C_2\sigma_{2n}) + D\sigma_{1q}\sigma_{2q} + E\sigma_{1z}\sigma_{2z} \tag{A.10}$$

with $C_1 \neq C_2$ now from the lack of time–reversal symmetry in this frame. The matrix in (A.7) is a special case of the matrix in Table I of MRW with $A = 1$, which gives $C_1 = C_2$.

Appendix B: Calculation of Scattering Observables

I. Scattering Amplitude

In the first part of this thesis, scattering observables for spin-$\frac{1}{2}$–spin-0 collisions were calculated. This appendix will cover the mathematics and some of the numerical details of the computer code which does this calculation.

We need to describe the scattering of a spin-$\frac{1}{2}$ particle from a nuclear optical potential (within the framework of the Schrödinger equation... see Appendix C). This potential is the sum of two parts: First there is the strong, short-ranged "nuclear" part which is complex and which has a central part (dependent on r only) and spin–orbit part (dependent on r and the spin orientation of the projectile). Second, there is the weak, long–ranged Coulomb potential between the projectile and the nucleus. The spin–orbit potential makes the cross–section dependent on the spin of the projectile and gives rise to the observables A_y and Q. The presence of the Coulomb potential demands special treatment for calculating the scattered wavefunction in the asymptotic region.

The geometry for the scattering experiment is shown in Fig. B.1. The projectile's initial momentum is in the $+z$ direction; the scattering takes place in the $x-z$ plane at spherical angles θ and $\phi = 0$ (ϕ is measured from the x–axis).

We begin by considering a point charge Ze at the origin. For a spin–$\frac{1}{2}$ particle with charge $+e$ and mass μ incident along $+z$ with energy $E = \frac{k^2}{2\mu}$, the solution to the Schrödinger equation satisfying the boundary conditions is:

$$\Psi_c = v^{-\frac{1}{2}} \sum_l [4\pi(2l+1)]^{\frac{1}{2}} i^l e^{i\sigma_l} \frac{F_l(kr)}{kr} Y_l^0(\theta,\phi)[a_{\frac{1}{2}}\alpha + a_{-\frac{1}{2}}\beta] \qquad (B.1)$$

where the Coulomb phase shift σ_l is given by

$$\sigma_l = \arg\Gamma(l+1+i\eta) \qquad (B.2)$$

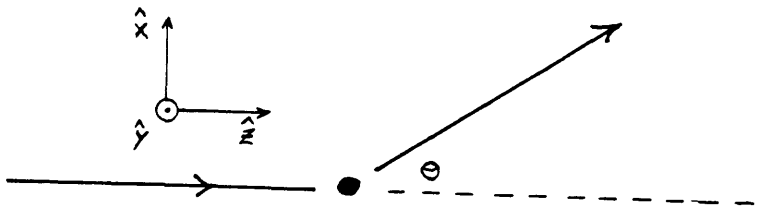

Fig. B.1 Coordinate system for proton–nucleus scattering

with

$$\eta = \frac{\mu Z e^2}{\hbar^2 k^2} \ , \tag{B.3}$$

and the $F_l(kr)$ are the regular Coulomb wavefunctions, described in [Ab72]. α and β denote Pauli spinors for spin up or down in the z–direction. The spin part of the wavefunction has $|a_{\frac{1}{2}}|^2 + |a_{-\frac{1}{2}}|^2 = 1$ and is a trivial factor here since the potential has no spin–dependence.

In general, the continuum solution to the Schrödinger equation for the point charge potential has a linear combination of F_l and the irregular Coulomb function G_l but with the F_l choice in (B.1), Ψ_c goes asymptotically as:

$$\Psi_c \rightarrow v^{-\frac{1}{2}} \left\{ e^{i[kz - \eta \ln k(r-z)]} \left[1 - \frac{\eta^2}{ik(r-z)} \right] + \frac{1}{r} f_c(\theta) e^{i(kr - \eta \ln 2kr)} \right\} (a_{\frac{1}{2}}\alpha + a_{-\frac{1}{2}}\beta) \tag{B.4}$$

with

$$f_c(\theta) = -\frac{\eta}{2k \sin^2 \frac{\theta}{2}} e^{-i\eta \ln(\sin^2 \frac{\theta}{2}) + 2i\sigma_0} \ , \tag{B.5}$$

the Rutherford scattering amplitude. This is the desired asymptotic form since it has only a $\frac{1}{r}e^{+ikr}$ part for an outgoing scattered wave with no incoming radial wave. Also, as $\eta \rightarrow 0$ (limit of zero charge), the F_l's tend to the spherical Bessel functions j_l to give the familiar plane wave expansion which is regular at the origin.

We now generalize (B.1) for a nuclear potential, which tends to a point charge potential at large distances and now depends on the spin orientation of the projectile. First, we write (B.1) in terms of eigenstates of $\mathbf{J}^2$, $\mathbf{L}^2$, $\mathbf{S}^2$ and $\mu = J_z$. These eigenstates are:

$$\mathcal{Y}^{\mu}_{j,l,\frac{1}{2}} = \langle l\ \mu - \tfrac{1}{2}\ \tfrac{1}{2}\ \tfrac{1}{2} | j\ \mu \rangle Y_l^{\mu-\frac{1}{2}}\ \alpha + \langle l\ \mu + \tfrac{1}{2}\ \tfrac{1}{2}\ \tfrac{1}{2} | j\ \mu \rangle Y_l^{\mu+\frac{1}{2}}\ \beta \qquad (B.6)$$

Writing down the four relations of this type with $j = l \pm \frac{1}{2}$ and $\mu = \pm\frac{1}{2}$ and inverting them to substitute for the product of spherical harmonics and spinors, (B.1) can be written as:

$$\Psi_c = \sqrt{\frac{4\pi}{v}} \sum_l i^l e^{i\sigma_l} \frac{F_l(kr)}{kr} \Big\{ \sqrt{l+1}(a_{\frac{1}{2}} \mathcal{Y}^{\frac{1}{2}}_{l+\frac{1}{2},l,\frac{1}{2}} + a_{-\frac{1}{2}} \mathcal{Y}^{-\frac{1}{2}}_{l+\frac{1}{2},l,\frac{1}{2}}) + \sqrt{l}(-a_{\frac{1}{2}} \mathcal{Y}^{\frac{1}{2}}_{l-\frac{1}{2},l,\frac{1}{2}} + a_{-\frac{1}{2}} \mathcal{Y}^{-\frac{1}{2}}_{l-\frac{1}{2},l,\frac{1}{2}}) \Big\} \qquad (B.7)$$

The nuclear spin–orbit potential is proportional to the operator $\mathbf{L} \cdot \mathbf{S}$, which, for eigenfunctions of $\mathbf{J}^2$, $\mathbf{L}^2$ and $\mathbf{S}^2$ can be replaced by:

$$\mathbf{L} \cdot \mathbf{S} = \frac{1}{2}(\mathbf{J}^2 - \mathbf{L}^2 - \mathbf{S}^2) = \frac{\hbar^2}{2}\left(j(j+1) - l(l+1) - \frac{3}{4} \right) \qquad (B.8)$$

Then to generalize (B.7) to a nuclear potential with a spin–orbit part, in place of $F_l(kr)$ we have a general radial wavefunction which will depend on whether $j = l + \frac{1}{2}$ or $j = l - \frac{1}{2}$, denoted respectively by u^+ and u^-. The wavefunction for nuclear scattering is then:

$$\Psi_{Total} = \sqrt{\frac{4\pi}{v}} \sum_l i^l \frac{e^{i\sigma_l}}{kr} \Big\{ \sqrt{l+1} u_l^+(kr) \left(a_{\frac{1}{2}} \mathcal{Y}^{\frac{1}{2}}_{l+\frac{1}{2},l,\frac{1}{2}} + a_{-\frac{1}{2}} \mathcal{Y}^{-\frac{1}{2}}_{l+\frac{1}{2},l,\frac{1}{2}} \right) + \sqrt{l} u_l^-(kr) \left(-a_{\frac{1}{2}} \mathcal{Y}^{\frac{1}{2}}_{l-\frac{1}{2},l,\frac{1}{2}} + a_{-\frac{1}{2}} \mathcal{Y}^{-\frac{1}{2}}_{l-\frac{1}{2},l,\frac{1}{2}} \right) \Big\} \qquad (B.9)$$

with the scattered wave defined by:

$$\Psi_{Total} \equiv \Psi_c + \Psi_{scat} \qquad (B.10)$$

Ψ_{Total} satisfies the Schrödinger equation

$$\left[-\frac{\hbar^2}{2\mu}\nabla^2 + V_c + V_{so}\,\mathbf{L}\cdot\mathbf{S}\right]\Psi_{Total} = E\Psi_{Total}$$

Substituting expansion (B.9) into this and using (B.8) gives the radial Schrödinger equations for $u^{\pm}$:

$$\frac{d^2u_l^{\pm}}{dr^2} + \left\{k^2 - \frac{2\mu}{\hbar^2}\left[V_c + \frac{\hbar^2}{2}\begin{pmatrix} l \\ -l-1 \end{pmatrix} V_{so}\right] - \frac{l(l+1)}{r^2}\right\} u_l^{\pm}(r) = 0 \qquad (B.11)$$

The u_l's differ from the F_l's because of the nuclear strong potential; in the exterior region, where only the Coulomb potential affects the scattering, the u_l's will be some linear combination of F_l *and* G_l because the boundary conditions for the point charge potential do not apply here. So in the exterior region, u_l has the general form:

$$u_l^{\pm}(kr) \underset{r>R}{\sim} \mathcal{A}_l^{\pm}F_l(kr) + \mathcal{B}_l^{\pm}G_l(kr)$$

The combination $G_l(kr) + iF_l(kr)$ goes asymptotically as an outgoing spherical wave:

$$G_l(kr) + iF_l(kr) \underset{r\to\infty}{\sim} \exp[i(kr - \eta\ln 2kr - \frac{l\pi}{2} + \sigma_l)]\ . \qquad (B.12)$$

Similarly, $G_l - iF_l$ tends to an incoming spherical wave. If we now require the total scattered wave to behave asymptotically as a Coulomb wave Ψ_c with an added outgoing spherical wave (as in (B.10)), then the u_l's must have the asymptotic form:

$$u_l^{\pm}(kr) \underset{r>R}{\sim} F_l(kr) + \mathcal{C}_l^{\pm}[G_l(kr) + iF_l(kr)] \qquad (B.13)$$

Without the nuclear strong potential and the finite charge distribution, the $\mathcal{C}_l$'s would vanish, leaving only F_l to give the pure Coulomb wave (B.7). Roughly speaking, experiments can see only outgoing spherical waves so they will be influenced by the second term of (B.13) but also by the part of F_l which has this form; in this way, the

Rutherford (point charge) scattering amplitude shows up in the final results, as will be seen.

Substituting (B.13) into (B.9) gives the form of Ψ_{Total} for large r. The $F_l(kr)$ term in (B.13) gives Ψ_c back again. Using (B.13), we have:

$$\begin{aligned}\Psi_{Total} \underset{r\to\infty}{\sim} \Psi_c + \sqrt{\frac{4\pi}{v}}\sum_l i^l \frac{e^{i\sigma_l}}{kr}\Big\{ &\sqrt{l+1}C_l^+ \exp[i(kr-\eta\ln 2kr-\frac{l\pi}{2}+\sigma_l)] \\ &(a_{\frac{1}{2}}y^{\frac{1}{2}}_{l+\frac{1}{2},l,\frac{1}{2}} + a_{-\frac{1}{2}}y^{-\frac{1}{2}}_{l+\frac{1}{2},l,\frac{1}{2}}) \\ &+\sqrt{l}C_l^- \exp[i(kr-\eta\ln 2kr-\frac{l\pi}{2}+\sigma_l)] \\ &(-a_{\frac{1}{2}}y^{\frac{1}{2}}_{l-\frac{1}{2},l,\frac{1}{2}} + a_{-\frac{1}{2}}y^{-\frac{1}{2}}_{l-\frac{1}{2},l,\frac{1}{2}})\Big\}\end{aligned} \tag{B.14}$$

where the asymptotic form for Ψ_c has already been given by (B.4). Finally, when we put the put the large–r form for Ψ_c into (B.14), re-express the y functions as combinations of the spherical harmonics Y_l^0 and Y_l^1 with Pauli spinors α and β and use

$$Y_l^m = (-1)^m\left[\frac{(2l+1)}{4\pi}\frac{(l-m)!}{(l+m)!}\right]^{\frac{1}{2}} P_l^m(\cos\theta)e^{im\phi}$$

we get:

$$\begin{aligned}\Psi_{Total} \underset{r\to\infty}{\sim} & v^{-\frac{1}{2}}\left\{e^{i[kz-\eta\ln k(r-z)]}\left[1-\frac{\eta^2}{ik(r-z)}\right]\right\}[a_{\frac{1}{2}}\alpha + a_{-\frac{1}{2}}\beta] \\ &+ v^{-\frac{1}{2}}\frac{1}{r}f_c(\theta)e^{i(kr-\ln 2kr)}[a_{\frac{1}{2}}\alpha + a_{-\frac{1}{2}}\beta] \\ &+ v^{-\frac{1}{2}}\frac{e^{i(kr-\eta\ln 2kr)}}{kr}\sum_l e^{2i\sigma_l}\left((l+1)C_l^+ + lC_l^-\right)P_l(\cos\theta)[a_{\frac{1}{2}}\alpha + a_{-\frac{1}{2}}\beta] \\ &+ v^{-\frac{1}{2}}\frac{e^{i(kr-\eta\ln 2kr)}}{kr}\sum_l e^{2i\sigma_l}\Big[P_l^1(\cos\theta)C_l^+(a_{-\frac{1}{2}}e^{-i\phi}\alpha - a_{\frac{1}{2}}e^{i\phi}\beta) \\ &\qquad - P_l^1(\cos\theta)C_l^-(a_{-\frac{1}{2}}e^{-i\phi}\alpha - a_{\frac{1}{2}}e^{i\phi}\beta)\Big]\end{aligned} \tag{B.15}$$

The scattered particle is always measured at $\phi = 0$ in this coordinate system; make this substitution and use the Pauli spinor

$$\chi_{inc} \equiv \begin{pmatrix} a_{\frac{1}{2}} \\ a_{-\frac{1}{2}} \end{pmatrix} = a_{\frac{1}{2}}\alpha + a_{-\frac{1}{2}}\beta$$

(where the spin basis is for the $\pm z$ direction) to describe the polarization of the incident beam. This gives:

$$\begin{aligned}\Psi_{Total} \underset{r\to\infty}{\sim} & v^{-\frac{1}{2}} \left\{ e^{i[kz - \eta \ln k(r-z)]} \left[1 - \frac{\eta^2}{ik(r-z)} \right] \right\} \chi_{inc} \\ & + v^{-\frac{1}{2}} \frac{e^{i(kr - \eta \ln 2kr)}}{r} [f_c(\theta) + \frac{1}{k} \sum_l e^{2i\sigma_l} ((l+1)C_l^+ + lC_l^-) P_l(\cos\theta)] \chi_{inc} \\ & + v^{-\frac{1}{2}} \frac{e^{i(kr - \eta \ln 2kr)}}{kr} \sum_l e^{2i\sigma_l} (C_l^+ - C_l^-) P_l^1(\cos\theta) \begin{pmatrix} 0 & 1 \\ -1 & 0 \end{pmatrix} \chi_{inc}\end{aligned} \tag{B.16}$$

Let $\hat{n} \equiv \frac{\mathbf{k}\times\mathbf{k}'}{|\mathbf{k}\times\mathbf{k}'|} = \hat{y}$, the unit normal to the scattering plane. Then:

$$\begin{pmatrix} 0 & 1 \\ -1 & 0 \end{pmatrix} = i\sigma_y = i\vec{\sigma}\cdot\hat{n}$$

Define

$$A(\theta) \equiv f_c(\theta) + \frac{1}{k} \sum_l e^{2i\sigma_l} [(l+1)C_l^+ + lC_l^-] P_l^1(\cos\theta) \tag{B.17a}$$

$$B(\theta) \equiv \frac{i}{k} \sum_l e^{2i\sigma_l} [C_l^+ - C_l^-] P_l^1(\cos\theta) \tag{B.17b}$$

then the asymptotic form of Ψ_{Total} reduces to the simpler expression:

$$\begin{aligned}\Psi_{Total} \underset{r\to\infty}{\sim} & v^{-\frac{1}{2}} \left\{ e^{i[kz - \eta \ln k(r-z)]} \left[1 - \frac{\eta^2}{ik(r-z)} \right] \right\} \chi_{inc} \\ & + \frac{v^{-\frac{1}{2}} e^{i(kr - \eta \ln 2kr)}}{r} [A(\theta) + B(\theta)\vec{\sigma}\cdot\hat{n}] \chi_{inc}\end{aligned} \tag{B.18}$$

Because of the log terms in the exponents, this is not of the form of a stationary wave function for a potential of finite range, for which we would have:

$$\Psi_{\substack{finite \\ range}} \underset{r\to\infty}{\sim} v^{-\frac{1}{2}} \left\{ e^{ikz}\chi_{inc} + f(\theta)\frac{e^{ikr}}{r}\chi_{inc} \right\} \tag{B.19}$$

but the factor $e^{-i\eta \ln k(r-z)} = e^{-i\eta \ln 2kr \sin^2 \frac{\theta}{2}}$ in (B.18) oscillates rapidly under typical experimental conditions and the angular width of an outgoing wave packet is large enough that this term gives a zero contribution to the cross section at realistic values of θ. Only the second term contributes to the flux measured away from the forward direction for which the factor $e^{-i\eta \ln 2kr}$ is now a phase factor which can be ignored. (See [Ta72], pp 262–266.) For all practical purposes, Ψ_{Total} *is* asymptotically of the form (B.19) with the scattering amplitude given by:

$$f(\theta) = A(\theta) + B(\theta)\vec{\sigma} \cdot \hat{n} \ . \qquad (B.20)$$

$A(\theta)$ and $B(\theta)$ are complex and may be determined only up to a common phase factor so that there are only three independent real functions to be compared with experiment. These are usually taken to be the differential cross section σ, the analyzing power A_y and the spin rotation function Q:

$$\sigma(\theta) = |A(\theta)|^2 + |B(\theta)|^2 \qquad (B.21a)$$

$$A_y(\theta) = \frac{2\mathrm{Re}(A^* B)}{\sigma(\theta)} \qquad (B.21b)$$

$$Q(\theta) = \frac{2\mathrm{Im}(AB^*)}{\sigma(\theta)} \qquad (B.21c)$$

B.2 Discussion of Spin Observables

The scattering amplitude for protons of some initial spin state emerging in some final spin state is obtained by sandwiching the operator $A + B\sigma_y$ in (B.20) between the Pauli spinors for these polarization directions. (The corresponding differential cross section is then the absolute value squared.) In the usual representation of the σ's where σ_z is diagonal, these are:

$$\chi_{+x} = \frac{1}{\sqrt{2}}\begin{pmatrix}1\\1\end{pmatrix} \quad \chi_{-x} = \frac{1}{\sqrt{2}}\begin{pmatrix}1\\-1\end{pmatrix} \qquad \chi_{+y} = \frac{1}{\sqrt{2}}\begin{pmatrix}1\\i\end{pmatrix} \quad \chi_{-y} = \frac{1}{\sqrt{2}}\begin{pmatrix}i\\1\end{pmatrix}$$

$$\chi_{+z} = \begin{pmatrix} 1 \\ 0 \end{pmatrix} \qquad \chi_{-z} = \begin{pmatrix} 0 \\ 1 \end{pmatrix} . \tag{B.22}$$

For example, the cross section for $+\hat{y} \rightarrow +\hat{y}$ scattering (polarization out of the scattering plane) is

$$\frac{d\sigma}{d\Omega}(\theta, +\hat{y} \rightarrow +\hat{y}) = |\chi^{\dagger}_{+y}\{A(\theta) + B(\theta)\sigma_y\}\chi_{+y}|^2 = |A(\theta) + B(\theta)|^2 \tag{B.23}$$

The unpolarized cross section, $\sigma(\theta)$, is a sum on cross sections for the final states and an average on the initial states:

$$\begin{aligned} \sigma(\theta) &= \frac{1}{2}\left(\frac{d\sigma}{d\Omega}(+\hat{y} \rightarrow +\hat{y}) + \frac{d\sigma}{d\Omega}(+\hat{y} \rightarrow -\hat{y}) + \frac{d\sigma}{d\Omega}(-\hat{y} \rightarrow +\hat{y}) + \frac{d\sigma}{d\Omega}(-\hat{y} \rightarrow -\hat{y})\right) \\ &= \tfrac{1}{2}(|A+B|^2 + 0 + 0 + |A-B|^2) \\ &= |A(\theta)|^2 + |B(\theta)|^2 \end{aligned} \tag{B.24}$$

Note the zero terms: the scattering operator of (B.20) can rotate spins about $\hat{y}$ but cannot change $+\hat{y}$ spin to $-\hat{y}$.

To measure the analyzing power, the spins of the outgoing particles are measured although the incident beam may be unpolarized. If the difference between the $+\hat{y}$ and $-\hat{y}$ cross sections is taken with the result divided by the unpolarized cross section, we obtain the analyzing power A_y:

$$\begin{aligned} A_y &= \frac{\frac{d\sigma}{d\Omega}(i \rightarrow +\hat{y}) - \frac{d\sigma}{d\Omega}(i \rightarrow -\hat{y})}{\frac{d\sigma}{d\Omega}(i \rightarrow +\hat{y}) + \frac{d\sigma}{d\Omega}(i \rightarrow -\hat{y})} \\ &= \frac{\frac{1}{2}(|A+B|^2 - |A-B|^2)}{\sigma(\theta)} \\ &= \frac{2\mathrm{Re}(A^*B)}{\sigma(\theta)} \end{aligned} \tag{B.25}$$

Equivalently, A_y can be measured by sending in a beam of protons polarized along $+\hat{y}$ and measuring the *total* cross section at angles θ and $-\theta$ in the scattering plane. From the definition of the vector $\hat{n}$, these measurements use $\hat{n}$'s of opposite directions and hence give rise to the combinations $A + B$ and $A - B$.

The last independent measurement involves the rotation of the spin vector in the scattering plane; for example, protons polarized along $+\hat{x}$ have a finite probably of emerging with spin polarized along $\pm\hat{z}$. Consider an incident beam polarized $+\hat{x}$ and a detector which can distinguish the z–polarization of the scattered protons. The spin rotation parameter Q is defined analogously to A_y as the difference in cross sections for going to the $+\hat{z}$ or $-\hat{z}$ states. Using the spinors in (B.22), it is:

$$\begin{aligned} Q &= \frac{\frac{d\sigma}{d\Omega}(+\hat{x} \to -\hat{z}) - \frac{d\sigma}{d\Omega}(+\hat{x} \to +\hat{z})}{\frac{d\sigma}{d\Omega}(+\hat{x} \to -\hat{z}) + \frac{d\sigma}{d\Omega}(+\hat{x} \to +\hat{z})} \\ &= \frac{\frac{1}{2}|A+iB|^2 - \frac{1}{2}|A-iB|^2}{\frac{1}{2}|A+iB|^2 + \frac{1}{2}|A-iB|^2} \\ &= \frac{-i(AB^* - BA^*)}{|A|^2 + |B|^2} \\ &= \frac{2\mathrm{Im}\, AB^*}{\sigma(\theta)} \end{aligned} \tag{B.26}$$

See Fig. B.2 for a schematic of the necessary spin measurements.

B.3 Numerical Calculation

The computer code used to calculate the observables begins with a Schrödinger-like equation for the upper components of the scattered wavefunction; it is of the form (B.11), or its partial wave expansion (B.12). To get the coefficients $C_l^{\pm}$ in (B.12), which will then give the scattering observables, it is easiest to evaluate $u_l^{\pm}$ at two large values of r. Define:

$$\mathcal{R}_l^{\pm} \equiv \frac{u_l^{\pm}(kR_2)}{u_l^{\pm}(kR_1)} \tag{B.27}$$

where R_1 and R_2 are well outside the range of the nuclear optical potential. Then from (B.12) and (B.27) it follows that:

$$C_l^{\pm} = \frac{F_l(kR_2) - \mathcal{R}_l^{\pm} F_l(kR_1)}{(\mathcal{R}_l^{\pm} G_l(kR_1) - G_l(kR_2)) - i(F_l(kR_2) - \mathcal{R}_l^{\pm} F_l(kR_1))} \tag{B.28}$$

so that the $C_l^{\pm}$'s can be found regardless of the normalization of the radial functions $u_l^{\pm}$.

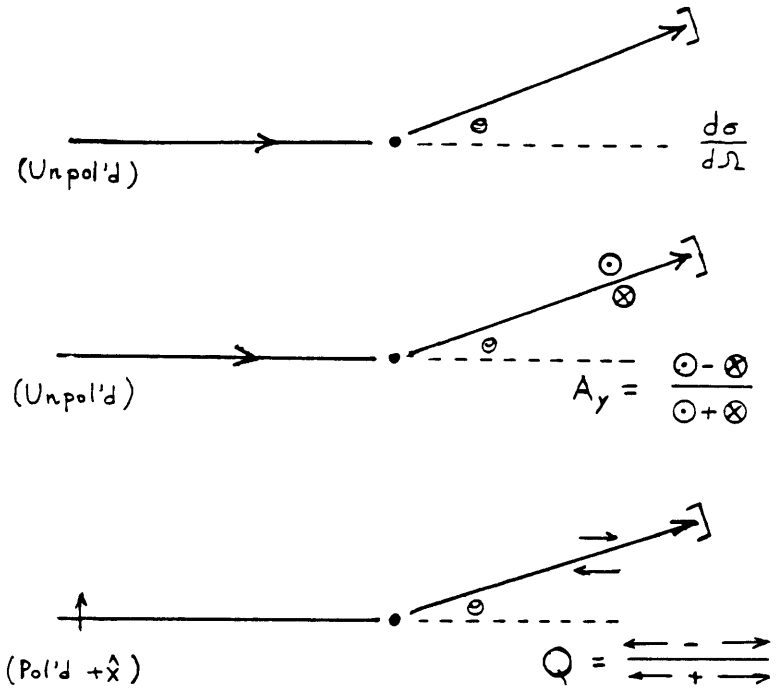

Fig. B.2 Schematic of spin measurements for elastic proton scattering

The $u_l^{\pm}$'s all satisfy the condition $u_l^{\pm}(0) = 0$ and at the first grid point (.04 fm in this work), the value of $u_l^{\pm}$ can be chosen arbitrarily since this amounts to a different choice of normalization. With these two starting points, the Numerov method [Ko86] for integrating a second–order differential equation is used to get the $u_l^{\pm}$ at all other grid points. Since the optical potentials are calculated out to 12 fm, R_1 and R_2 are chosen to be 12 and 12.04 fm.

Having the values of $\mathcal{R}^{\pm}$, we need the values of the Coulomb wavefunctions F_l and G_l evaluated at kR_1 and kR_2 to use in (B.28) to complete the calculation. We also need the values of σ_l to be used in (B.17).

McCarthy [McC68] gives a convenient formula for σ_0:

$$\begin{aligned}\sigma_0 = &-\eta + \frac{\eta}{2}\ln(\eta^2+16) + \frac{7}{2}\tan^{-1}(\frac{\eta}{4}) \\ &- \left[\tan^{-1}\eta + \tan^{-1}(\frac{\eta}{2}) + \tan^{-1}(\frac{\eta}{3})\right] \\ &- \frac{\eta}{12(\eta^2+16)}\left[1 + \frac{1}{30}\frac{\eta^2-48}{(\eta^2+16)^2} + \frac{1}{105}\frac{\eta^4-160\eta^2+1680}{(\eta^2+16)^4}\right]\end{aligned} \tag{B.29}$$

From this, the rest of the σ_l's follow from the recursion formula:

$$\sigma_i = \sigma_{i-1} + \tan^{-1}(\frac{\eta}{i}) \tag{B.30}$$

To evaluate F_l and G_l, I have used the asymptotic expansion in [Ab72] (Section 14.5), where for large ρ (which is typically $\rho \approx 39$ in this work) we have:

$$\begin{aligned}F_l &= g_l \cos\theta_l + f_l \sin\theta_l \\ G_l &= f_l \cos\theta_l - g_l \sin\theta_l\end{aligned} \tag{B.31}$$

where

$$\theta_l = \rho - \eta\ln 2\rho - l\frac{\pi}{2} + \sigma_l \tag{B.32}$$

and an asymptotic expansion is given for f and g:

$$f_l + ig_l \sim 1 + \frac{(i\eta - l)(i\eta + l + 1)}{1!(2i\rho)} + \frac{(i\eta - l)(i\eta - l + 1)(i\eta + l + 1)(i\eta + l + 2)}{2!(2i\rho)^2} + \cdots \tag{B.33}$$

20 terms of this series were sufficient to agree with tabulated values.

It is only necessary to use these formulae for $l = 0$ and $l = 1$ since then we can use a recurrence relation to get the rest of the F_l's and G_l's:

$$l[(l+1)^2+\eta^2]u_{l+1} = (2l+1)\left[\eta + \frac{l(l+1)}{\rho}\right]u_l - (l+1)[l^2+\eta^2]^{\frac{1}{2}}u_{l-1} \tag{B.34}$$

where u can be F or G. McCarthy advises against using this procedure to recur upward on the F_l's since for some values of the argument ρ this can be numerically unstable; the alternative is similar to the remedy used for the same problem with spherical Bessel

functions [Ko86], using downward recurrence for the F_l's, then fixing the normalization of the set with the Wronskian relation:

$$F_0 G_1 - F_1 G_0 = \frac{1}{\eta} \qquad (B.35)$$

However, for the values of ρ in this work, upward recurrence on the F's was well–behaved and in fact more accurate than downward recurrence.

Having calculated the full set of $C_l^{\pm}$, the scattering observables are found from (B.17) and (B.24–26). 60 partial waves are sufficient for the scattering calculations for $T_{\rm lab} = 200$ MeV.

Appendix C. "Schrödinger Equivalent" Equation and Potentials

C.1 Reduction to (Local) Second–Order Equation

We begin with the Dirac equation for a particle with an anomalous magnetic moment moving in central scalar, vector and tensor *nuclear* potentials; also in a Coulomb potential which is a central *vector* potential:

$$\Big\{\vec{\alpha}\cdot\mathbf{p}+\beta[M+V^S_{Nuc}(r)]+[V^0_{Nuc}(r)+V_C(r)] - i\beta\vec{\alpha}\cdot\hat{r}\big[U^T_{Nuc}(r)-\frac{\kappa}{2M}\frac{\partial}{\partial r}V_C(r)\big]\Big\}\psi = E\psi \tag{C.1}$$

Define:

$$\begin{aligned} U_S(r) &\equiv V^S_{Nuc}(r) \\ U_0(r) &\equiv V^S_{Nuc}(r)+V_C(r) \\ U_T(r) &\equiv V^T_{Nuc}(r)-\frac{\kappa}{2M}\frac{\partial}{\partial r}V_C(r) \end{aligned} \tag{C.2}$$

use the definitions:

$$\vec{\alpha}=\begin{pmatrix}0 & \vec{\sigma}\\ \vec{\sigma} & 0\end{pmatrix} \qquad \beta=\begin{pmatrix}1 & 0\\ 0 & -1\end{pmatrix} \tag{C.3}$$

and distinguish the upper and lower components of ψ:

$$\psi=\begin{pmatrix}\psi_u\\ \psi_l\end{pmatrix} \tag{C.4}$$

where ψ_u and ψ_l are two-component Pauli-type functions.

This gives a pair of coupled equations for the upper and lower wavefunctions:

$$(\vec{\sigma}\cdot\mathbf{p})\psi_l+(M+U_S+U_0)\psi_u-iU_T(\vec{\sigma}\cdot\hat{r})\psi_l=E\psi_u \tag{C.5a}$$

$$(\vec{\sigma}\cdot\mathbf{p})\psi_u+(-M-U_S+U_0)\psi_l+iU_T(\vec{\sigma}\cdot\hat{r})\psi_u=E\psi_l \tag{C.5b}$$

Combining these to get a single equation for ψ_u, we find:

$$[(\vec{\sigma}\cdot\mathbf{p})-iU_T(\vec{\sigma}\cdot\hat{r})]\frac{1}{(\mathcal{E}-\mathcal{M})}[(\vec{\sigma}\cdot\mathbf{p}+iU_T(\vec{\sigma}\cdot\hat{r})]\psi_u=(\mathcal{E}-\mathcal{M})\psi_u \tag{C.6}$$

where $\mathcal{E} = E - U_0$ and $\mathcal{M} = M + U_S$, which are both functions of r. It is also convenient to use $B \equiv \mathcal{E} + \mathcal{M}$. After some algebra, we get:

$$\left[-\frac{\nabla^2}{2E}+\frac{1}{2E}\left(2MU_S + 2EU_0 + U_S^2 - U_0^2 + U_T^2 - \frac{B'}{B}U_T + \frac{2}{r}U_T + U_T'\right)\right.$$
$$\left. + \frac{i}{2Er}\frac{B'}{B}\mathbf{r}\cdot\mathbf{p} + \left(-\frac{1}{2Er}\frac{B'}{B} + \frac{U_T}{Er}\right)\vec{\sigma}\cdot\mathbf{L}\right]\psi_u = \frac{(E^2 - M^2)}{2E}\psi_u \qquad (C.7)$$

In deriving (C.7), the operator relations

$$(\vec{\sigma}\cdot\mathbf{A}_{op})(\vec{\sigma}\cdot\mathbf{B}_{op}) = \mathbf{A}_{op}\cdot\mathbf{B}_{op} + i\vec{\sigma}\cdot(\mathbf{A}_{op}\times\mathbf{B}_{op}) \qquad (C.8)$$

and

$$\mathbf{p}_{op} = \frac{1}{i}\nabla \qquad\qquad \mathbf{L}_{op} = \mathbf{r}\times\mathbf{p}_{op}$$

were used.

When (C.7) is *viewed* as a Schrödinger equation for ψ_u, there is now a term for the kinetic energy, a central potential term which is a complicated function of U_S, U_0 and U_T, a spin-orbit potential and a non-local "Darwin" potential, $\frac{i}{2Mr}\frac{B'}{B}\mathbf{r}\cdot\mathbf{p}$. It is possible to get an equation with all *local* potential terms with the substitution:

$$\psi_u(\mathbf{r}) = [A(r)]^{\frac{1}{2}}\phi(\mathbf{r})\ . \qquad (C.9)$$

where

$$A(r) = \frac{\mathcal{E}(r) + \mathcal{M}(r)}{E + M} = \frac{B(r)}{E + M} \qquad (C.10)$$

After this substitution and some more algebra, it is found that the non-local term is canceled by a contribution from the kinetic term. Some additional central terms arise, which are grouped as "U_{Darwin}" and which are typically small compared to the other

potentials. The result is a Schrödinger-like equation for ϕ (after multiplying through again by $2E$):

$$\Big[-\nabla^2 + 2MU_S + 2EU_0 + U_S^2 - U_0^2 + U_T^2 + \left(\frac{2}{r} - \frac{B'}{B}\right) U_T + U_T' + U_{\text{Darwin}} + \left(-\frac{1}{r}\frac{B'}{B} + \frac{2U_T}{r}\right) \vec{\sigma}\cdot\mathbf{L}\Big]\phi(\mathbf{r}) = (E^2 - M^2)\phi(\mathbf{r}) \tag{C.11}$$

where

$$U_{\text{Darwin}} = \frac{3}{4}\left(\frac{B'}{B}\right)^2 - \frac{B'}{rB} - \frac{1}{2}\frac{B''}{B} \tag{C.12}$$

While $\phi(\mathbf{r})$ is *not* the upper component wavefunction, note that since $A(r) \to 1$ as $r \to \infty$, it does tend to $\psi(\mathbf{r})$ at large r. So we can use the differential equation (C.11) to find $\phi(\mathbf{r})$ and thus $\psi(\mathbf{r})$ at large r to match asymptotic functions. This is what is done in the scxattering codes used in this work.

C.2 Equivalent Potentials

It is of interest to see how the potentials U_S, U_0, and U_T relate to those used in a Schrödinger equation for the scattered proton. Such a correspondence can only be approximate, since even after identifying ψ_u with the Pauli wavefunction that would occur in nonrelativistic quantum mechanics, there is still the nonlocal Darwin term and the relativistic kinematics embodied in (C.11).

What is customarily done is to ignore the Darwin term and look at the central and spin-orbit parts of (C.7). (Note that (C.7) is written as "$\frac{\nabla^2}{2E} + \cdots$", instead of with M in the denominator.) Thus,

$$U_{\text{eff}} \equiv \frac{1}{2E}\left(2MU_S + 2EU_0 + U_S^2 - U_0^2 + U_T^2 - \frac{B'}{B}U_T - \frac{2}{r}U_T + U_T'\right) \tag{C.13}$$

and

$$U_{\text{so}} \equiv \frac{1}{2E}\left(-\frac{1}{r}\frac{B'}{B} + \frac{2U_T}{r}\right) \tag{C.14}$$

are compared with the central and spin-orbit terms of Schrödinger dynamics. Also, with these definitions, the equation for ψ_u is

$$\left[-\frac{\nabla^2}{2E} + U_{\text{eff}} + U_{\text{so}}\vec{\sigma}\cdot\mathbf{L} + U_{\text{Darwin}}\right]\psi_u = \frac{(E^2 - M^2)}{2E}\psi_u \qquad (C.15)$$

C.3 Relativistic Kinematics

Eq. (C.1) is a single particle equation which is used to describe the nucleon–nucleus center of mass frame motion of the proton. A prescription for dealing center of mass motion is needed in order to define M and E in (C.1). We choose M to be the rest mass of the proton and E to be the (total) energy of the projectile in the proton–nucleus center–of–mass frame:

$$E \equiv E_{p,cm} = \frac{M^2 + M_T(M + T_{\text{lab}})}{\sqrt{(M + M_T)^2 + 2M_T T_{\text{lab}}}} \qquad (C.16)$$

where M_T is the mass of the target. When other (similar) choices are made, there is a small but noticeable change in the observables, especially for scattering from ^{12}C and ^{16}O. A systematic treatment of "recoil", or $\frac{1}{A}$ corrections remains to be done for relativistic systems.

The scattering code (Appendix B) uses the following approximations for the Coulomb interaction: The charge density of the target is taken to be that of a uniformly charged sphere of radius $r_0 A^{\frac{1}{3}}$ with $r_0 = 1.25\ fm$. Nonrelativistic Coulomb wavefunctions are used for the matching condition at large r. The observables are not sensitive to these choices. However, in comparing data with the predictions of different theoretical models, the details of the scattering calculation must not be completely overlooked, especially when different models for the optical potential give similar predictions for the observables.

Appendix D. Expressions for Spin Observables for Quasi-Elastic Proton Scattering

The terms in $M_{i'j}$ (Eq. (3.B.34)) which are proportional to $s_i \cdot s_f$ are listed first. Define:

$$\begin{aligned}
S \equiv & -s_i \cdot s_f \Big[t_S^* t_S (1 + K_1 \cdot P_2)(1 + K_2 \cdot P_2) - t_P^* t_P (1 - K_1 \cdot P_1)(1 - K_2 \cdot P_2) \\
& + 2(t_V^* t_V - t_A^* t_A)(1 + K_1 \cdot K_2 P_1 \cdot P_2 - K_1 \cdot P_1 K_2 \cdot P_2 + K_1 \cdot P_2 K_2 \cdot P_1) \\
& - 8 t_T^* t_T (K_1 \cdot P_1 + K_2 \cdot P_2) \\
& + 2\mathrm{Re}\,(t_V^* t_S + 2 t_T^* t_A)(K_1 \cdot K_2 + K_1 \cdot P_2 + K_2 \cdot P_1 + P_1 \cdot P_2) \\
& + 4\mathrm{Re}\,(t_T^* t_P - t_T^* t_S)(K_1 \cdot K_2 P_1 \cdot P_2 - K_1 \cdot P_2 K_2 \cdot P_1) \\
& + 2\mathrm{Re}\,(t_A^* t_P + 2 t_T^* t_V)(K_1 \cdot P_2 + K_2 \cdot P_1 - K_1 \cdot K_2 - P_1 \cdot P_2) \Big]
\end{aligned} \tag{D.1}$$

Then the general spin observable is given by:

$$\begin{aligned}
4M_{i'j} = & \; S + t_S^* t_S (1 + K_2 \cdot P_2) s_i \cdot K_1 s_f \cdot P_1 \\
& + t_P^* t_P (1 - K_2 \cdot P_2) s_i \cdot K_1 s_f \cdot P_1 \\
& + 2 t_V^* t_V \big\{ s_i \cdot K_1 s_f \cdot K_2 P_1 \cdot P_2 + s_f \cdot P_1 s_i \cdot K_2 K_1 \cdot P_2 - s_f \cdot P_1 s_i \cdot K_1 K_2 \cdot P_2 \\
& \quad + (1 - K_1 \cdot P_1)(s_f \cdot K_2 s_i \cdot P_2 + s_i \cdot K_2 s_f \cdot P_2) \\
& \quad + s_f \cdot P_2 s_i \cdot K_1 K_2 \cdot P_1 + s_i \cdot P_2 s_f \cdot P_1 K_1 \cdot K_2 \big\} \\
& + 2 t_A^* t_A \big\{ s_i \cdot K_1 s_f \cdot P_1 K_2 \cdot P_2 - s_i \cdot K_1 s_f \cdot K_2 P_1 \cdot P_2 - s_i \cdot K_1 s_f \cdot P_2 K_2 \cdot P_1 \\
& \quad + (1 + K_1 \cdot P_1)(s_i \cdot K_2 s_f \cdot P_2 + s_f \cdot K_2 s_i \cdot P_2) \\
& \quad - s_f \cdot P_1 s_i \cdot P_2 K_1 \cdot K_2 - s_i \cdot K_2 s_f \cdot P_1 K_1 \cdot P_2 \big\} \\
& - 8 t_T^* t_T \big\{ s_i \cdot K_1 s_f \cdot P_1 + 2(s_i \cdot K_2 s_f \cdot P_2 + s_i \cdot P_2 s_f \cdot K_2) \big\} \\
& + 2\mathrm{Re}(t_V^* t_S + 2 t_T^* t_A)(s_i \cdot K_1 s_f \cdot K_2 + s_f \cdot P_1 s_i \cdot K_2 \\
& \quad + s_f \cdot P_2 s_i \cdot K_1 + s_i \cdot P_2 s_f \cdot P_1) \\
& + 2\mathrm{Re}(t_A^* t_P + 2 t_T^* t_V)(s_i \cdot K_1 s_f \cdot P_2 + s_f \cdot P_1 s_i \cdot K_2 \\
& \quad - s_f \cdot K_2 s_i \cdot K_1 - s_i \cdot P_2 s_f \cdot P_1) \\
& + 4\mathrm{Re}(t_A^* t_V)(s_i \cdot P_2 s_f \cdot K_2 - s_i \cdot K_2 s_f \cdot P_2) \\
& + 4\mathrm{Re}(t_T^* t_S)\big\{ (1 + K_1 \cdot P_1)(s_f \cdot K_2 s_i \cdot P_2 - s_i \cdot K_2 s_f \cdot P_2) \\
& \quad - K_1 \cdot K_2 s_f \cdot P_1 s_i \cdot P_2 + K_1 \cdot P_2 s_i \cdot K_2 s_f \cdot P_1 + K_2 \cdot P_1 s_i \cdot K_1 s_f \cdot P_2 \\
& \quad - P_1 \cdot P_2 s_i \cdot K_1 s_f \cdot K_2 \big\} \\
& + 4\mathrm{Re}(t_T^* t_P)\big\{ (1 - K_1 \cdot P_1)(s_f \cdot K_2 s_i \cdot P_2 - s_f \cdot P_2 s_i \cdot K_2) \\
& \quad + K_1 \cdot K_2 s_f \cdot P_1 s_i \cdot P_2 - K_1 \cdot P_2 s_i \cdot K_2 s_f \cdot P_1 - K_2 \cdot P_1 s_i \cdot K_1 s_f \cdot P_2 \\
& \quad + P_1 \cdot P_2 s_i \cdot K_1 s_f \cdot K_2 \big\}
\end{aligned} \tag{D.2}$$

Appendix E. Relativistic Expression for Magnetic Moment

In this section I derive the magnetic formula as used with *relativistic* wavefunctions. This is essentially the derivation of Margenau [Ma40] recast in the notation of [Se86].

Consider a Dirac particle of charge q bound in a central field $U(r)$ (from nuclear potentials), in a $(j, m = j)$ state. Introduce a small external magnetic field $\mathbf{B} = H_z\hat{z}$. This will give a change in energy of the particle, ΔE, which can be evaluated to first order in peturbation theory. We then get the magnetic moment M_z from $M_z = -\frac{\partial \Delta E}{\partial H_z}$.

The external $\mathbf{A}$ field for this choice can be written as $\mathbf{A} = \frac{H_z}{2}(-y, x, 0)$ and we can make the gauge choice $A_0 = 0$. The Dirac wavefunction for the particle, $\psi_{n\kappa m}$ satisfies:

$$\left(\gamma_\mu(p^\mu - qA^\mu) - \frac{\lambda e}{4M}F^{\mu\nu}\sigma_{\mu\nu} + U(r) - M\right)\psi_{n\kappa m} = 0 \qquad (E.1)$$

where

$$\lambda_p = 1.7928 \qquad \text{and} \qquad \lambda_n = -1.931 \qquad (E.2)$$

are the appropriate values for protons and neutrons, and e is the charge of the proton. We can also write this as:

$$(\vec{\alpha}\cdot\mathbf{p} - q\vec{\alpha}\cdot\mathbf{A} + \frac{\lambda e}{4M}\beta\sigma_{\mu\nu}F^{\mu\nu} + U(r) + \beta M)\psi_{n\kappa m} = E\psi_{n\kappa m} \qquad (E.3)$$

so that the contribution to the Dirac Hamiltonian of the "Dirac" magnetic term is:

$$\begin{aligned} H'_D = -q\vec{\alpha}\cdot\mathbf{A} &= \frac{qH_z}{2}(y\alpha_x - x\alpha_y) \\ &= \frac{qH_z}{2}\begin{pmatrix} 0 & & & y+ix \\ & & y-ix & \\ & y+ix & & \\ y-ix & & & 0 \end{pmatrix} \\ &= \frac{iqrH_z}{2}\sqrt{\frac{8\pi}{3}}\begin{pmatrix} 0 & & & Y_{1,-1} \\ & & Y_{1,1} & \\ & Y_{1,-1} & & \\ Y_{1,1} & & & 0 \end{pmatrix} \end{aligned} \qquad (E.4)$$

and that of the anomalous term is:

$$H'_A = \frac{\lambda e}{4M}\beta\sigma_{\mu\nu}F^{\mu\nu} = -\frac{\lambda e}{2M}\beta\mathbf{B}\cdot\Sigma_z$$
$$= -\frac{\lambda e}{2M}H_z\begin{pmatrix}1 & & & 0\\ & -1 & & \\ & & -1 & \\ 0 & & & 1\end{pmatrix} \qquad (E.5)$$

With wavefunctions defined as in [Se86],

$$\psi_{n\kappa m}(\mathbf{r}) = \begin{pmatrix} i\frac{G_{n\kappa}(r)}{r}\Phi_{\kappa m} \\ -\frac{F_{n\kappa}(r)}{r}\Phi_{-\kappa m}\end{pmatrix} \quad \text{with} \quad \Phi_{\kappa m} = \sum_{m_l,m_s}\langle l\, m_l\, \tfrac{1}{2}\, m_s | l\, \tfrac{1}{2}\, j\, m\rangle Y_{l,m_l}\chi_{m_s} \qquad (E.6)$$

there are two cases of interest, the "parallel" case, where $l \equiv l_{upper} = j - \frac{1}{2}$ and the "antiparallel" case, where $l \equiv l_{upper} = j + \frac{1}{2}$. For these cases we have:

$$\text{Parallel:} \qquad \psi_{n\kappa m=j}(\mathbf{r}) = \begin{pmatrix} i\frac{G_{n\kappa}(r)}{r}\begin{bmatrix}Y_{l,l}\\ 0\end{bmatrix} \\ -\frac{F_{n\kappa}(r)}{r}\begin{bmatrix}-\sqrt{\frac{1}{2j+2}}Y_{l+1,l}\\ \sqrt{\frac{2j+1}{2j+2}}Y_{l+1,l+1}\end{bmatrix}\end{pmatrix} \qquad (E.7)$$

$$\text{Anti}-\text{parallel:} \qquad \psi_{n\kappa m=j}(\mathbf{r}) = \begin{pmatrix} i\frac{G_{n\kappa}(r)}{r}\begin{bmatrix}-\sqrt{\frac{1}{2j+2}}Y_{l,l-1}\\ \sqrt{\frac{2j+1}{2j+2}}Y_{l,l}\end{bmatrix} \\ -\frac{F_{n\kappa}(r)}{r}\begin{bmatrix}Y_{l-1,l-1}\\ 0\end{bmatrix}\end{pmatrix} \qquad (E.8)$$

(From here on, assume $m = j$ in the matrix elements and drop this index on ψ.)

Evaluate the matrix element of H'_D (Dirac moment piece). The parallel case gives:

$$\langle\psi_{n\kappa}|H'_D|\psi_{n\kappa}\rangle\Big|_{\text{par}} = \int d^3r\,\psi^\dagger_{n\kappa}(\mathbf{r})H'_D(\mathbf{r})\psi_{n\kappa}(\mathbf{r})$$
$$= \frac{-qH_z}{2}\sqrt{\frac{8\pi}{3}}\int rF_{n\kappa}(r)G_{n\kappa}(r)dr \qquad (E.9)$$
$$\cdot\sqrt{\frac{2j+1}{2j+2}}\left[\int Y^*_{l,l}Y_{1,-1}Y_{l+1,l+1}d\Omega - \int Y^*_{l+1,l+1}Y_{1,1}Y_{l,l}\,d\Omega\right]$$

Use

$$\int Y^*_{l_3,m_3}\, Y_{l_1,m_1}\, Y_{l_2,m_2}\, d\Omega = \left[\frac{(2l_1+1)(2l_2+1)}{4\pi(2l_3+1)}\right]^{\frac{1}{2}} \langle l_1\, m_1\, l_2\, m_2\, |l_3\, m_3\rangle \cdot \langle l_1\, 0\, l_2\, 0\, |l_3\, 0\rangle \tag{E.10}$$

to evaluate the integrals of the spherical harmonics and get:

$$\langle \psi_{n\kappa}|H'_D|\psi_{n\kappa}\rangle\Big|_{\rm par} = qH_z\left(\frac{2j+1}{2j+2}\right)\int_0^\infty rF_{n\kappa}(r)G_{n\kappa}(r)\,dr \tag{E.11}$$

The anti-parallel case gives:

$$\begin{aligned}\langle \psi_{n\kappa}|H'_D|\psi_{n\kappa}\rangle\Big|_{\rm par} &= \frac{-qH_z}{2}\sqrt{\frac{8\pi}{3}}\left[\int_0^\infty rF_{n\kappa}(r)G_{n\kappa}(r)\,dr\right]\sqrt{\frac{2j+1}{2j+2}} \\ &\quad\cdot\left[\int Y^*_{l,l}Y_{1,1}Y_{l-1,l-1}\,d\Omega - \int Y^*_{l-1,l-1}Y_{1,-1}Y_{l,l}\,d\Omega\right] \\ &= -qH_z\left(\frac{2j+1}{2j+2}\right)\int_0^\infty rF_{n\kappa}(r)G_{n\kappa}(r)\,dr\end{aligned} \tag{E.12}$$

Now evaluate the matrix element of H'_A. The parallel case gives:

$$\langle \psi_{n\kappa}|H'_A|\psi_{n\kappa}\rangle\Big|_{\rm par} = -\frac{\lambda e}{2M}H_z\left\{\int_0^\infty |G_{n\kappa}(r)|^2\,dr + \left(\frac{j}{j+1}\right)\int_0^\infty |F_{n\kappa}(r)|^2\,dr\right\} \tag{E.13}$$

while the antiparallel case gives:

$$\langle \psi_{n\kappa m}|H'_A|\psi_{n\kappa m}\rangle\Big|_{\rm a-par} = -\frac{\lambda e}{2M}H_z\left\{-\left(\frac{j}{j+1}\right)\int_0^\infty |G_{n\kappa}(r)|^2\,dr - \int_0^\infty |F_{n\kappa}(r)|^2\,dr\right\} \tag{E.14}$$

The total first-order ΔE due to $H' = H'_D + H'_A$ is:

$$\begin{aligned}\Delta E\Big|_{par} &= \langle \psi_{n\kappa m}|H'|\psi_{n\kappa m}\rangle\Big|_{par} \\ &= qH_z\left(\frac{2j+1}{2j+2}\right)\int_0^\infty F_{n\kappa}(r)G_{n\kappa}(r)\,dr \\ &\quad - \frac{\lambda e}{2M}H_z\left\{\int_0^\infty |G_{n\kappa}(r)|^2\,dr + \left(\frac{j}{j+1}\right)\int_0^\infty |F_{n\kappa}(r)|^2\,dr\right\}\end{aligned} \tag{E.15}$$

$$\Delta E\Big|_{a-par} = \langle \psi_{n\kappa m}|H'|\psi_{n\kappa m}\rangle\Big|_{a-par}$$
$$= -qH_z\left(\frac{2j+1}{2j+2}\right)\int_0^\infty F_{n\kappa}(r)G_{n\kappa}(r)\,dr$$
$$-\frac{\lambda e}{2M}H_z\left\{-\left(\frac{j}{j+1}\right)\int_0^\infty |G_{n\kappa}(r)|^2\,dr + \int_0^\infty |F_{n\kappa}(r)|^2\,dr\right\} \qquad (E.16)$$

which we now use to take $M_z = -\frac{\partial(\Delta E)}{\partial H_z}$. (Omit a factor of $-H_z$.) Use $q = \left(\frac{1+\tau_3}{2}\right)e$ and $\mu_0 = \frac{\hbar e}{2M_p c}$ The two cases can be combined to give:

$$\mu_z = \frac{M_z}{\mu_0}$$
$$= \omega\left(\frac{1+\tau_3}{2}\right)\left(\frac{2j+1}{2j+2}\right)\frac{M_p c}{\hbar}\int_0^\infty rF_{n\kappa}(r)G_{n\kappa}(r)\,dr$$
$$-\omega\lambda\left(\frac{j}{j+1}\right)^{\frac{1}{2}}\left[\left(\frac{j}{j+1}\right)^{\frac{\omega}{2}}\int_0^\infty |G_{n\kappa}(r)|^2\,dr + \left(\frac{j}{j+1}\right)^{-\frac{\omega}{2}}\int |F_{n\kappa}(r)|^2\,dr\right]$$
$$\text{where} \qquad \omega = \begin{cases} -1, & \text{Parallel} \\ +1, & \text{Anti-parallel} \end{cases} \qquad (E.17)$$

and the radial functions G and F are those used in [Se86].